

Hydrogen-Enriched Combustion Study at High Turbulence and Swirl Levels Inside a Gas Turbine Combustor

by

Mohamed ELBAYOUMI

THESIS PRESENTED TO ÉCOLE DE TECHNOLOGIE SUPÉRIEURE
IN PARTIAL FULFILLMENT FOR THE DEGREE OF
DOCTOR OF PHILOSOPHY
Ph. D.

MONTREAL, APRIL 13, 2022

ÉCOLE DE TECHNOLOGIE SUPÉRIEURE
UNIVERSITÉ DU QUÉBEC



Mohamed Elbayoumi, 2022



This [Creative Commons](#) licence allows readers to download this work and share it with others as long as the author is credited. The content of this work can't be modified in any way or used commercially.

BOARD OF EXAMINERS

**THIS THESIS HAS BEEN EVALUATED
BY THE FOLLOWING BOARD OF EXAMINERS**

Mr. Patrice Seers, Research Supervisor
Department of Mechanical Engineering, École de technologie supérieure

Mr. François Garnier, Research Co-supervisor
Department of Mechanical Engineering, École de technologie supérieure

Mr. Hany Moustapha, Research Co-supervisor
Department of Mechanical Engineering, École de technologie supérieure

Mrs. Ouassima Akhrif, President of the Board of Examiners
Department of Electrical Engineering, École de technologie supérieure

Mr. François Morency, Member of the jury
Department of Mechanical Engineering, École de technologie supérieure

Mr. Gilles Bourque, External Member of the jury
Siemens Energy Canada

**THIS THESIS WAS PRESENTED AND DEFENDED
IN THE PRESENCE OF A BOARD OF EXAMINERS AND THE PUBLIC**

AT ÉCOLE DE TECHNOLOGIE SUPÉRIEURE

ACKNOWLEDGMENTS

I would like to address my thanks to my thesis supervisor Prof. Patrice Seers for his coaching and fruitful discussions. Also, I would like to express my gratitude to my co-supervisor Prof. François Garnier for his support and productive conversations. Special thanks also for my co-supervisor Prof. Hany Moustapha, for his everlasting directions. Great thanks too to the jury members, Prof. Ouassima Akhrif, Prof. François Morency, and Prof. Gilles Bourque for revising and assessing this manuscript.

I would like to acknowledge the financial support from the Military Technical College (MTC) for this dissertation. Great thanks also to Compute Canada for allowing me to perform CFD computations on its different supercomputer platforms, such as Cedar and Graham.

Sincere thanks to the TFT team, including professors and students, for the rich discussions we shared together. Also, special thanks for the IT support provided to this research by the IT specialist.

My last but not least thanks go to my father's spirit, my mom, my beloved wife, my sisters and my kids for their endless love and unfailing support. I want to simply tell you: I love you all, you are my strength, and you all inspired me to achieve this success, which in turn is dedicated to you. These few words are meant to express the love and joy of life, which you inspired in me.

Hydrogen-enriched combustion study at high turbulence and swirl levels inside a gas turbine combustor

Mohamed ELBAYOUMI

ABSTRACT

Given the limited reserves of fossil fuels and the environmental ramifications of their burning; a transfer to new energy resources is all but inevitable. Hydrogen-blended fuel is a promising resource for future generations of Gas Turbine Engines (GTE), due to its high reactivity and ability to reduce carbon emissions. However, several limitations prevent its application, especially for swirl-configurations. The literature does not account for the hydrogen-swirl-equivalence ratio interaction at high turbulence levels, a shortcoming this dissertation addresses. The main objective of this research is to numerically investigate the effects of hydrogen addition (to methane) and swirl intensity on the combustion process under relevant GTE conditions. A numerical study is conducted to assess Hydrogen-Enriched Combustion (HEC) in a lab-scale burner operating at a high turbulence level ($Re_{in} = 36,000$ and u'/S_L up to 45), under lean and stoichiometric burning conditions. A wide range of H_2 (up to 90%) is used for enriching CH_4 -air lean combustion, in combination with a high swirl level (S up to 1.3). The study reveals the feasibility of using H_2 - CH_4 blends with 25% H_2 to replace CH_4 in the primary stages of GTE operation, and of using up to 90% and 60% H_2 to enrich lean and stoichiometric combustion, respectively, without any design modification. Under the studied conditions, it is found that H_2 addition raises the reaction zone temperature, reduces the size of the Inner Recirculation Zone (IRZ), responsible for stabilizing the flame, and results in longer flames, due to the interaction between the high reactivity of H_2 with a high turbulence level. Conversely, the swirl intensity is found to reduce the flame surface area and associated heat release, increase the IRZ size, in addition to resulting in shorter flames, due to an increased turbulent intensity. Hence, increasing the swirl intensity is favoured when using H_2 -blended fuel with high H_2 concentrations. Radiation is considered for all simulations and found influential, as it yields a reduction of the outlet temperature by not less than 100 K, thus reducing emissions by half. A moderate H_2 concentration (up to 50%) and swirl intensity up to 1.3 are found to slightly increase NO_x ; however, such an increase is not deemed significant, for as long as NO_x levels are generally in the order of a few ppm at the burner's outlet. H_2 results in reducing CO, as it promotes CO conversion into CO_2 , which was also reduced as the H_2 concentration increased. Overall, hydrogen-blended fuel is highlighted as an encouraging resource towards a carbon-free fuel and HEC is deemed as a clean combustion approach.

Keywords : gas turbine engine, hydrogen-enriched combustion, swirl-configuration, computational fluid dynamics, inner recirculation zone

Étude de combustion enrichie en hydrogène à des niveaux élevés de turbulence et de tourbillon à l'intérieur d'une chambre de combustion de turbine à gaz

Mohamed ELBAYOUMI

RÉSUMÉ

La combustion d'énergie fossile et ses ramifications environnementales résultant de sa combustion font que la migration vers de nouvelles ressources énergétiques devient inévitable. Les carburants à base d'hydrocarbures conventionnels mélangés à de l'hydrogène sont une solution prometteuse vers une transition énergétique des unités de génération de puissance comme les turbines à gaz, car l'ajout d'hydrogène réduit les émissions carbonées. Cependant, l'ajout d'hydrogène apporte de nouvelles contraintes au niveau de la combustion, par sa vitesse de propagation plus rapide et sa grande plage d'inflammabilité. Ainsi l'interaction entre la richesse du mélange et l'écoulement structuré de la chambre de combustion nécessite une étude plus approfondie lorsque des niveaux de turbulence élevés sont présents afin de quantifier l'impact sur la flamme obtenue. L'objectif principal de cette thèse est d'étudier numériquement l'effet de l'ajout d'hydrogène au méthane et de l'intensité de l'écoulement structuré de type swirl sur le processus de combustion dans des conditions approchant les turbines à gaz. Ainsi l'étude numérique propose d'évaluer la combustion enrichie en hydrogène d'un brûleur de laboratoire fonctionnant à un niveau de turbulence élevé ($Re_{in} = 36,000$ et $/S_L$ up to 45) et ce, dans des conditions de mélange pauvre et stœchiométrique. Une large plage d'ajout d'hydrogène (jusqu'à 90%) est utilisée pour enrichir la combustion de mélange pauvre à base de méthane, et ce, pour différents niveaux d'intensité de swirl. L'étude montre la faisabilité d'utiliser des mélanges contenant jusqu'à 25% de H_2 sans modifications majeures à la flamme obtenue. Il apparaît également possible d'utiliser jusqu'à 90% H_2 en mélange pauvre et 60% de H_2 pour un mélange stœchiométrique, avec toutefois une légère différence sur la flamme obtenue. Dans les conditions étudiées, l'ajout de H_2 augmente la température de la zone de réaction, réduit la taille de la zone de recirculation interne qui est responsable de la stabilisation de la flamme. Ainsi dans la configuration initiale, l'ajout d'hydrogène en forte concentration entraîne des flammes plus longues, en raison de l'interaction entre la réactivité élevée de H_2 et la turbulence. Toutefois en augmentant l'intensité du swirl, la surface de la flamme est réduite et augmente légèrement la taille de la zone de recirculation interne, ce qui entraîne des flammes plus courtes, en raison de l'intensité turbulente accrue. Par conséquent, il est suggéré d'augmenter l'intensité de l'écoulement structuré de type swirl lors de l'utilisation de carburant à forte teneur de H_2 . L'étude numérique a également permis d'illustrer l'importance des pertes par rayonnement, car il entraîne une réduction de la température de sortie d'au moins 100 K, ce qui se traduit par des émissions de NO réduites de moitié. Toutefois, les résultats démontrent un comportement non linéaire entre la concentration de H_2 et la température de flamme et les NO obtenus. Ainsi jusqu'à une concentration modérée de H_2 (50%) et un swirl intense, les NO augmentent légèrement, mais restent à des niveaux de l'ordre de quelques ppm à la sortie du brûleur. En contrepartie, de fortes concentrations de H_2 entraînent de plus fortes augmentations de température et donc de NO lorsque

l'intensité du swirl est intense. Dans l'ensemble, l'approche d'ajout d'hydrogène au méthane semble offrir une solution viable vers un carburant sans carbone.

Mots-clés : moteur à turbine à gaz, combustion enrichie en hydrogène, écoulement structuré de type swirl, dynamique des fluides numérique, zone de recirculation interne

TABLE OF CONTENTS

	Page
INTRODUCTION	1
CHAPTER 1 LITERATURE REVIEW AND RESEARCH OBJECTIVES	5
1.1 Introduction.....	5
1.2 Combustor's configurations.....	5
1.2.1 Lean premix combustors.....	6
1.2.2 Favoured temperature for minimum NO _x and CO emissions.....	7
1.3 Survey of publications	8
1.3.1 Experimental studies.....	8
1.3.2 Numerical studies.....	10
1.3.2.1 DNS and LES approaches.....	11
1.3.2.2 RANS approach	13
1.4 Literature review conclusions	15
1.5 Research objectives.....	18
CHAPTER 2 COMBUSTOR CFD NUMERICAL MODEL	19
2.1 Introduction.....	19
2.2 CFD model structure.....	20
2.3 Governing equations	21
2.3.1 Cold flow model	21
2.3.1.1 Turbulence model	22
2.3.2 Non-reactive flow model	24
2.3.3 Reactive flow mode	25
2.3.3.1 Flamelet model.....	25
2.3.3.2 NO _x sub-model.....	29
2.3.3.3 Radiation sub-model	30
2.4 Boundary conditions	32
2.5 Discretization, solution, and initialization	34
2.6 Model geometry	35
2.7 Mesh structure.....	38
2.7.1 Mesh strategy	38
2.7.2 Mesh configuration	38
2.7.3 Grid independence test (Grid Convergence Index)	41
2.8 Processing resources	45
2.9 Chapter conclusions	45
CHAPTER 3 CFD NUMERICAL MODEL VALIDATION	47
3.1 Introduction.....	47
3.2 CFD model validation.....	47
3.2.1 Validation of cold flow	47
3.2.1.1 Quantitative analysis.....	48

3.2.2	Validation of non-reactive flow	55
3.2.2.1	Different non-reactive flow equivalence ratios.....	57
3.2.3	Validation of reactive flow ($\phi = 0.65$)	59
3.2.3.1	Reactive flow aerodynamics	59
3.2.3.2	Reactive flow chemical data	62
3.3	Chapter conclusions	64
CHAPTER 4 HYDROGEN-ENRICHED COMBUSTION		65
4.1	CFD reactive flow model modification with respect to hydrogen addition.....	65
4.2	Effect of hydrogen addition	65
4.2.1	H ₂ addition effect on AFT.....	66
4.2.2	H ₂ addition effect on the global flow pattern and vorticity	67
4.2.3	H ₂ addition effect on the flame shape	72
4.2.4	H ₂ addition effect on the main species concentrations (CH ₄ , H ₂ , O ₂ , CO ₂ , CO, and H ₂ O).....	75
4.2.5	H ₂ addition effect on the burnt temperature (with radiation).....	77
4.2.6	H ₂ addition effect on NO _x emissions	78
4.3	Chapter discussion and conclusions.....	85
CHAPTER 5 SWIRL INTENSITY		89
5.1	CFD model geometry modification with respect to swirl intensity.....	89
5.2	Cold and reactive flow analyses for different swirl angles.....	90
5.2.1	Cold flow analysis.....	91
5.2.2	Reactive flow analysis (CH ₄ -air combustion at $\phi = 0.7$)	94
5.2.2.1	Reactive flow aerodynamics	94
5.2.2.1	Reactive flow chemical data	102
5.3	HEC study at high swirl level	107
5.3.1	H ₂ -swirl- ϕ effect on the global flow pattern and vorticity.....	107
5.3.2	H ₂ -swirl- ϕ effect on the Volumetric Heat Release rate (VHRR)	112
5.3.3	H ₂ -swirl- ϕ effect on the flame shape	114
5.3.4	H ₂ -swirl- ϕ effect on the burnt temperature (with radiation).....	117
5.3.5	H ₂ -swirl effect on emissions	119
5.3.6	H ₂ -swirl- ϕ effect on the turbulent premixed combustion regime	124
5.4	Chapter conclusions	126
CONCLUSION		127
FUTURE WORK		129
APPENDIX I MORE VALIDATION RESULTS.....		131
APPENDIX II UNSTABLE RESULTS.....		141
BIBLIOGRAPHY.....		145

LIST OF TABLES

		Page
Table 1.1	Summary of the literature studied hydrogen, swirl, ϕ , and turbulence combinations	17
Table 2.1	Fuel mass flow rate variation vs. equivalence ratio in CFD, base case in bold	32
Table 2.2	Applied fluid, thermal, and turbulent boundary conditions used in CFD ($\phi = \mathbf{0.65}$)	33
Table 2.3	Optimized meshing configuration specifications	39
Table 2.4	Meshes used for the Grid Convergence Index (GCI) calculations	41
Table 2.5	GCI results, including the apparent order, P_{GCI} , and errors (GCI_{32} & GCI_{21})	44
Table 4.1	Temperature and NO_x at the burner's outlet versus HVR, case $\phi = 0.7$	82
Table 4.2	Power scaling and inlet conditions for the real burner, lab burner, and restricted lab-scale burner	86
Table 4.3	Hydrogen addition phenomenological concept according to the study approach	87
Table 5.1	Swirl intensity change with respect to swirl vanes angle	90
Table 5.2	Carbon atom (C) mass balance between the inlet CH_4 and outlet CO_2 for the basic swirl configuration at $\phi = 0.7$ and HVRs up to 90%	123
Table 5.3	Carbon atom (C) mass balance between the inlet CH_4 and outlet CO and CO_2 for the three swirl configuration (50° , 55° , and 60°) at $\phi = 1$ and HVRs up to 50%	123

LIST OF FIGURES

	Page
Figure 0.1	Canada's greenhouse gas emissions map Taken from Environment and Climatic Change Canada (2015)1
Figure 1.1	Non-premixed (left), partially premixed (middle),and fully premixed (right) combustor configurations6
Figure 1.2	LP combustors generic flow pattern (left) and favoured temperature range (right) Taken from Turns (2000) and Lefebvre (1998).....7
Figure 1.3	Sample of results showing the visible flame vs. numerical flame (OH radical) Taken from Ali <i>et al.</i> (2020).....13
Figure 1.4	Sample of results showing the visible flame vs. numerical one (in terms of temperature) and meshing concept Taken from Samiran <i>et al.</i> (2019).....15
Figure 2.1	CFD model progression map19
Figure 2.2	CFD basic equations, main models, and sub-models map.....20
Figure 2.3	2D distribution of radiative emissivity and wall temperature applied to the CFD boundaries34
Figure 2.4	Free exhaust atmospheric burner tested by Taupin (2003) (top) and a longitudinal cut-out of the swirler with bluff body (bottom)37
Figure 2.5	Whole CFD model meshing configuration (≈ 2 M cells)40
Figure 2.6	Meshed swirler surfaces.....40
Figure 2.7	Region of Interest (ROI) including the points where the GCI study is conducted43
Figure 3.1	3D cold flow global flow field inside the combustion chamber48
Figure 3.2	Comparisons of the cold flow normalized axial (left) and tangential (right) velocities at the combustion chamber entry, Taupin (2003) (red) and CFD (blue).....49
Figure 3.3	Cold flow tangential velocity contours inside the ROI measured by Taupin (2003) (left) and predicted by CFD (right).....49

Figure 3.4	Cold flow normalized axial velocity radial profiles at $Z/D = 0.22$ (top), $Z/D = 1.22$ (middle), and $Z/D = 4.33$ (bottom).....	51
Figure 3.5	Cold flow normalized radial velocity radial profiles at $Z/D = 0.22$ (top), $Z/D = 1.22$ (middle), and $Z/D = 4.33$ (bottom).....	52
Figure 3.6	Cold flow normalized tangential velocity radial profiles at $Z/D = 0.22$ (top), $Z/D = 1.22$ (middle), and $Z/D = 4.33$ (bottom)	53
Figure 3.7	Cold flow axial velocity evolution along the combustor longitudinal axis, Taupin (2003) in red dots and CFD in blue line	54
Figure 3.8	Non-reactive flow equivalence ratio radial profiles at four axial locations, Taupin (2003) in red and CFD in blue	56
Figure 3.9	Non-reactive flow equivalence ratio radial profiles at the combustion chamber entry ($Z/D = 0.01$) for $\phi = 0.6$ (top left), 0.63 (middle left), 0.65 (bottom), 0.68 (top right), and 0.7 (middle right)	58
Figure 3.10	Reactive flow ($\phi = 0.65$) normalized axial velocity radial profiles at $Z/D = 0.22$ (top), $Z/D = 1.22$ (middle), and $Z/D = 4.33$ (bottom)	60
Figure 3.11	Reactive flow ($\phi = 0.65$) normalized radial velocity radial profiles at $Z/D = 0.22$ (top), $Z/D = 1.22$ (middle), and $Z/D = 4.33$ (bottom)	61
Figure 3.12	Flame shape validation versus Taupin (top) in terms of the CFD predicted AFT (middle) and OH radical (bottom), methane-air combustion case at $\phi = 0.65$	63
Figure 4.1	AFT versus HVR plot at $\phi = 0.7$ where each point represent the maximum CFD-predicted temperature inside the wake region for methane and HEC with HVRs = 25, 50, 75, and 90%	66
Figure 4.2	2D streamlines distribution inside the ROI at $\phi = 0.7$ mapped over the axial velocity contours for methane (top left) and HEC with HVR = 25% (top right), 50% (bottom left), and 90%	68
Figure 4.3	2D streamlines distribution inside the ROI at $\phi = 0.7$ mapped over the contours of temperature (up) and OH radical (down) for methane (top left) and HEC with HVR = 25% (top right), 50% (bottom left), and 90% (bottom right).....	69
Figure 4.4	3D streamlines distribution inside the entire combustion chamber at $\phi = 0.7$ (colored by the axial velocity) for methane (top) and HVR = 75% (bottom)	70

Figure 4.5	Vorticity magnitude contours inside the ROI at $\phi = 0.7$ for methane (top left) and HEC with HVR = 25% (top right), 50% (bottom left), and 90% (bottom right)72
Figure 4.6	2D flame visualization inside the ROI using OH radical (up) and c (down) at $\phi = 0.7$ for CH ₄ (top left) and HEC with HVR = 25% (top right), 50% (bottom left), and 90% (bottom right) with a 3D visualization of HVR = 25% (base left) and 90% (base right)74
Figure 4.7	Mass fractions of CH ₄ (top left), H ₂ (top right), O ₂ (middle left), CO ₂ (middle right), H ₂ O (bottom left), and CO (bottom right) for HEC at $\phi = 0.7$ with HVR = 25% (up) and 90% (down)76
Figure 4.8	2D temperature distribution inside $2/3 L_{cc}$ at $\phi = 0.7$ for methane (top left) and HEC with HVR = 25% (top right), 50% (bottom left), and 90% (bottom right)78
Figure 4.9	Plots of temperature (top) and NO _x (bottom) along the burner's longitudinal axis at $\phi = 0.7$ for methane and HEC with different HVRs: 25, 50, 75, and 90%80
Figure 4.10	2D NO _x distribution inside the entire combustion chamber at $\phi = 0.7$ for methane (top) and HEC with HVR = 25% (middle) and 90% (bottom)79
Figure 4.11	2D distributions of temperature, NO, NNH, and NO ₂ (stacked clockwise) inside the ROI for methane flame at $\phi = 0.7$84
Figure 4.12	2D distributions of temperature, NO, NNH, and NO ₂ (stacked clockwise) inside the ROI for HEC with 25% H ₂ at $\phi = 0.7$84
Figure 4.13	2D distributions of temperature, NO, NNH, and NO ₂ (stacked clockwise) inside the ROI for HEC with 90% H ₂ at $\phi = 0.7$85
Figure 5.1	Combustor model geometry modification with respect to the swirl intensity in terms of the swirl angle (α)89
Figure 5.2	Cold flow analysis in terms of the axial velocity distribution inside the ROI for the 52°, 55°, and 60° swirl configurations, from top to bottom, respectively92
Figure 5.3	Cold flow analysis in terms of the 2D velocity vectors (colored by u) distribution inside the ROI for the basic (50°, top) and highest (60°, bottom) swirl configurations93

Figure 5.4	Reactive flow analysis using the 2D streamlines (mapped over u) inside the ROI of the 50° (top) and 60° (bottom) swirl configurations for CH ₄ -air combustion at $\phi = 0.7$95
Figure 5.5	Pressure plots along the burner's longitudinal axis for CH ₄ -air combustion at $\phi = 0.7$ inside the 50° and 60° swirl configurations, where $P_{\text{atm.}} = 101325$ Pa.....96
Figure 5.6	Centrifugal force plots versus R/D (at three axial heights) for CH ₄ -air combustion at $\phi = 0.7$ inside the 50° and 60° swirl configurations.....96
Figure 5.7	Reactive flow analysis using the total velocity distribution inside the ROI of the 50° (top) and 60° (bottom) swirl configurations for CH ₄ -air combustion at $\phi = 0.7$98
Figure 5.8	Reactive flow analysis using the radial velocity distribution inside the ROI of the 50° (top) and 60° (bottom) swirl configurations for CH ₄ -air combustion at $\phi = 0.7$99
Figure 5.9	Reactive flow analysis using the axial velocity fluctuation (u) distribution inside the ROI of the 50° (top) and 60° (bottom) swirl configurations for CH ₄ -air combustion at $\phi = 0.7$100
Figure 5.10	Reactive flow analysis using the vorticity magnitude distribution inside the ROI of the 50° (top) and 60° (bottom) swirl configurations for CH ₄ -air combustion at $\phi = 0.7$101
Figure 5.11	Reactive flow analysis using the volumetric heat release rate distribution inside the ROI of the 50° (top) and 60° (bottom) swirl configurations for CH ₄ -air combustion at $\phi = 0.7$102
Figure 5.12	Reactive flow (CH ₄ -air combustion at $\phi = 0.7$) c distribution inside the ROI of the 50° (top) and 60° (bottom) swirl configurations....103
Figure 5.13	Reactive flow (CH ₄ -air combustion at $\phi = 0.7$) AFT contours inside the ROI of the 50° (top) and 60° (bottom) swirl configurations....104
Figure 5.14	Reactive flow (pure methane, $\phi = 0.7$) 2D temperature (with radiation) contours inside the ROI for the 50° (top) and 60° (bottom) swirl configurations105
Figure 5.15	Reactive flow (pure methane, $\phi = 0.7$) 3D temperature (with radiation) iso-surfaces at 300 (blue), 1300 (green), and 1800 K (orange) for the 50° (top) and 60° (bottom) swirl configurations106

Figure 5.16	2D streamlines distribution inside the ROI at $\phi = 0.7$ mapped over the temperature (up) and OH radical (down) for methane and HEC with HVRs = 25, 50, and 90% (from top to bottom)108
Figure 5.17	2D streamlines distribution inside the ROI mapped over the axial velocity for the reference CH ₄ case (top) compared to HEC with HVR = 60% (bottom) at $\phi = 0.7$ (left) and 1 (right) for the 50° (up) and 60° (down) swirl configurations110
Figure 5.18	Vorticity contours inside the ROI for the reference methane case (top) compared to HEC with HVR = 60% (bottom) at $\phi = 0.7$ (left) and 1 (right) for the 50° (up) and 60° (down) swirl configurations111
Figure 5.19	Volumetric heat release rate contours inside the ROI of the 50° (up) and 60° (down) swirl configurations at $\phi = 0.7$ (top) and 1 (bottom) for the reference methane case and HEC with HVR = 25, 50, and 60% (from left to right)113
Figure 5.20	OH mass fraction contours inside the ROI of the 50° (up) and 60° (down) swirl configurations at $\phi = 0.7$ for the reference methane flame (top left) compared to HEC with HVR = 25% (top right), 50% (bottom left), and 60% (bottom right)115
Figure 5.21	Progress variable contours inside the ROI for the reference methane case (top) compared to HEC with HVR = 60% (bottom) at $\phi = 0.7$ (left) and 1 (right) for the 50° (up) and 60° (down) swirl configurations116
Figure 5.22	2D temperature contours inside the ROI for the reference methane case (top) compared to HEC with HVR = 60% (bottom) at $\phi = 0.7$ (left) and 1 (right) for the 50° (up) and 60° (down) swirl configurations118
Figure 5.23	NO _x versus the temperature at the burner outlet for the 50°, 55°, and 60° swirl configurations and HVRs: 0, 25, 50, 75, and 90%, from left to right, respectively, considering radiation (top) and adiabatic (bottom), case $\phi = 0.7$120
Figure 5.24	NO (left axis) and CO (right axis) versus the temperature at the burner outlet for the 50°, 55°, and 60° swirl configurations and HVRs: 0, 25, 50, 75, and 90%, from left to right, respectively, considering radiation (top) and adiabatic (bottom), case $\phi = 1$122
Figure 5.25	Borghi diagram (u'/S_L versus l_o/δ)125

Figure 5.26	Samples of the generated networks for swirl-HVR couples of 50°-25% (top) and 60°-50% (bottom) at $\varphi = 0.7$129
-------------	------------------------------------------------------------------------------------------------------------------------------

LIST OF ABBREVIATIONS

0D	Zero-Dimensional
1D	One-Dimensional
2D	Two-Dimensional
3D	Three-Dimensional
AFT	Adiabatic Flame Temperature
AMG	Algebraic Multi Grid
B.C.	Boundary Conditions
BOR	Burnout Region
CFD	Computational Fluid Dynamics
cnds	Conditions
CPU	Central Processing Unit
CRN	Chemical Reactor Network
CRZ	Corner Recirculation Zone
DE	Differential Equation
DLE	Dry Low Emissions
DNS	Direct Numerical Simulation
DOM	Discrete Ordinate Model
EBU	Eddy Break Up

EDC	Eddy Dissipation Concept
ETS	École de technologie supérieure
FGM	Flamelet Generated Manifold
GCI	Grid Convergence Index
GHG	Greenhouse Gas
GRI	General Research Institute
GT	Gas Turbine
GTE	Gas Turbine Engine
HEC	Hydrogen-enriched Combustion
HOI	Height of Interest
HRR	Heat Release Ratio
HTKE	High Turbulent Kinetic Energy
HVR	Hydrogen Volumetric Ratio
IEA	International Energy Statistics
IRZ	Inner Recirculation Zone
ISP	Intermediate Steady Propagation
LES	Large Eddy Simulation
LFC	Laminar Flame Concept
LP	Lean Premixed

LPC	Lean Premixed Combustion
LPP	Lean Premixed Prevapourized
MTC	Military Technical College
ODE	Ordinary Differential Equation
PDE	Partial Differential Equation
PDF	Probability Distribution Function
PFR	Plug Flow Reactor
PPM	Parts Per Million
PSR	Perfect Stirred Reactor
RANS	Reynolds Averaged Navier Stockes
RMS	Root Mean Square
ROI	Region Of Interest
RTE	Radiative Transport Equation
STARCCM+	Commercial CFD code (SIEMENS PLM)
TCI	Turbulence Chemistry Interaction
TDR	Turbulent Dissipation Rate
TFC	Turbulent Flame speed Closure
TFT-CDF	Laboratoire de Thermo-Fluide pour le Transport
TKE	Turbulent Kinetic Energy

VHRR	Volumetric Heat Release Rate
WSGGM	Weighted Sum of Gray Gases Model

LIST OF SYMBOLS AND MEASURING UNITS

Chemical species

$C_{12}H_{23}$	Jet-A ₁
CH	Methylidyne radical
CH_2	Methylene radical
CH_3	Methyl radical
CH_4	Methane
CN	Cyano radical
CO	Carbon monoxide
CO_2	Carbon dioxide
H	Hydrogen atom
H_2	Hydrogen
H_2O	Water
HCN	Hydrogen cyanide
N	Nitrogen atom
N_2	Nitrogen
N_2O	Nitrous oxide
NCN	Diradical cyanonitrene
NH	Nitrogen monohydride

XXVI

NO	Nitrogen monoxide (nitric oxide)
NO ₂	Nitrogen dioxide
NO _x	Nitrogen oxides emission
O	Oxygen atom
O ₂	Oxygen
OH	Hydroxyl radical

Measuring units (International System)

B	Byte (data capacity)
g·s ⁻¹	Gram per second (flow rate)
J	Joule (work)
J·s ⁻¹	Joule per second (molar energy)
K	Kelvin (temperature)
m	Meter (distance)
m·s ⁻¹	Meter per second (velocity)
Pa, atm, bar	Pascal (pressure)
s	Second (time)
W	Watt (power)

Greek Letters

ρ	Density
σ	Stress tensor
μ	Dynamic viscosity
α	Swirl vanes angle
φ	Equivalence ratio
Δ	Difference
ν	Kinematic viscosity
ε	Turbulent kinetic energy dissipation rate
ω	Tangential velocity

Latin Letters

\bar{V}	Velocity vector
F_b	Body force/unit volume
S_E	Energy source/unit volume
A0	Main research objective
A1	First research sub-objective
A2	Second research sub-objective
A3	Third research sub-objective

XXVIII

c	Progress variable
c_{var}	Progress variable variance
D	Strain tensor
E	Total energy/unit mass
I	Identity tensor
k	Turbulent kinetic energy
m	Mass
n	Number of moles
P	Pressure
q	Heat flux
R	Ideal gas constant
T	Temperature
T	Viscous stress tensor
u	Axial velocity
v	Radial velocity
X	Mole fraction
Y	Mass fraction
Y_i	Mass fraction of species i
J_i	Laminar (or molecular) diffusive flux of species i

Other symbols

F	Mixture fraction
f_{var}	Mixture fraction variance
$\nabla(\text{scalar})$	Gradients (grad)
$\nabla \cdot (\text{vector})$	Divergence (div)
$\nabla \times (\text{vector})$	Curl (rotation)
Δ	Laplace operator

Dimensionless Numbers and its physical meaning

Da	Damköhler number	Turbulent mixing time scale over chemical time scale
Ka	Karlovitz number	Chemical time scale over Kolmogorov time scale
Pr	Prandtl number	Viscous diffusivity over heat (thermal) diffusivity
Pr _t	Turbulent Prandtl number	Viscous diffusivity over heat (thermal) diffusivity (considering the turbulent velocity)
Re	Reynolds number	Inertia force over viscous force
Re _t	Turbulent Reynolds number	Inertia force over viscous force (considering the turbulent velocity)
S, S _g	Geometric Swirl number	Axial flux of angular momentum (tangential velocity) over axial flux of axial momentum (axial velocity)

XXX

Sc	Schmidt number	Viscous diffusivity over mass diffusivity
Sc _t	Turbulent Schmidt number	Viscous diffusivity over mass diffusivity (considering the turbulent velocity)
Le	Lewis number	Heat (thermal) diffusivity over mass diffusivity

INTRODUCTION

Over the last two decades, industrial gas turbines attracted a great deal of attention for the generation of power, including heat and electricity. However, burning fossil fuels have several ecological implications. For instance, in Canada, power generation accounts for about 45% of the total Greenhouse Gas (GHG) emissions into the atmosphere, as shown in Figure 0.1, (Environment and Climatic Change Canada, 2015). Such emissions, including NO_x and CO₂, are considered the main culprits at the root of the well-known global warming and represent a profound danger that must be taken into consideration urgently. On the other hand, excess burning of fossil fuel - for power generation purposes - results in a sharp depletion of the fossil fuel reserves, (International Energy Agency, 2018), which urges finding alternative fuels to be used in the near future.

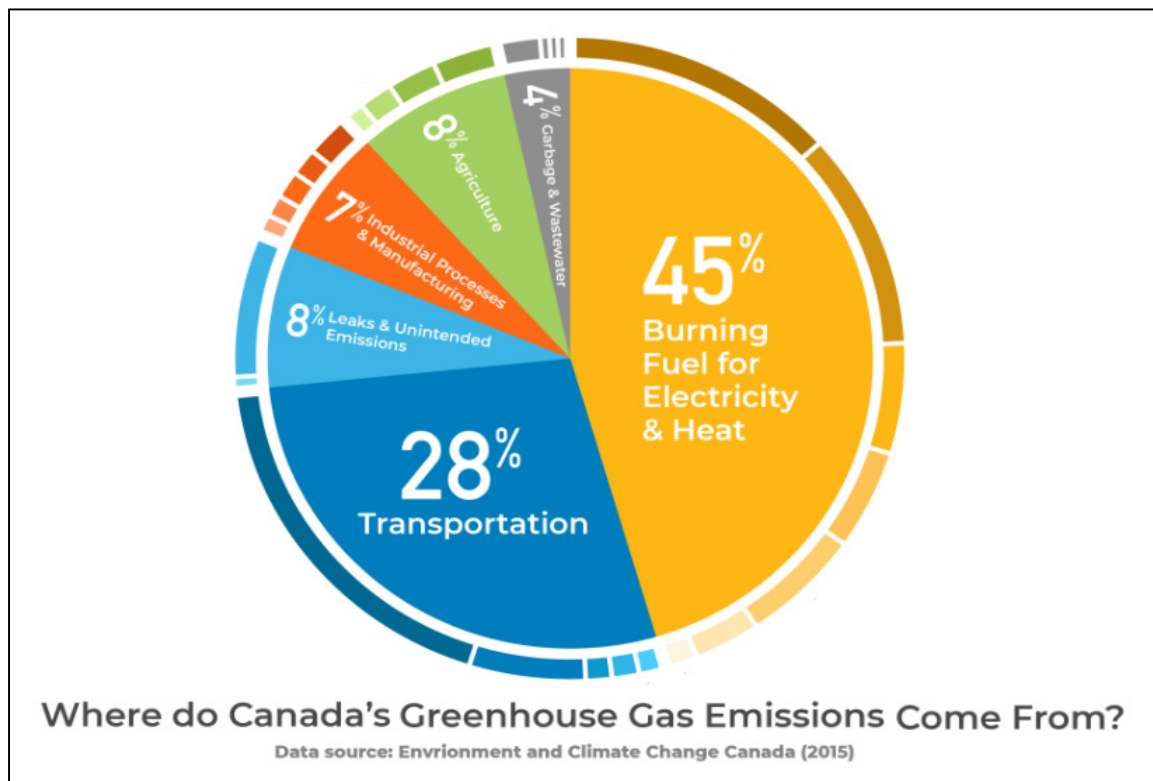


Figure 0.1 Canada's greenhouse gas emissions map
Taken from Environment and Climatic Change Canada (2015)

Given these problems (increased emissions and limited reserves), the transfer to alternative/blended fuels is thus necessary. This transfer shall guarantee the proper operation of existing industrial gas turbines, powered by new energy resources, with only partial or minimal design modifications. The main challenge in this context is that alternative fuels have distinct properties, as compared to conventional ones. On the other hand, most industrial GTEs operate at high turbulence and swirl levels. Considering all of the above, determining the optimum blended fuel composition and swirl intensity is considered undoubtedly an arduous task. To accomplish this task, a substantial understanding of the interrelation between fluid dynamics, thermodynamics, chemical kinetics, and heat transfer is essential.

One approach to help with the transition to alternative fuels involves the use of Hydrogen-enriched Combustion (HEC), in which hydrogen is blended with a traditional hydrocarbon to be used as the prime fuel. Hydrogen-blended fuel could be produced in different ways, including through the gasification of coal or biomass and industrial processes, such as steel production. Recently, hydrogen has come to be used in different combustion applications, due to its higher reactivity (compared to fossil fuels) and ability to reduce carbon-based emissions. However, more investigations about the characteristics of HEC are still needed, especially when hydrogen is injected into industrial swirling configurations. The aim of this dissertation is to numerically identify the effects of hydrogen addition and swirl intensity on combustion characteristics and emissions. Computational Fluid Dynamics (CFD) will be used herein to study the hydrogen-enriched methane-air combustion inside a laboratory-scale industrial gas turbine combustor.

This dissertation consists of the following five chapters: 1. Literature review and research objectives, 2. Combustor CFD numerical model, 3. CFD numerical model validation 4. Hydrogen-enriched combustion, and 5. Swirl intensity. In Chapter 1, a literature review will be presented and the research objectives will be defined. Next, the numerical model of the combustor will be presented in Chapter 2 followed by the model validation in Chapter 3. Finally, the effect of hydrogen addition to methane on the combustion process and emissions

will be identified in Chapter 4, before the impact of swirl intensity on the combustion process and emissions is studied for a few specific hydrogen addition and equivalence ratios in Chapter 5.

CHAPTER 1

LITERATURE REVIEW AND RESEARCH OBJECTIVES

1.1 Introduction

In the context of hydrogen-enriched combustion in gas turbine combustors, the addition of hydrogen and the swirl intensity influence the combustion characteristics, such as the flame shape, length, temperature, pollutant emissions, etc. Hence, a review of the effect of these two factors (hydrogen addition and swirl intensity) on the combustion process and emissions is presented. Particular attention will be paid to studies conducted using CFD simulations, as that is the study approach adopted in the present work. At the end of this chapter, conclusions and outcomes of the literature review will be highlighted, allowing to define the research objectives of this work.

1.2 Combustor's configurations

GTEs possess different configurations with respect to how fuels and oxidizers mix in the combustion chamber. The first configuration consists of non-premixed combustors, characterized by two regions, namely, a primary zone and a secondary zone. In the primary, fuel is injected and burned with air under near-stoichiometric conditions, without mixing before reaching the flame, while in the latter; a secondary air stream is used to convolute and dilute the primary zone in order to complete the combustion process and reduce the product's temperature (Turns, 2000, p. 451).

The second approach employs premixed combustors, which are used to diminish the regions of high temperature and NO_x (Turns, 2000, p. 452). As the name implies, the goal is to create a premixed fuel-air mixture before combustion take place. The mixing process occurs either within the combustion chamber or before entering the combustion chamber. For the first configuration, the fuel-air mixing process occurs very fast, however, it may exhibit a non-premixed area creating a diffusion flame, due to insufficient mixing inside the combustion

chamber. In this case, the flame is referred to as “partially-premixed flame” (Turns, 2000, p. 452). The second configuration involves fuel and air being mixed inside a pre-mixer before entering the combustion chamber, and the flame produced thus called “fully premixed flame”. Such configurations (fully premixed) are most commonly used in industrial combustors/burners, because they are known for their reduced emissions (Lefebvre, 1998, p. 23). Used fuel can be ejected either in liquid or gaseous state, making the combustor respectively Lean Premix Prevapourized (LPP) or Lean Premix (LP). For the liquid fuel combustor, the fuel injection system should guarantee that liquid fuel evaporates completely before it enters into the combustion chamber. Figure 1.1 shows the configurations of the three combustors, where the blue arrows represent air and red arrows represent fuel.

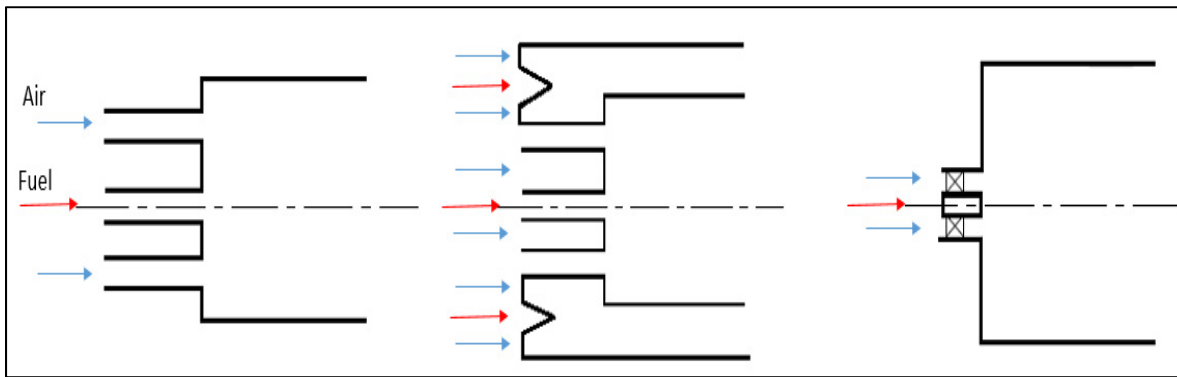


Figure 1.1 Non-premixed (left), partially-premixed (middle), and fully premixed (right) combustor configurations

1.2.1 Lean premix combustors

An LP combustor consists of a swirler (pre-mixer) combined with a combustion chamber. Figure 1.2 (left) shows the generic flow pattern of LP combustors, consisting of Inner Recirculation zones (IRZ), due to the existence of a swirler, and Corner Recirculation zones (CRZ), due to the sudden expansion. Such a configuration enhances the flow separation and creates recirculation zones, which in turn stabilizes the flame. IRZ serves as a flame stabilization mechanism, where hot products are mixed with the incoming fuel-air mixture, and is thus considered as one of the most important flow features of swirl stabilized flames

(Huang & Yang, 2005; Huang, Sung, Hsieh, & Yang, 2003). Swirl stabilization has been frequently used in industrial burners and gas turbine combustors (Turns, 2000, p. 473)

The prime drawbacks of LP combustors are the required time and quality of the mixing process. Increases of the former can cause self-ignition, especially at elevated pressures and temperatures, whereas a lack of the latter affects the combustion stability.

1.2.2 Favoured temperature for minimum NO_x and CO emissions

The flame temperature inside LP combustors doesn't exceed 1900 K and hence nitric oxides (NO_x), which strongly follow temperature, are lowered (Lefebvre, 1998, p. 23). Furthermore, the increase in residence time - due to inner recirculation - does not only influence the NO_x formation, but it also boosts the occurrence of a complete combustion process, in which carbon monoxide (CO) has enough time to completely convert into carbon dioxide (CO_2) (Lefebvre, 1998, p. 24). The net result is that both NO_x and CO can be minimized simultaneously with an appropriate temperature. Figure 1.2 (right) shows the favoured temperature range for minimizing NO_x and CO emissions with hydrocarbon fuels.

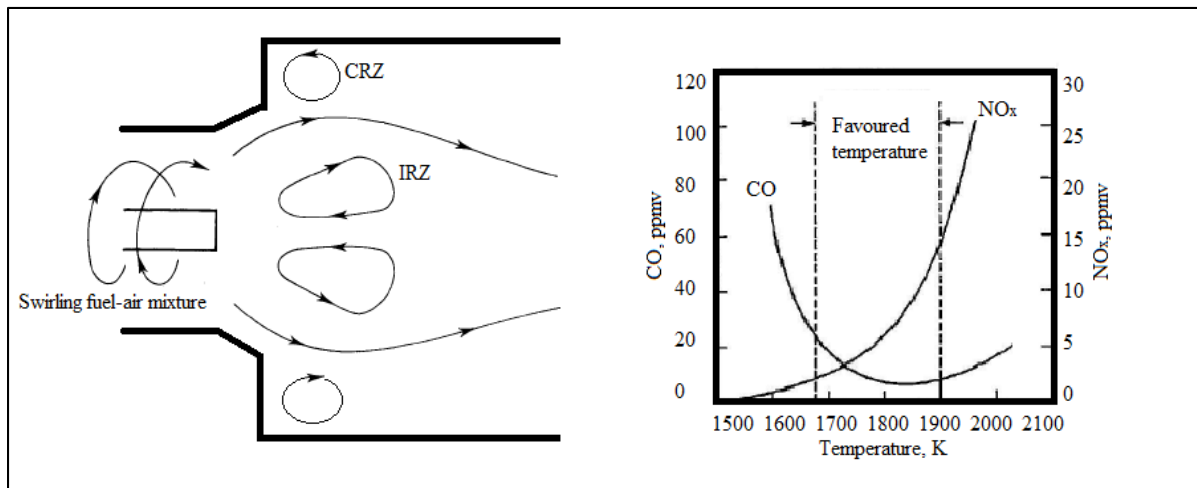


Figure 1.2 LP combustors generic flow pattern (left) and favored temperature range (right)
Taken from Turns (2000) and Lefebvre (1998)

1.3 Survey of publications

When investigating combustion inside LP combustors, it has been reported that the combustion process and emissions are influenced by hydrogen addition and swirl intensity. This section presents the main findings related to such effects, obtained experimentally and numerically.

1.3.1 Experimental studies

Experimental measurements identifying the effect of hydrogen on the different combustion parameters cover different subjects. For example, Schefer *et al.* (2002) studied the effect of hydrogen addition (0, 12, 22, and 29%, volume ratio) on the lean methane-air confined combustion under atmospheric pressure and temperature. All measurements were performed for a unique swirl number ($S = 0.82$), using a swirl angle of 45° . The inlet bulk velocity varied between 8 and 22 m/s, while its maximum fluctuation was 11 m/s. The authors reported a reduction in CO concentration with hydrogen addition, with no adverse effect on NO_x . In addition, measurements showed that addition of a moderate amount of hydrogen to methane changes the flame structure, which appeared shorter and more robust than methane flames.

Schefer (2003) studied the effect of hydrogen addition (0, 10, and 20%, volume ratio) on the lean, stoichiometric, and rich methane-air combustion (ϕ varied from 0.5 to 2) inside a swirl stabilized unconfined burner. All measurements were performed for a unique swirl number ($S = 0.76$), using a swirl angle of 45° , while the inlet bulk velocity varied between 8 and 22 m/s. OH radicals were measured to assess the lean stability limit. The author reported that enriching the methane-air combustion by 20% H_2 increases the OH concentration and extends the lean stability limit. He further reported that the flame was lifted from the swirler surface under rich conditions; while conversely, the flame was attached to the burner surface for stoichiometric and lean combustions.

Shy *et al.* (2008) studied the effect of hydrogen addition (0, 10, 20, and 30% H₂, volume ratio) with equivalence ratios of 0.6, 0.7, and 0.8 on the turbulent flame speed of the methane-air combustion inside a cruciform burner at atmospheric pressure and temperature. They also studied the impact of turbulent intensity, defined as the characteristic velocity fluctuation over the laminar flame speed (u'/S_L), which reached a maximum value of 40. According to measurements, intensive turbulence intensity can highly affect the canonical structure of the turbulent premixed flame and thus the turbulent burning rate. In addition, results revealed that the high reactivity and diffusivity of hydrogen assists the reaction zone to remain thin.

Kim *et al.* (2009 a) studied the effect of swirl angle (30°, 45°, and 60°) on the hydrogen-enriched methane-air combustion (0, 4, and 9% H₂, volume ratio) in a laboratory-scale unconfined combustor, where combustion took place at $\phi = 0.7$. They reported that, hydrogen addition moves the flame upstream at low swirl strength (swirl angle of 30°), but this effect decreases with an increasing swirl angle. The authors also reported that a higher hydrogen combustibility not only promotes faster chemical reaction and raises the reaction zone temperature, but also reduces the residence time of hot products in the reaction zone. The end result, at lower swirl strength, is a decrease in NO concentration with increasing hydrogen addition. At higher swirl strength (swirl angles of 45° and 60°), the NO concentration increases with an increase in the hydrogen content in the fuel mixture due to the higher flame temperature and decreased recirculation zone intensity. Kim *et al.* (2009 b) further pursued the same study, but with a confined flame. Under this new condition, the lean stability limit was extended by adding hydrogen and the NO_x emission increased for a constant Adiabatic Flame Temperature (AFT).

Imteyaz *et al.* (2018) experimentally studied the behaviour of a stoichiometric hydrogen-enriched oxygen-methane premixed flame in a model gas turbine combustor at atmospheric pressure and temperature. The studied swirl intensity and angle were 0.98 and 55°, respectively, while hydrogen was varied between 0 and 50%, by an increment of 10%. Three inlet bulk velocities were tested: 4.4, 5.2, and 6 m/s, which resulted in a wrinkled flame as

later confirmed by Nemitallah, Imteyaz, Abdelhafez, & A.Habib (2019). Results indicated that the Reynolds number (based on the inlet bulk velocity) plays an important role in controlling the flame stability. In addition, the authors reported that the effect of hydrogen addition on the flame characteristics was more tangible for H₂ addition from 20% to 50%.

Khalil *et al.* (2012) studied the feasibility of using syngas (a mixture of CH₄, H₂, CO, CO, and N₂) with a premixed and a non-premixed combustor configuration, primitively designed for methane-air combustion. NO and CO emissions were measured for an inlet preheating temperature of 600 K. The presence of hydrogen in the syngas alters the AFT as a function of its concentration. They showed a favourable operation of premixed combustors when syngas was utilized, without any modifications to the combustors design. Moreover, lower emissions were reported with syngas combustion and premix combustion showed lower NO and CO emissions when compared to the non-premix.

Yilmaz *et al.* (2019) conducted an experimental study on the combustion characteristics (temperature and emissions) of a syngas (mixture of CH₄, H₂, CO, and CO₂) in a premixed combustor with a variable swirl number ranging from 0.2 to 1.6, and with an increment of 0.2. Combustion took place under ambient temperature at three equivalence ratios (0.6, 0.8, and 1). Hydrogen Volumetric Ratio (HVR, hereinafter) was varied between 30 and 40%, with an increment of 2.5% of the syngas fuel blend. Results revealed that the effect of the swirl number on the flame characteristics (temperature and emission) is not monotonous. However, the flame behavior is highly dependent on the equivalence ratio. Hence, the interaction between the equivalence ratio and the swirl number alters the combustion phenomenon.

1.3.2 Numerical studies

The second track present in the literature involves numerical modelling using CFD simulations that are reviewed and classified in terms of the approach used, either DNS and LES or RANS. Particular attention will be paid to the RANS approach.

1.3.2.1 DNS and LES approaches

Direct Numerical and Large Eddy Simulations (DNS and LES) are numerical modelling approaches that emphasize resolving a wide range of time scales and length scales. DNS is computationally expensive due to the smallest length scale resolved by this approach. For example, Hawkes & Chen (2004) studied the effect of hydrogen addition (HVR = 0 and 29%) on LP methane-air confined atmospheric combustion using a 2D DNS approach coupled with a reduced mechanism. A unique swirl condition ($S = 0.82$ and $\alpha = 45^\circ$) was studied, while the inlet bulk velocity was 15 m/s and an inlet turbulent intensity of 10% was used. A reduced mechanism consisting of 19 species and 15 reactions - based on the GRI 3.0 - was utilized to define the chemistry. The flame stability was quantified in terms of the turbulent flame speed. The authors reported that a higher flame speed, higher OH concentration, lower CO, and higher NO were observed for the hydrogen-enriched case, with HVR = 29%.

De & Achary (2012) studied the effects of swirl, premix, and combustion chamber geometry on the hydrogen-enriched methane premixed flame (only for 30% H₂) in a laboratory-scale unconfined combustor using a LES approach and a Thickened Flame Model (TFM), which is a LES combustion model in which the flame front is assumed to be artificially thickened. The combustor basic swirl angle was 45° and three swirl numbers (0.38, 0.82, and 1.76) were studied by changing the combustor's geometry, i.e. changing the bluff body and swirler diameters. Combustion took place under atmospheric pressure and temperature at $\phi = 0.7$. The inlet bulk velocity was 5.7 m/s, whereas the turbulent intensity was set at 10%. Two-step reduced kinetics were used for the methane combustion and were combined with a one-step hydrogen oxidation reaction into water. The results showed that a higher swirl intensity promotes upstream flame propagation and that hydrogen addition raises the reaction zone temperature, similarly to the experimental results of Shy *et al.* (2008); Kim *et al.*, (2009 a), presented earlier.

Guo *et al.* (2020) numerically studied the HEC of LP methane-air flame inside a swirl unconfined combustor with bluff body using LES and a TFM. Combustion took place at $\phi = 0.7$ with the studied swirl configuration being $S = 0.7$ and $\alpha = 45^\circ$. The inlet bulk velocity was 9.2 m/s. Three HVRs (0, 40, and 80%) were considered. The authors validated their numerical results with their own experimental work and a good agreement was found. Both numerical and experimental results showed that hydrogen addition not only increased the overall chemical reaction rate, but also changed the combustion intensity at the fuel outlet, from relatively weak to strong, highlighting the role of hydrogen in stabilizing the flame. Moreover, the authors reported that the next-generations of industrial combustors might operate with hydrogen blended fuel up to 90% H_2 , similarly to Day, Tachibana, Bell, Lijewski, Beckner, & Cheng (2012). Although micro combustion falls outside the scope of this dissertation, it is worth mentioning here that a similar conclusion was reached by Meziane & Bentebbiche (2019), who used up to 90% hydrogen to blend natural gas and fuel a micro GTE combustor.

Ali *et al.* (2020) numerically investigated stoichiometric hydrogen-enriched oxygen-methane combustion in a premixed swirl combustor using LES coupled with a partially premixed combustion model. Combustion took place at atmospheric pressure and temperature. The studied swirl configuration was $S = 0.98$ and $\alpha = 55^\circ$. Three HVRs were considered: 20, 40, and 60%. The inlet bulk velocity was 5.2 m/s. The Discrete Ordinate Model (DOM) was used to account for the heat transferred by radiation. A partially premixed combustion model modified for hydrogen addition and oxygen-methane combustion was employed. The OH radical was used to validate the flame shape, as shown in Figure 1.3, where the luminous images of flame (camera images on the left) were compared to the numerically generated flame (OH contours on the right). Results were presented for the cases with 40% H_2 (right half) and 60% H_2 (left half) for an inlet bulk velocity of air of 5.2 m/s, under stoichiometric burning conditions. Results showed that increasing HVR improves the reactivity of the mixture (i.e. accelerates the chemistry), which was also indicated by the higher OH concentration observed in the numerical flame shape. In addition, the particular flame microstructure is more governed by stoichiometry than by turbulence, which only affects the

flame macro-structure. This postulate is due to the low inlet bulk velocity (5.2 m/s) and the very fast chemical kinetics attributable to the presence of H_2 , which results in a wrinkled flame, similarly to Imteyaz, Nemitallah, Abdelhafez, & Habib (2018).

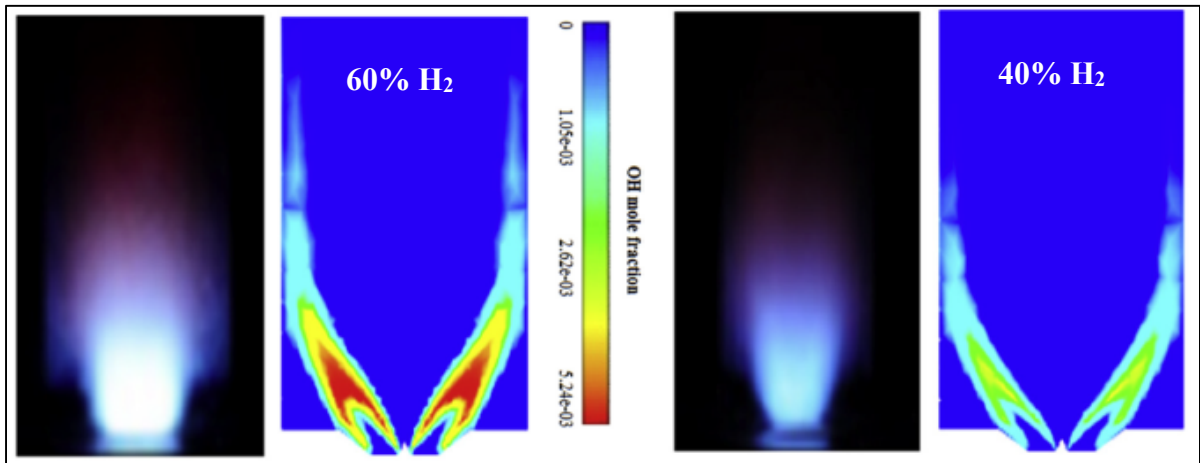


Figure 1.3 Sample of results showing the visible flame vs. numerical flame (OH radical)
Taken from Ali *et al.* (2020)

1.3.2.2 RANS approach

The Reynolds Averaged Navier Stokes (RANS) approach is a numerical modelling approach, in which an instantaneous property is decomposed into its time-averaged and fluctuating quantities. Unlike the DNS/LES approaches, the RANS approach allows considering a detailed chemistry when modelling a turbulent combustion process without excessive computational cost. Ilbas *et al.* (2016) performed a numerical study to investigate the effect of the swirl number ($S = 0 - 0.8$, with an increment of 0.2) on the combustion temperature and NO_x emission of two hydrogen-containing fuel blends inside a gas-fired combustor. Combustion took place under atmospheric pressure and temperature. The fuels used were pure methane, Coke oven gas (55% H_2 - 27% CH_4), and Town gas (51% H_2 - 21% CH_4). The $k-\epsilon$ realizable turbulence model and the Probability Distribution Function (PDF)/mixture fraction combustion model were used to model turbulence and combustion, respectively. The radiation effect was also considered using a simplified radiation model. Results showed that the temperature and NO_x levels of the Coke oven gas and Town gas were highly sensitive to

changes of swirl number. More specifically, when the swirl number increased from zero to 0.8, the overall NO_x increased as well. For swirl numbers 0.6 and 0.8, temperature levels decreased in the axial direction, but increased in the radial one.

Samiran *et al.* (2019) studied the combustion of syngas (mixture of 90% H_2 -CO, 5% CH_4 , and 5% CO_2 , volume ratio) inside a premixed swirling confined combustor. The combustion took place under atmospheric pressure and temperature. The studied swirl configuration was $S = 0.84$ and $\alpha = 45^\circ$. HVR varied in the H_2 -CO mixture as follows: 22.5, 40.5, 49.5, and 67.5%. The combustion process was studied at three equivalence ratios, namely, 0.6, 0.8, and 1. The turbulent intensity was 17%. Figure 1.4 (right) shows the meshed combustor, where three elements were used, namely, saturated, fine, and coarse. The high grid density of cells were constructed for the swirler and combustion chamber entry (with the high gradients of velocity, temperature, and species) and then became coarser when approaching the combustor's outlet. The grid had the size of minimum and maximum cells of 0.7 and 1 million, respectively. The temperature distribution (intermediate) inside the Region of Interest (ROI) was used to validate the previously captured flame shape (left), as also shown in Figure 1.4 for the case with 67.5% H_2 , under stoichiometric burning conditions. The k - ϵ turbulence model was combined with the Flamelet Generated Manifold (FGM) to model the turbulent combustion process. The detailed methane-air reaction mechanism GRI 3.0 was used to generate the flamelet table. The authors affirmed the superiority of the used RANS-FGM approach for modelling the turbulent combustion process over the other modelling approaches.

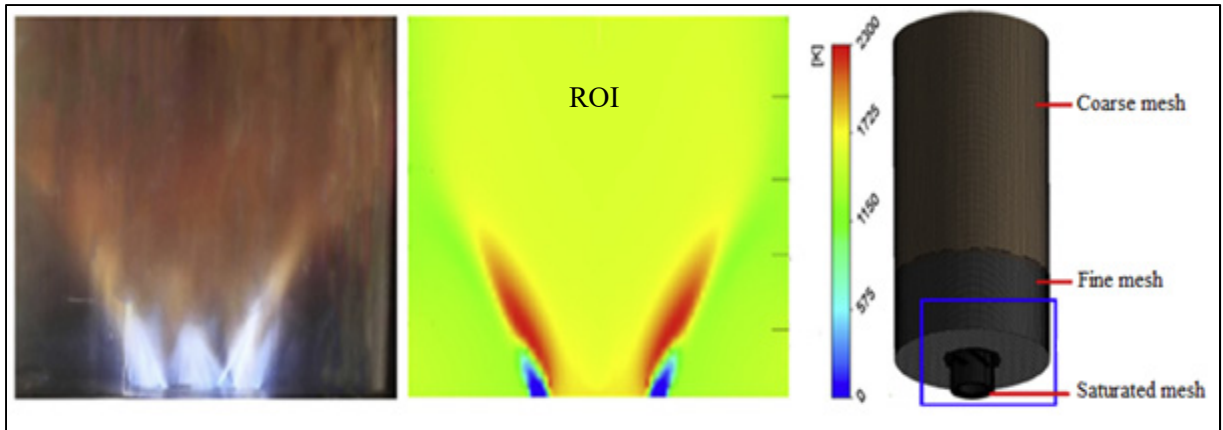


Figure 1.4 Sample of results showing the visible flame vs. numerical one (in terms of temperature) and meshing concept
Taken from Samiran *et al.* (2019)

1.4 Literature review conclusions

Regarding the studied combustion environments, Table 1.1 summarizes the combination of parameters that have been studied in the literature, where combustion took place under ambient pressure and temperature. The swirler diameter (d_{sw}) and inlet bulk velocity (V_{in}) are used as the characteristic length scale and characteristic velocity, respectively, for the inlet Reynolds number (Re_{in}) calculation. HVR represents the hydrogen volumetric ratio or hydrogen concentration in the fuel blend (molar basis), while ϕ represents the global equivalence ratio. α indicates the swirl vanes angle and S is the resulting swirl number/intensity.

First, the survey shows that, when data is available, the considered turbulence conditions, represented in terms of V_{in} (Re_{in} inside the swirler) or u' (u'/S_L) at the combustion chamber entry where the flame exist, are below expected levels in industrial gas turbines, used for power generation purposes, where the velocity fluctuations are usually higher than the laminar flame speed (Zimont, 2000). The resulting flame of such a condition is then called the Intermediate Steady Propagation (ISP) flame that could be characterized by a practically constant flame speed, controlled by turbulence, chemistry, and the molecular process (Zimont, 2000). For instance, the V_{in} , Re_{in} , and u' considered herein are 30 m/s, 36000, and

10 m/s, respectively, while the maximum laminar flame speed ($S_{L_{max}}$) could reach 40 cm/s, for the methane-air stoichiometric combustion at atmospheric pressure and temperature. Thus, u'/S_L ratio could have a minimum value of 25 (for the stoichiometric combustion) and a maximum of 45, for a lean combustion ($\phi = 0.65$). The sole study (Shy *et al.* (2008)) that reached this level was for a cruciform burner, i.e. non-swirling configuration. Second, it can be seen that the literature either considers different HVRs for a unique swirl condition or considers different swirl conditions for a single HVR (or low HVR, up to 9%). In other words and from the author's knowledge, the literature doesn't seem to combine high HVRs and swirl intensities in a lab-scale burner. Third, the literature studies HEC under either lean ($\phi = 0.7$) or stoichiometric burning conditions. The two studies that considered a range of equivalence ratios were either for a non-swirling configuration or for a single swirl condition and low HVR.

In order to help in the understanding of HEC approach and its application inside industrial combustion configurations, this dissertation covers the following combustion environments, high turbulence level ($Re_{in} = 36,000$ and u'/S_L up to 45), a wide hydrogen range (HVR up to 90%), and a wide swirl intensity range (S up to 1.3), under lean and stoichiometric burning conditions.

It can be also seen that radiation was neglected by De *et al.* (2012); Samiran *et al.* (2019); Guo *et al.* (2020), while it was considered by Hawkes *et al.* (2004); Ali *et al.* (2020); Ilbas *et al.* (2016). Therefore, adiabatic and non-adiabatic (i.e. with radiation) simulations are run herein in order to identify the effect of radiation on temperature and emissions.

It can be also concluded that using a detailed chemistry is essential for reproducing the swirl-stabilized ISP flame, analyzing the combustion characteristics, and predicting emissions. Accordingly, the detailed methane-air mechanism GRI 3.0 is used herein to define the chemistry, similarly to Samiran *et al.* (2019), where it (GRI 3.0 mechanism) was reported sufficient for computing either CH_4 -air or high H_2 - CH_4 combustion as well as the formation of pollutants (Samiran *et al.*).

Table 1.1 Summary of HVR, swirl number, ϕ , and turbulence level studied in the literature

Author (year)	HVR %	Swirl cnd. $\alpha - S$	ϕ	$V_{in} - u'$ (m/s) Re_{in}
Schefer <i>et al.</i> (2002)	0, 12, 22, 29	45° - 0.82	Not Reported, NR	8 - 4 20,000
Schefer (2003)	0, 10, 20	45° - 0.76	[0.5 - 2]	12 - NR 14,400
Hawkes & Chen (2004)	0, 29	45° - 0.82	0.52	15 - 1.5 1,500
Shy <i>et al.</i> (2008)	[0 - 30: 10]	Cruciform burner	0.6, 0.7, 0.8	u'/S_L up to 40
Kim <i>et al.</i> (2009)	0, 4, 9	30°, 45°, 60°	0.7	8 - NR d_{sw} NR
De & Achary (2012)	30	45° - 0.38, 0.82, 1.76	0.7	5.7 / 0.5 13,339
Imteyaz <i>et al.</i> (2018)	[0 - 50: 10]	55° - 0.98	1	4.4, 5.2, 6 - NR 9,000 - 9,500
Nemitallah <i>et al.</i> (2019)	[0 - 50: 10]	55° - 0.98	1	5.2 9,500
Ali <i>et al.</i> (2020)	[20 - 60: 20]	55° - 0.98	1	5.2 9,500
Guo <i>et al.</i> (2020)	[0 - 80: 40]	45° - 0.7	0.7	9.2 - 2.5 21,000

1.5 Research objectives

Considering the fact that dispensing fossil fuels is essential as well as that greenhouse gas emissions must be decreased, it appears that hydrogen-enriched combustion is a promising approach to help with the transition to a carbon-free fuel and a clean combustion. The main objective of this research is to numerically investigate the effects of hydrogen addition and swirl intensity on the combustion process under GTE relevant conditions (for power generation gas turbines).

To achieve this main objective (A0), three sub-objectives, denoted A1, A2, and A3, respectively, are defined as follows:

1. A1: Propose and validate a CFD numerical model for an LP combustor (swirler and combustion chamber) based on experimental data from the literature.
2. A2: Characterize the effect of hydrogen addition on the flame structure and emissions under lean and stoichiometric burning conditions.
3. A3: Identify the effect of swirl intensity on the main flame characteristics and emissions, in combination with specific hydrogen addition and equivalence ratios.

CHAPTER 2

COMBUSTOR CFD NUMERICAL MODEL

The literature review has shown that CFD simulations have been used successfully to study HEC inside industrial combustors. This approach involves/integrates fluid dynamics (aerodynamics), thermodynamics, chemistry (chemical kinetics), and heat transfer. Hence, the CFD numerical modelling effort linked to the present first research sub-objective (A1) will now be presented.

2.1 Introduction

In this chapter, the numerical model's mathematical equations are presented as the model progresses from cold flow to non-reactive and reactive flows, respectively. Then, the CFD model structure, including the turbulence, combustion, and radiation models, model geometry and mesh, boundary conditions and discretization technique, and processing resources are presented.

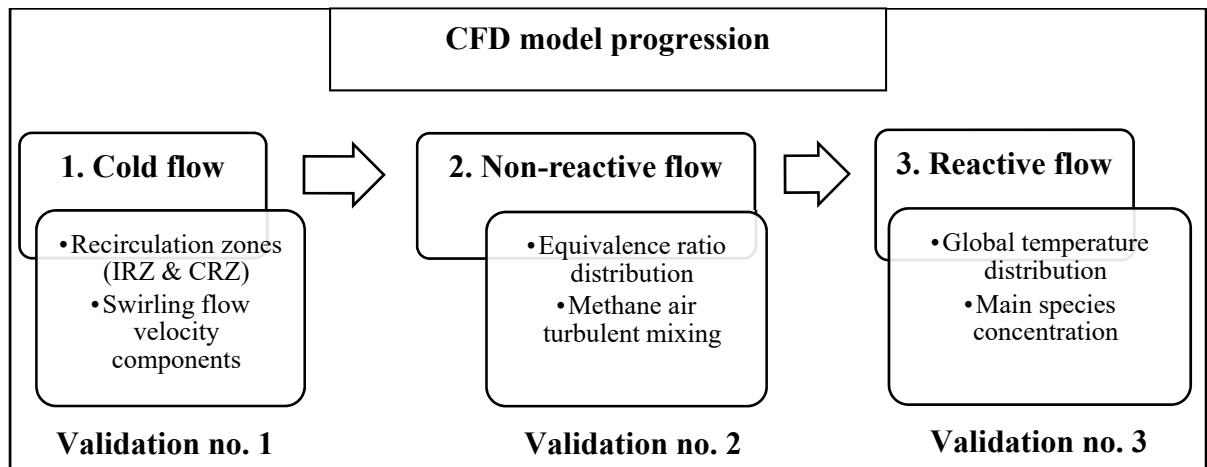


Figure 2.1 CFD model progression map

Figure 2.1 shows the combustor's CFD model map in which the combustor's numerical CFD model is expanded into three modelling steps:

1. Modelling the cold flow which allows to identify the Region of Interest (ROI), global flow field, and recirculation zones.
2. Modelling the non-reactive which emphasizes the methane-air mixing (without reactions) in order to assess the methane-air turbulent mixing and equivalence ratio distribution inside the ROI.
3. Modelling the reactive flow in order to reproduce the flame and predict the global temperature distribution and the main species concentrations.

For each step, a specific validation versus experimental data from the literature is realized and will be presented in Chapter 3.

2.2 CFD model structure

Figure 2.2 present an overview of the CFD model. The map shows how the combustor CFD numerical model defines the turbulent premixed combustion process in terms of two key factors, namely, turbulence and chemistry, in the left and right dashed boxes, respectively. It also shows a sub-model to account for radiation heat loss.

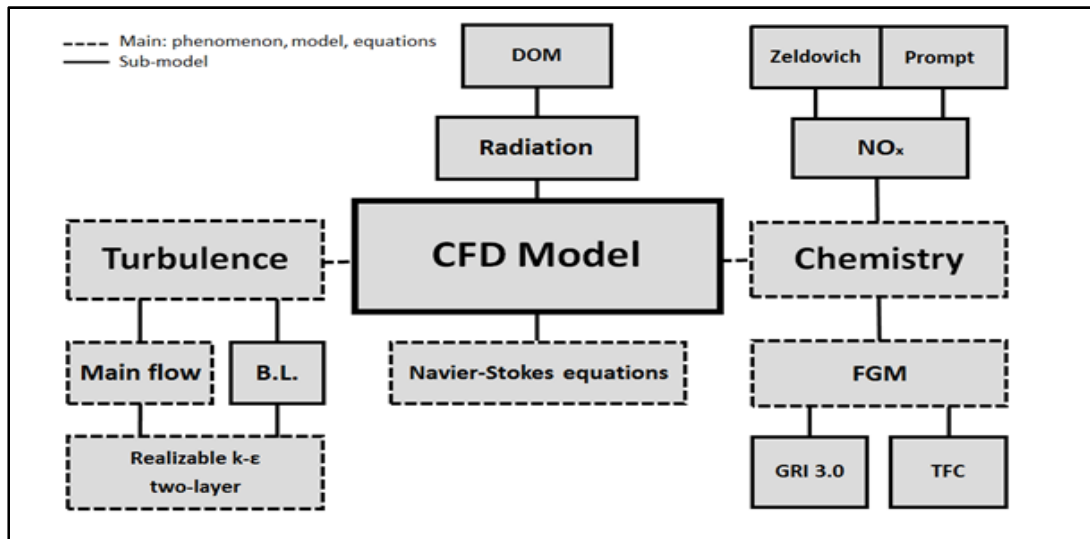


Figure 2.2 CFD basic equations, main models, and sub-models map

2.3 Governing equations

In this section, the CFD model's governing equations are presented with respect to the numerical model steps, i.e. cold flow, non-reactive flow, and reactive flow, respectively.

2.3.1 Cold flow model

Starting with the cold flow model, 3D steady simulations are conducted in order to identify the global flow field. The Simcenter STAR-CCM+ commercial code (version 2020.1) is used to perform all simulations. Air is considered as an incompressible fluid, based on an inlet bulk velocity of 30 m/s, as in Taupin, Benoît PhD Thesis in French (2003). More details about the experimental conditions will be presented in Chapter 3. The corresponding Mach number (M) for this velocity is ≈ 0.08 indicating that the flow could be considered as an incompressible flow ($M < 0.2$), considering an ambient air temperature of 300 K. Consequently, the segregated flow model in STAR-CCM+ is employed to solve flow equations implying that the conservation equations of mass and momentum are solved together in a sequential manner, while the conservation equation of energy is solved via an additional segregated energy model in order to reduce the CPU time (Siemens Digital Industries Software, 2020). More details about the solution techniques will be presented in section (2.8).

The conservation equations of mass, momentum (x , y , and z directions), and energy are solved for the mean flow field, equations (2.1), (2.2), and (2.3), respectively. Air is considered as a Newtonian fluid and hence the Reynolds stress vector/tensor is used for the closure of the above equations, considering the Boussinesq approximation, as per equation (2.4). All the details of the turbulence model used will be discussed in the ensuing subsection, 2.3.1.1.

Air is considered as an ideal gas and hence the equation of state is used to determine its density, equation (2.5). The dynamic viscosity (μ) is set to a constant value of $1.716.E^{-5}$ Pa.s.

$$\bar{\nabla} \cdot (\rho \bar{\mathbf{V}}) = 0 \quad \text{where: } \bar{\mathbf{V}} = u\hat{i} + v\hat{j} + w\hat{k} \quad (2.1)$$

$$\frac{D(\rho \bar{\mathbf{V}})}{Dt} = \bar{\nabla} \cdot (\rho \bar{\mathbf{V}} \times \bar{\mathbf{V}}) = \bar{\nabla} \cdot \sigma + F_b \quad \text{where: } \sigma = -PI + T \quad (2.2)$$

$$\bar{\nabla} \cdot (\rho E \bar{\mathbf{V}}) = F_b \cdot \bar{\mathbf{V}} + \bar{\nabla} \cdot (\bar{\mathbf{V}} \cdot \sigma) - \bar{\nabla} \cdot \mathbf{q} + S_E \quad (2.3)$$

$$T = 2\mu_t D - \frac{2}{3}\mu_t (\bar{\nabla} \cdot \bar{\mathbf{V}}) \mathbf{I} \quad (2.4)$$

$$\rho = P/RT \quad (2.5)$$

where $\rho, \bar{\mathbf{V}}, t, \sigma, P, \mathbf{I}, T, F_b, E, \mathbf{q}, S_E, D, R$, and T represent the density, velocity vector, time, stress tensor, pressure, identity tensor, viscous stress tensor, body force per unit mass, total energy per unit mass, heat flux, energy source per unit volume, strain tensor, universal gas constant and temperature, respectively.

2.3.1.1 Turbulence model

The Reynolds Averaged Navier-Stokes (RANS) approach is a time-averaged equation of fluid flow motion, which is primarily used to describe turbulent flow. For the derivation of RANS equations from the instantaneous Navier Stokes equations, a Reynolds decomposition is used, where an instantaneous property (for instance velocity, v) is decomposed into its time-averaged (\bar{v}) and fluctuating quantities (ψ), as shown in equation (2.6). In order to close the RANS equations, a two-equation turbulence model (realizable k- ϵ) is used. The realizable k- ϵ turbulence model is an eddy viscosity turbulence model (μ_t) that allows to derive the turbulent viscosity (μ_t), through equation (2.7), and hence the Reynolds stress vector/tensor could be expressed as a function of the mean flow velocity, using the Boussinesq approximation, equation (2.4). Therefore, two additional equations are solved for the turbulent kinetic energy (k) and the turbulent kinetic energy dissipation rate (ϵ), equations (2.8) and (2.9), respectively. All model coefficients values are found in STARCCM + theory manual.

$$v = \bar{v} + \hat{v} \quad (2.6)$$

$$\mu_t = \rho c_\mu f_\mu \frac{k^2}{\varepsilon} \quad \text{where: } c_\mu = 0.09 \text{ \& } f_\mu = 1 \quad (2.7)$$

$$\bar{\nabla} \cdot (\rho k \bar{V}) = \bar{\nabla} \cdot \left[\left(\mu + \frac{\mu_t}{\sigma_k} \right) \nabla k \right] + P_k - \rho(\varepsilon - \varepsilon_o) \quad (2.8)$$

$$\bar{\nabla} \cdot (\rho \varepsilon \bar{V}) = \bar{\nabla} \cdot \left[\left(\mu + \frac{\mu_t}{\sigma_\varepsilon} \right) \nabla \varepsilon \right] + \frac{1}{T_e} C_{\varepsilon 1} P_\varepsilon - C_{\varepsilon 2} f_2 P_\varepsilon \left(\frac{\varepsilon}{T_e} - \frac{\varepsilon_o}{T_o} \right) \quad (2.9)$$

where μ and μ_t are the dynamic and turbulent eddy viscosity, σ_k , σ_ε , $C_{\varepsilon 1}$, $C_{\varepsilon 2}$, are the model coefficients, P_k and P_ε are production terms, f_2 is a damping coefficient, ε_o and T_o are the ambient dissipation rate and temperature, and T_e is the effective temperature.

The main impetus of using the realizable k- ε turbulence model is its capability to model high-turbulent swirling flow versus the other two-equation turbulence models, according to Abe, Kondoh, & Nagano (1994). Moreover, it is frequently used in the literature to model the swirling flow in burners, as pursued herein by Novosselov, Malte, Yuan, Srinivasan, & Lee (2006); Novosselov & Malte (2008); Fichet, Kanniche, Plion, & Gicquel (2010); İlbaş *et al.* (2016); Samiran *et al.* (2019), to name a few.

The near-wall flow is solved using a two-layer Y^+ sub-model, emanating from the realizable k- ε turbulence model in STAR-CCM+, in order to capture the boundary layer phenomenon (viscous sub-layer, buffer layer, and log-law layer), where Y^+ is a scalar representing the non-dimensional wall distance and can be defined according to equation (2.10). In the two-layer realizable k- ε turbulence model, the turbulent kinetic energy (k) transport equation is solved across the entire flow - as indicated earlier in equation (2.6) - while the turbulent kinetic energy dissipation rate (ε) is prescribed at the near-wall layer as a function of the wall-distance, d , according to equation (2.11), where I_ε is a length scale function computed at the layer far from the wall according to equation (2.7). A wall-proximity indicator (λ) - defined according to equation (2.12) - is used to blend the turbulent viscosity calculated from the realizable k- ε turbulence model, equation (2.9), with the two-layer values, equation

(2.13), as per equation (2.14). All equations, model constants, and coefficients are available in the STAR-CCM+ theory manual.

$$Y^+ = \frac{u^* y}{\nu} \quad (2.10)$$

$$\varepsilon = \frac{k^{1.5}}{l_\varepsilon} \quad (2.11)$$

$$\lambda = \frac{1}{2} \left[1 + \tanh \left(\frac{Re_d - 60}{A} \right) \right] \quad \text{where: } A = \frac{10}{a \tanh 0.98} \quad (2.12)$$

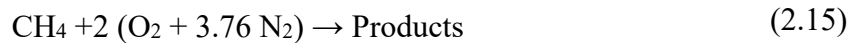
$$\left(\frac{\mu_t}{\mu} \right)_{\text{two-layer}} = 0.42 Re_d c_\mu^{0.25} \left[1 - e^{-\frac{Re_d}{70}} \right] \quad (2.13)$$

$$\mu_t = \lambda \mu_t|_{\text{equation (2.9)}} + (1 - \lambda) \mu \left(\frac{\mu_t}{\mu} \right)_{\text{two-layer}} \quad (2.14)$$

where y , u^* , and ν are the normal distance from the wall to the closest cell centroid, reference velocity, and kinematic viscosity, respectively.

2.3.2 Non-reactive flow model

Next, the conservation of species is added to the cold flow model equations such as to reproduce the non-reactive flow model. Air is considered as a mixture of 21% oxygen (O_2) and 79% nitrogen (N_2), ratio by volume. Methane (CH_4) is added to the multi-component gas sub-model to represent the fuel. Now, three species are considered for the non-reactive flow and thus three conservation equations (one per species) are added to the cold flow models, from equation (2.1) to equation (2.14). Equation (2.15) shows the stoichiometric methane-air non-reactive flow equation, while equation (2.16) shows the conservation equation of a species (i), where i denotes either O_2 , N_2 , or CH_4 , Y is the mass fraction, J is the laminar (or molecular) diffusive flux, and Sc_t is the turbulent Schmidt number, physically defined as the ratio of the viscous diffusivity to the mass diffusivity, considering the turbulent velocity.



$$\bar{\nabla} \cdot (\rho Y_i \bar{V}) = \bar{\nabla} \cdot \left(J_i + \frac{\mu_t}{Sc_t} \nabla Y_i \right) \quad (2.16)$$

2.3.3 Reactive flow mode

Regarding the reactive flow modelling, two modelling categories are available in the CFD commercial code (STAR-CCM+) used, either the flamelet model or the reacting species transport model. Since the two categories are used in the literature to model combustion, both modelling approaches were evaluated and it was found that the flamelet approach better reproduced the experimental flame of Taupin (2003), in terms of the formation of recirculation zone, the prediction of swirling flow velocity components, the visible flame shape, the distribution of the burnt temperature inside the ROI, and the prediction of AFT and NO_x level. Therefore, the governing equations pertaining to the flamelet approach are presented herein, while other details will be discussed in section (2.4).

2.3.3.1 Flamelet model

In the flamelet approach, also known as the Flamelet Generated Manifold (FGM), combustion products are assumed to be directly formed from the reactants based on pre-tabulated data/tables. These tables are generated using a detailed kinetic mechanism associated with a 0D constant pressure reactor, considering both fuel and oxidizer being in a gaseous state. Later, a specific interpolation is adopted to interpolate the 0D constant pressure reactor to a 3D turbulent one, based on a reduced set of variables, such as the mixture fraction (f), progress variable (c), and enthalpy (h). In recent years, the FGM has been favoured over the other combustion models as it avoids the computational cost seen with complex chemistry calculations. The FGM approach has been frequently reported to successfully model the turbulent combustion process inside various industrial combustors, Kuenne, Ketelheun, & Janicka (2011); Goldin, Montanari, & Patil (2014); Palanti, Pampaloni, Andreini, & Facchini (2018); Samiran *et al.* (2019), to name a few.

Once the FGM is selected to model the turbulent premixed combustion process, the three conservation equations of species (O₂, N₂, and CH₄), indicated in section 2.3.2, are disabled. Instead, the detailed methane-air reaction mechanism (GRI Mech. 3.0) involving 325 reactions and 53 species is used to define the chemistry of the laminar flamelet gas-phase

combustion, i.e. to generate the FGM table. The GRI mechanism includes the chemical kinetics, species thermal data, and species transport data. In FGM, the thermo-chemistry state is parametrized by three parameters, namely, the mixture fraction (f), the progress variable (c), and the heat loss ratio (γ). Each of these parameters will be explained below.

The first parameter used for the thermo-chemistry state in FGM modelling is the mixture fraction (f), which represents the fuel mass fraction in the fresh mixture, as defined in equation (2.17). Therefore, f varies between 1 - for pure fuel - and 0 for pure oxidizer. A transport equation is solved for f , as shown per equation (2.18). In this equation, f is a conserved scalar. The turbulent Schmidt number (Sc_t) is set to 0.9 for all simulations, in order to keep the unity Prandtl and Lewis numbers assumption, representing the ratio of viscous diffusivity to thermal diffusivity and thermal diffusivity to mass diffusivity, respectively. In addition to the mixture fraction transport equation, another transport equation - equation (2.20) - is solved for the mixture fraction variance (f_{var}), defined in equation (2.19), in order to account for the turbulent fluctuations of the mixture fraction.

$$f = \frac{m_f}{m_f + m_{ox}} \quad (2.17)$$

$$\bar{\nabla} \cdot [\rho \bar{\nabla} - (\rho D_f + \frac{\mu_t}{Sc_t}) \nabla f] = 0 \quad (2.18)$$

$$f_{var} = \overline{(f - \bar{f})^2} \quad (2.19)$$

$$\bar{\nabla} \cdot [\rho f_{var} \bar{\nabla} - \frac{\mu_t}{Sc_t} \nabla f_{var}] = 2 \frac{\mu_t}{Sc_t} (\nabla f)^2 - \rho c_d \frac{\varepsilon}{k} f_{var} \quad (2.20)$$

where m_f , m_{ox} , and D_f are the fuel and oxidizer mass flow rates, the laminar or molecular diffusivity, respectively.

The second parameter representing the thermo-chemistry state in the FGM modelling is the progress variable (c), which is defined as a scalar quantity that distinguishes the mixture status, as either unburnt ($c = 0$), burnt ($c = 1$), or something in-between ($0 < c < 1$). Equation

(2.21) defines c , while equation (2.22) is used to calculate y , defined shortly. For the methane-air combustion, all species weights are set to zero, except CO_2 and CO , i.e. $W_{\text{CO}} = W_{\text{CO}_2} = 1$, which indicates a hydrocarbon combustion. On the other hand, for HEC in Chapter 4, $W_{\text{CO}} = W_{\text{CO}_2} = W_{\text{H}_2\text{O}} = 1$, indicating the combustion of a hydrogen-hydrocarbon blend.

$$c = \frac{y - y_u}{y_b - y_u} \quad (2.21)$$

$$y = \sum_{i=1}^{\text{species}} (W_i Y_i) \quad (2.22)$$

where y represents the unnormalized progress variable of the mixture and subscripts u and b denotes the initial unburnt state and equilibrium burnt state, respectively, Y_i is a specie mass fraction, and W_i is a specie weight.

An additional transport equation is solved for the progress variable (equation (2.23)), in which the source term ($\dot{\omega}_c$) represents the fuel consumption that closes the progress variable transport equation (Zimont, 2000). A flame position model is used to calculate the turbulent premixed flame movement in space and hence close the progress variable transport equation, hereinafter known as the Turbulent Flame speed Closure (TFC). Equation (2.24) defines how such a closure occurs. An algebraic expression, namely the Zimont correlation, is used to calculate S_t and hence account for the turbulence chemistry interaction, as per equation (2.25). α_u is the thermal diffusivity of the unburnt mixture, which is calculated based on the laminar flame thickness (δ_L) and laminar flame speed (S_L), as per equation (2.26). Hence, the laminar flame speed is defined in advance according to the Gülder definition that accounts for the fuel type and equivalence ratio, Gülder (1991), as per equation (2.27). All model parameters, definitions, and coefficients are found in the STARCCM + theory manual.

$$\bar{\nabla} \cdot (\rho c \bar{\nabla}) - \bar{\nabla} \cdot (\Gamma_c \nabla c) = \dot{\omega}_c \quad (2.23)$$

$$\dot{\omega}_c|_{\text{TFC}} = \rho_u S_t |\nabla c| \quad (2.24)$$

$$S_t = \frac{1}{2} G (u')^{3/4} S_L^{1/2} \left(\frac{l_o}{\alpha_u} \right)^{1/4} \quad (2.25)$$

$$\delta_L = \frac{\alpha_u}{S_L} \quad (2.26)$$

$$S_L = 0.422 \varphi^{0.15} e^{-5.18(\varphi - 1.075)^2} \quad (2.27)$$

where ρ_u is the unburnt mixture density, S_t is the turbulent flame speed, G is the stretch factor, u' is the axial velocity fluctuation, S_L is the laminar flame speed, and l_o is the turbulent characteristic length.

In addition to the progress variable transport equation, an algebraic relationship is used to calculate the unnormalized progress variable variance (y_{var}) in order to account for the turbulent fluctuations of the progress variable, as per equation (2.28).

$$y_{var} = c_v \Delta^2 (\nabla y)^2 \quad (2.28)$$

where c_v and Δ are a model constant and the mesh size, respectively. The mesh size is calculated in a 3D domain by averaging the alternative cell size in the x, y, and z directions (separately) relative to the trimmed mesher coordinate system, according to STAR-CCM + theory manual.

The third and last parameter representing the thermo-chemistry state in the FGM modelling is the Heat Release Ratio, HRR (γ). This ratio indicates the amount of heat gain, when non-adiabatic simulations are conducted. Since heat transfer by radiation is considered in this dissertation, the HRR is used herein to represent the deviation of the system from its adiabatic state. Equation (2.29) shows the definition of the heat loss (release) ratio. The last two enthalpies (h_{ad} and h_{sens}) are calculated according to equations (2.30) and (2.31), respectively.

$$\gamma = \frac{h_{ad} - h_{cell}}{h_{sens}} \quad (2.29)$$

$$h_{ad} = (1 - f) h_{ox} + f h_f \quad (2.30)$$

$$h_{sens} = \sum_{i=1}^{species} Y_i \int_{200K}^T c_{p_i} dT \quad (2.31)$$

where h_{cell} , h_{ad} , and h_{sens} represent the cell, adiabatic, and sensible enthalpies, respectively, and c_{p_i} is a specie specific heat at a constant pressure.

2.3.3.2 NO_x sub-model

A sub-model for predicting NO_x is included in the reactive flow model. Therefore, an additional transport equation is solved for the NO_x mass fraction, Y_{NO_x} , as per equation (2.32), in which the two right hand source terms represent the thermal and prompt NO_x, respectively.

$$\bar{\nabla} \cdot [\rho Y_{NO_x} \bar{V} - (\rho D_f + \frac{\mu_t}{\sigma_t}) \nabla Y_{NO_x}] = \dot{\omega}_{NO_{xthermal}} + \dot{\omega}_{NO_{xprompt}} \quad (2.32)$$

The prompt NO_x is formed from the reaction of nitrogen molecule with hydrocarbons radicals in fast kinetics, which involves complex reactions with many intermediate species such as CH, CH₂, HCN, CN, and others. This complex kinetic is simplified to a one-step reaction derived by Soete (1975). The prompt NO_x source term ($\dot{\omega}_{NO_{xprompt}}$) is calculated according to equation (2.33). The latter is defined according to equation (2.34).

$$\dot{\omega}_{NO_{xprompt}} = k_r M_{wNO_x} \quad (2.33)$$

$$k_r = 6.4 f e^{6 \left(\frac{R_u T}{P} \right)^{a+1}} [O_2]^a [N_2] [Fuel] e^{-\left(\frac{E_A}{R_u T} \right)} \quad (2.34)$$

where M_{wNO_x} and k_r are the NO_x molecular weight and rate constant, respectively, terms in brackets represent the species (O_2 , N_2 , and CH_4) molar concentration and f is a correction factor.

Thermal NO_x is formed at high temperature ($T > 1800$ K) from the dissociation of nitrogen and oxygen. The thermal NO_x chemistry is known as the Zeldovich mechanism, equations (2.35) and (2.36). An additional reversible reaction between N and OH-radical - equation (2.37) - is considered in STAR-CCM+ and known as the Extended Zeldovich mechanism, based on kinetics data from Baulch, Drysdale, Horne, & Lloyd (1973).



The NHH pathway is considered herein and is taken into account in the GRI 3.0 mechanism.

2.3.3.3 Radiation sub-model

Heat transferred by radiation is considered herein, including the emissivity of the combustion by-products, CO_2 and H_2O . In addition, a fixed temperature of 1300 K is set to the combustion walls, similar to Monaghan *et al.* (2014). An additional transport equation is solved for radiation, equation (2.38), namely the Radiative Transport Equation (RTE).

$$\frac{dI_\lambda}{ds} = -\beta_\lambda I_\lambda + k_{a\lambda} I_{b\lambda} + \frac{k_{s\lambda}}{4\pi} \int_0^{4\pi} I_\lambda \Omega d\Omega + k_{pa\lambda} I_{pb\lambda} + \frac{k_{ps\lambda}}{4\pi} \int_0^{4\pi} I_\lambda \Omega d\Omega \quad (2.38)$$

where I_λ , $I_{b\lambda}$, and $I_{pb\lambda}$ are the radiative, black body, and particle black body intensities at a specific wave length, λ , respectively, s is the distance, β_λ is an extinction coefficient ($\beta_\lambda = k_{a\lambda} + k_{s\lambda} + k_{pa\lambda} + k_{ps\lambda}$), $k_{a\lambda}$, $k_{s\lambda}$, $k_{pa\lambda}$, and $k_{ps\lambda}$ are the absorption, scattering, particle absorption, and particle scattering coefficients at a specific wave length, respectively, and Ω

is a solid angle as a part of a hemisphere, where the radiation solution is discretized in the CFD domain.

The Discrete Ordinates Model (DOM) is selected as a radiative transfer model, where the emissivity of combustion products (CO_2 and H_2O) is taken into account. The model considers the Gray Thermal spectrum for modelling wavelength-independent radiation properties, where the full thermal wavelength domain is considered as a whole and all radiative properties are considered invariant within this single spectrum. The media is assumed able to absorb, emit, and scatter radiation. The Weighted Sum of Gray Gases Model (WSGGM) is combined with DOM to describe the combustion products (CO_2 and H_2O) emissivity, similar to Ali *et al.* (2020).

Regarding the coupling of the radiation sub-model with the flow model, the mixture radiant energy is exchanged with flow energy by adding a source term to the conservation of energy equation. Thus, the energy equation source term (S_E) in equation (2.3) takes into account radiation calculated using equation (2.40). The radiant heat flux in a particular direction (q_r) is calculated by integrating the radiant intensity, $I_{\lambda(s)}$, over all solid angles, as presented by equation (2.39).

$$q_r = \int_0^\infty \int_0^{4\pi} I_{\lambda(s)} s \, d\Omega \, d\lambda \quad (2.39)$$

$$\bar{\nabla} \cdot q_r = \int_0^\infty k_{a\lambda} [4\pi I_b - \int_0^{4\pi} I_\lambda \, d\Omega] \, d\lambda \quad (2.40)$$

Overall, the reactive flow model takes into account the conservation equations of mass, momentum, and energy in combination with the k-epsilon turbulence model and the FGM-TFC technique, for modelling combustion.

2.4 Boundary conditions

In this section, the fluid, thermal, and turbulence conditions at the different combustor boundaries are defined.

The velocity inlet conditions are an air inlet bulk velocity (V_{in}) set to 30 m/s (corresponding to a mass flow rate of 8 g/s) for all simulations with an inlet turbulent intensity (I) of 30%, as previously used by Taupin (2003); Taupin, Cabot, Martins, Vauchelles, & Boukhalfa (2007) for all their experiments. The air inlet temperature is set to 300 K and pressure is 1 atm. The fuel mass flow rate is adjusted as a function of the equivalence ratio, but the turbulent intensity is set to 10%. As an example, the fuel mass flow rate is set to 0.303 g/s of methane at an equivalence ratio of 0.65 while other values are presented in Table 2.5. The outlet boundary condition is set to pressure-outlet with a turbulent intensity of 5%. The integral length scale (l_0) is set to 0.018 m, corresponding to the characteristic length of the swirler diameter.

Fuel is considered as pure methane (CH_4) in a gaseous state for all simulations. Fuel is ejected radially through eight holes located 30 mm before the combustion chamber inlet.

Table 2.1 Fuel mass flow rate variation vs. equivalence ratio in CFD, base case in **bold**

Model	Non-reactive flow model				Reactive flow model		
φ	0.6	0.63	0.65	0.68	0.7	0.85	1
\dot{m}_f (g/s)	0.28	0.294	0.303	0.317	0.326	0.396	0.466

Ambient conditions of pressure (1 atmosphere) and temperature (300 K) are selected for the unburnt mixture. For the wall, a no-slip condition is assumed for the entire combustor wall with $T_{wall} = 1300$ K. Simulations are run with and without radiation loss. Table 2.2

summarizes the fluid, thermal, and turbulence boundary conditions at an equivalence ratio of 0.65.

Table 2.2 Applied fluid, thermal, and turbulent boundary conditions in CFD ($\phi = 0.65$)

Boundaries	B.C type	Fluid cnds (g/s)	Thermal cnds (K)	Turbulence cnds % , (m/s) , m	
Air inlet	Mass flow inlet	$\dot{m}_{\text{air}} = 8$	$T_{\text{air in}} = 300$ Total temperature	$I_{\text{in}} = 30\%$ $V_{\text{in}} = 30 \text{ m/s}$	$l_0 = 0.018 \text{ m}$
Fuel inlet holes	Mass flow inlet	$\dot{m}_f = 0.303$	$T_{f \text{ in}} = 300$ Total temperature	$I_f = 10\%$	
Outlet	Pressure outlet	$\dot{m}_{\text{target}} =$ $\sum \dot{m}_{\text{air}} + \dot{m}_f =$ 8.303	$T_{\text{out}} = 300$ Static temperature	$I_{\text{out}} = 5\%$	

Lastly, for the radiative boundary conditions, a radiation temperature of 300 and 1300 K is selected for the open boundaries, the inlets (either air or fuel) and outlet, respectively. A fixed temperature of 1300 K is set for the combustion chamber walls, as was also done by Monaghan *et al.* (2012). Figure 2.3 shows a 2D distribution of the radiative emissivity distribution on the different CFD model boundaries.

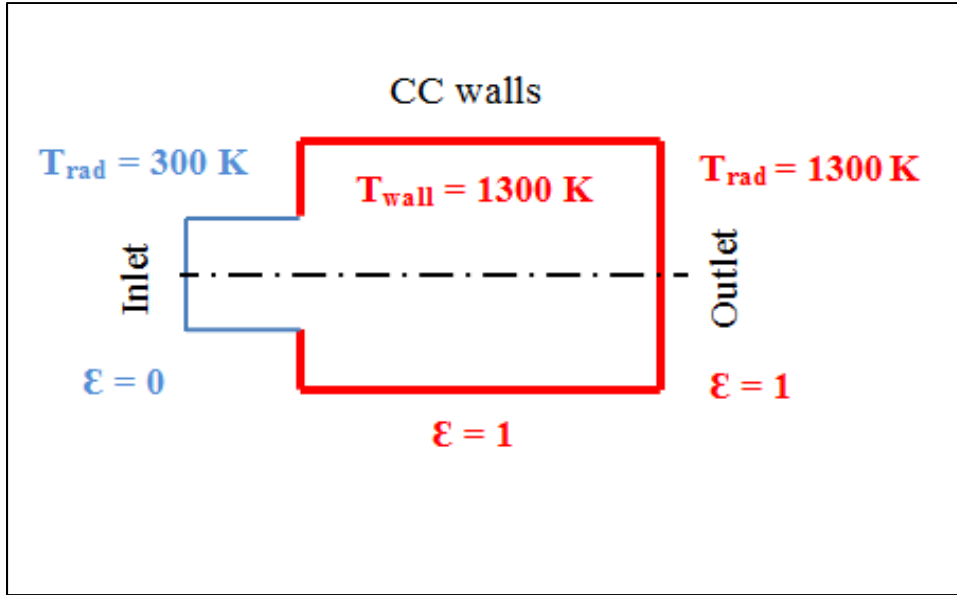


Figure 2.3 2D distribution of radiative emissivity and wall temperature applied to the CFD boundaries

2.5 Discretization, solution, and initialization

The governing equations are solved via an Algebraic Multi Grid linear solver (AMG) applied to the meshed domain. A second order finite volume discretization method is applied for all transport equations.

The volume integral (source term) is calculated as the product of the mean value at cell centroid and cell volume, $(S_{\Phi}V)_o$, i.e. a second order accuracy. For the two surface integrals (convective and diffusive fluxes), a quadrature approximation is employed to express the integral at the cell face center. Since the property is only known at the cell centroid (not the cell face), a Second Order Upwind (SOU) discretization scheme is used for the interpolation. The latter was recommended for the steady RANS-based simulations, according to the STAR-CCM+ theory manual.

Regarding the discretization of the RTE (equation (2.38)), in which the wave-length independent radiant intensity (I_{λ}) is expressed neither in time (t) nor in space (x , y , and z)

coordinates, a solid angle (Ω) measured in steradian as a part of a hemisphere, a level symmetric quadrature, also known as S_n , is used for the RTE discretization in STAR-CCM+. For all radiative simulations, the total volume radiative heat source of the whole CFD domain is verified to be equal to the total radiative heat flux over the radiative boundaries, the CC walls and outlet.

The Under-Relaxation Factors (URFs) of the velocity, energy, k- ϵ turbulence model, FGM, TFC, NO_x, and DOM are uniquely set to 0.8 so as to simultaneously relax the turbulent radiative reactive flow, as recommended by the STAR-CCM+ theory manual. Only the pressure URF is set to 0.3.

All reactive flow simulations are initialized with cold flow conditions, i.e. zero profiles of mixture fraction and its variance, progress variable, and NO_x up to 6000 iterations. After that, a progress variable ignitor ($c = 1$) is used to ignite the mixture. All reactive flow simulations (with radiation) were run for at least 100,000 iterations to ensure reaching a steady-state solution. Moreover, the solution was confirmed to be converged similar to the same criteria of Samiran *et al.* (2019), where the energy, mixture fraction and its variance residuals reach 10^{-3} , the flow and turbulence residuals reach 10^{-5} , the progress variable and NO_x, residuals reach 10^{-8} and 10^{-12} , respectively.

2.6 Model geometry

The model geometry is selected based on the availability of experimental data of a laboratory scale combustor (an atmospheric burner) from Taupin (2003); Taupin *et al.*, (2007) and shown in Figure 2.4 (top). This geometry can be considered as similar to an industrial gas turbine combustor, where fuel is injected radially and mixed with air inside an axial swirler (premixer) with a bluff-body, before entering the combustion chamber (dump plane). The axial swirler is composed of six helical vanes settled at 50° with the longitudinal axis and placed on 8 mm diameter bluff body, as shown in Figure 2.4 (bottom). The swirler outer diameter is 18 mm. The geometrical swirl number resulting from that configuration is 0.9,

according to equation (2.41). The combustion chamber is a Herasil quality transparent quartz tube with an 80 mm diameter and a 200 mm length.

$$S = \frac{2(1-a^3)}{3(1-a^2)} \tan(\alpha) \quad (2.41)$$

where a is the ratio between the bluff body and swirler diameters.

The selected combustor configuration ($\alpha = 50^\circ$ and $S = 0.9$) resulted in a perfect methane-air mixture with a stable flame (Taupin, 2003; Taupin *et al.*, 2007). Therefore, it is considered as the basic swirl configuration herein.

The CFD domain of study is selected to include the axial swirler, in order to capture the fuel-air turbulent mixing, and hence the domain starts from the swirler inlet up to the combustion chamber outlet, as shown in red in Figure 2.4 (top).

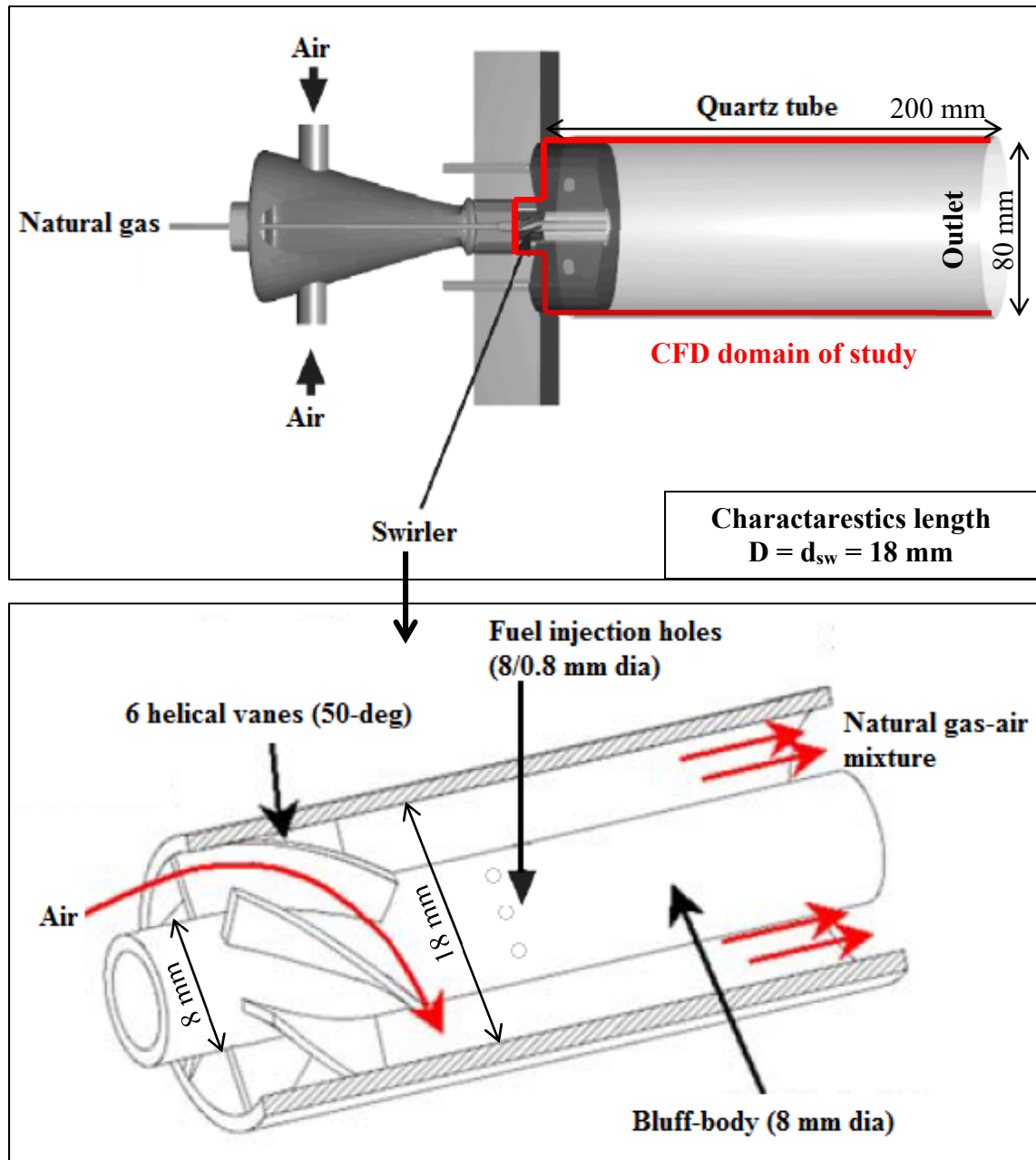


Figure 2.4 Free exhaust atmospheric burner tested by Taupin (2003) (top) and a longitudinal cut-out of the swirler with bluff body (bottom)

2.7 Mesh structure

The geometry presented in Figure 2.4 is meshed using the STAR-CCM+ 3D meshing module. The work in this section is organized as follows: The strategy followed to mesh the combustor model is presented first. Then, the grid independence test is presented, based on a calculation of the Grid Convergence Index (GCI) according to Celik, Ghia, Roache, & Freitas (2008).

2.7.1 Mesh strategy

The 3D mesh is prioritized in this dissertation because according to Taupin (2003), the methane-air mixing profile (not experimentally measured) affects the NO_x emissions level, especially in the wake region just behind the bluff body. The same conclusion was highlighted in the literature by Novosselov *et al.* (2006); Novosselov & Malte (2008), who asserted that considering a uniform fuel-air mixture profile - instead of a radial one - is responsible by itself for underrating the experimental NO_x levels by a factor of three. Moreover, the swirler has been included in the CFD domain in recent numerical studies of different burners, such as in Hawkes & Chen (2004); De & Achary (2012); Samiran *et al.* (2019). Accordingly, the swirler is included in the CFD domain of study herein.

2.7.2 Mesh configuration

The mesh configuration follows the approach of Samiran *et al.* (2019), who used three elements to mesh their studied model, namely, saturated, fine, and coarse mesh for the swirler, region of interest, and burn-out region, respectively. A hexahedral element (named trimmed cell in STAR-CCM+) is used to mesh the entire model, including the swirler. A coarse element size of 8 mm is used for the far stream flow, i.e., near the combustion chamber outlet. This coarse element was considered the mesh base size, and hence all other elements will be reported relative to this size. The minimum surface size is set to be 1% of the base (0.08 mm). The mesh has a smooth transition from the ROI (see Figure 2.5) to the downstream with a surface growth rate of 1.0034. Two prism layers, with a stretch ratio of

1.2 and a thickness ratio of 0.125% of the base element size (0.01 mm) are used to capture the boundary layer phenomenon. A surface refinement with an element size of 1% of the base (0.08 mm) is performed for the fuel inlet holes and its neighbor walls, to capture its exact shape. 100 points per circle are used for meshing all circular surfaces. The swirler surface refinement is performed using an element size of 2.5% of the base (0.2 mm). The swirler minimum surface size is set to be 0.1% of the base size (0.008 mm).

Ultimately, the optimized meshing configuration resulted in \approx a 2 M cells model (1930877), which is comparable to Samiran *et al.* (2019); De & Achary (2012); Monaghan *et al.* (2012). Figure 2.5 shows the entire CFD model meshing configuration, while Figure 2.6 shows some of the meshed swirler surfaces, such as the inlet, helical vanes, fuel inlet holes, and bluff body. Table 2.3 summarizes all the meshing specifications.

Table 2.3 Optimized meshing configuration specifications

	Mesh type	3D mesh
	Element type	Hexahedral (trimmed cell)
	Total number of cells	\approx 2 M cells (1,930,877)
Combustion chamber ($d_{cc} \times L_{cc} =$ 80 x 200 mm)	Base element size (coarse element)	8 mm
	Minimum surface size	1% (0.08 mm)
	Surface growth rate	1.0034
Swirler ($d_{sw} = 18$ mm)	Swirler surface element size	2.5% (0.2 mm)
	Swirler minimum surface size	0.1% (0.008 mm)
Fuel holes ($d_f = 0.8$ mm)	Fuel holes element size	1% (0.08 mm)
	Number of points/circle	100
Boundary layer	Number of prism layers	2
	Prism layers stretch ratio	1.2
	Prism layers thickness ratio	0.125% (0.01 mm)

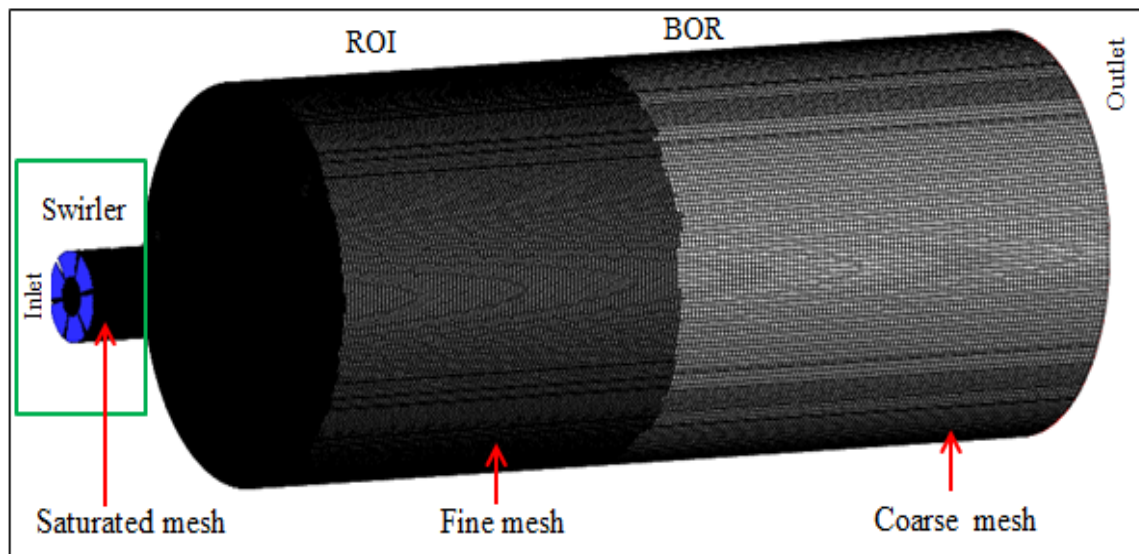


Figure 2.5 Whole CFD model meshing configuration (≈ 2 M cells)

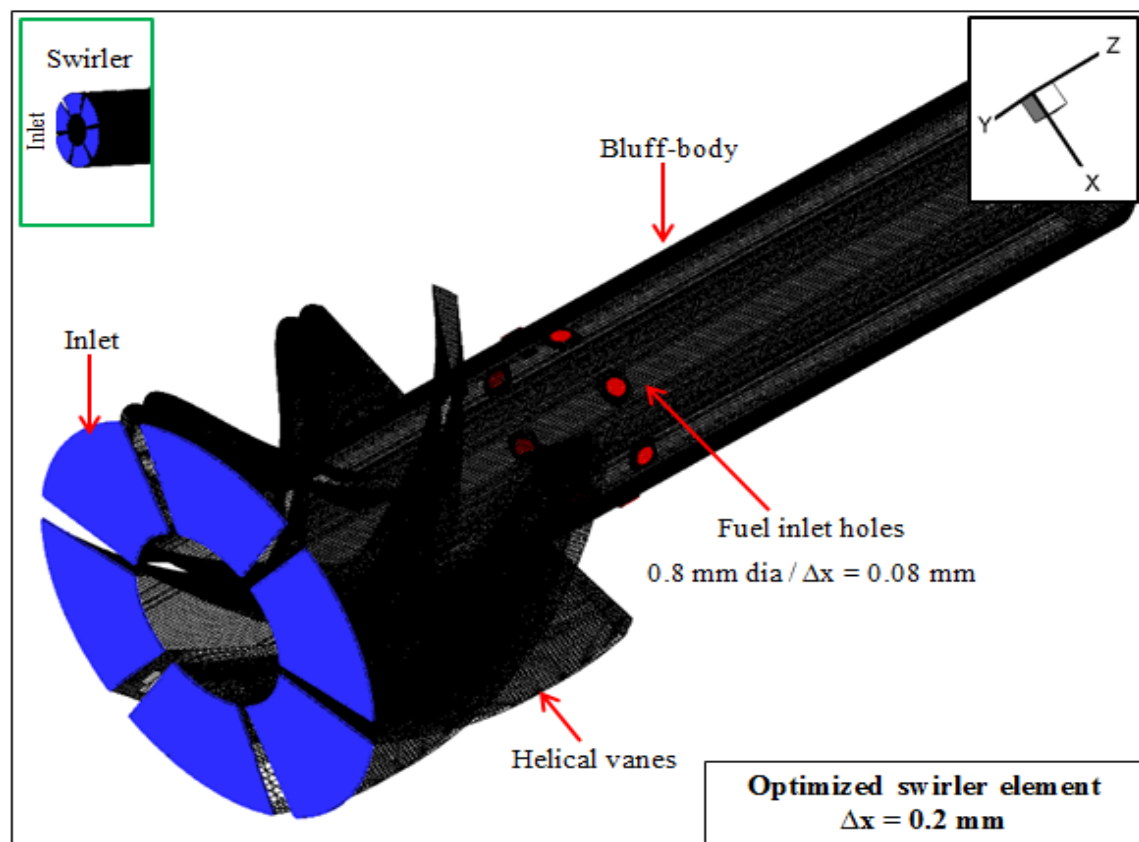


Figure 2.6 Meshed swirler surfaces

2.7.3 Grid independence test (Grid Convergence Index)

In order to assure the solution independency on the mesh, three structured meshes - only differ in the base element size which is the combustion chamber coarse element - are generated and denoted by: 1. Fine, 2. Intermediate and 3. Coarse, according to a method introduced by Celik *et al.* (2008) and is known as the Grid Convergence Index (GCI). The three meshes have a structured/uniform refinement ratio, $h_{\text{coarse}} / h_{\text{fine}} = \text{constant} = 2$, whereas the other mesh parameters are kept the same. This ratio is selected to be greater than the minimum value (1.3), recommended by Celik *et al.* (2008). Table 2.4 summarizes the mesh specifications used, as well as the resulting number of cells for the cold and reactive flow cases size (without radiation and NO_x sub-models) and processing time.

Table 2.4 Meshes used for the Grid Convergence Index (GCI) calculations

Character		1.Fine	2. Intermediate	3. Coarse
CFD domain volume $\pi[(r_{\text{sw}}^2 - r_{\text{bb}}^2) * l_{\text{sw}} + (r_{\text{cc}}^2) * l_{\text{cc}}]$		1.E10 ⁶ mm ³ (1000 cm ³)		
Grid size (mm) (C.C. coarse element)		4	8	16
Refinement ratio (h)		$h_{21} = 2$		$h_{32} = 2$
Number of cells		≈ 4 M	≈ 2 M	(900 K) ≈ 1 M
Cold flow*	Data size	1.7 GB	800 MB	400 MB
	Processing time (hour)	4	2	1
Reactive flow* (without radiation and NO _x)	Data size	4 GB	2 GB	1GB
	Processing time (hour)	8	4	2
* Considering 50,000 iterations and 4 nodes*48 CPU/node = 192 CPU, Cedar cluster				

The predictions obtained with these three meshes are compared in terms of different parameters, namely, the temperature, T , the Turbulent Kinetic Energy, TKE , indicating the velocity fluctuations, and the three velocity components, axial, u , radial, v , and tangential, w , at different points distributed axially and radially/preferentially inside the ROI. Figure 2.7 shows the ROI, including only the points that showed a monotonic convergence, i.e. $0 < R_{GCI} < 1$, where R_{GCI} is defined according to equation (2.42) and X refers to any studied parameter. These points are selected based on the presence of strong gradients of T , TKE , and u , inside the Height of Interest (HOI).

$$R_{GCI} = \frac{x_2 - x_1}{x_3 - x_2} \quad (2.42)$$

The points indicated could be classified into four groups as follows:

1. Group A: includes three points (red dots) located axially at the burner's symmetric axis ($0 \leq Z/D \leq 2$), where u is always negative, indicating a reversed flow, and T is always high, indicating the existence of the flame and the occurrence of reactions.
2. Group B: includes five points (blue dots) located axially at $Z/D = 0.22$ and distributed radially at $0 \leq R/D \leq 1$, where the fuel-air mixture enters the combustion chamber and expands forming the shear layers separating the inner and corner recirculation zones.
3. Group C: includes one point (orange dot) located axially at $Z/D = 0.44$ and radially at $R/D = 0.6$, where the shear layer has a colder temperature, as no reactions occur.
4. Group D: includes one point (green dot) located axially at $Z/D = 3.44$ and radially at $R/D = 1$, where the temperature profile has no more changes approaching the burner's outlet.

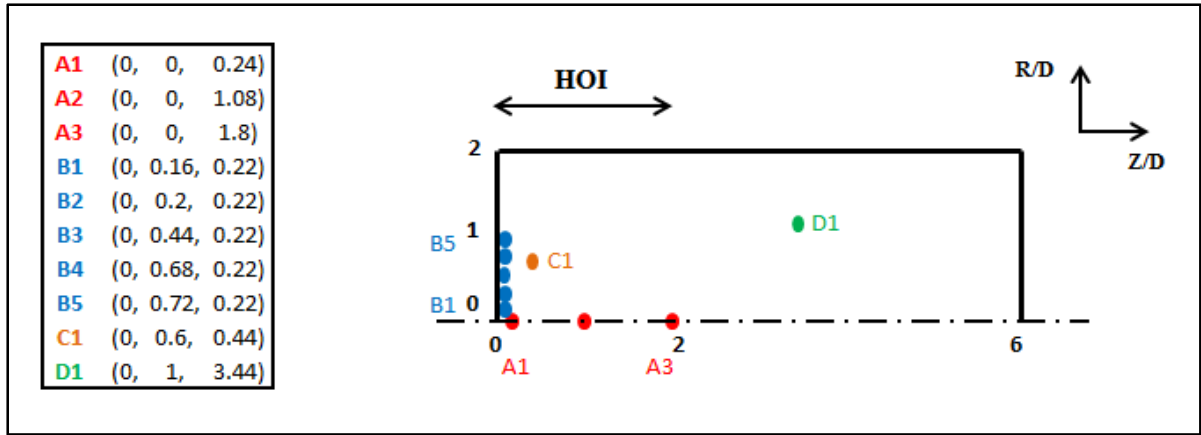


Figure 2.7 Region of Interest (ROI) including the points where the GCI study is conducted

Table 2.5 summarizes the results obtained by the three meshes (T, TKE, u, v, and w) at different point's combinations as well as the R_{GCI} , apparent order of the error due to the used discretization scheme, P_{GCI} , and the resulting GCI error between each two consecutive meshes, the coarse and intermediate, GCI_{32} , as well as the intermediate and fine, GCI_{21} . The equations used for calculating the P_{GCI} , GCI_{32} , and GCI_{21} could be found in Celik *et al.*, (2008).

The apparent order was found to be slightly less than 2, which well matches the discretization scheme used, the Second Order Upwind (SOU) presented earlier in section 2.5, except for two points, A1 and D1, where high temperatures were identified in the CFD field. The averaged apparent order in the CFD domain was found to be 1.58, 1.57, and 1.34 for the temperature, turbulent kinetic energy, and axial velocity, respectively. The average GCI error between the coarse and intermediate meshes was found to be 1.39, 6.59, and 3.78% for the temperature, turbulent kinetic energy, and axial velocity, respectively, while the error between the intermediate and fine meshes is found to be 0.56, 2.45, and 1.75% for the same arrangement of parameters. This indicates that the intermediate mesh compromises both precision and processing time and is thus selected for this dissertation hereinafter.

Table 2.5 GCI results, including the apparent order, P_{GCI} , and errors (GCI_{32} & GCI_{21})

Model	Point	Parameter	1. Fine	2. Inter.	3. Coarse	R _{GCI}	P _{GCI}	GCI ₃₂ %	GCI ₂₁ %
Reactive flow	A1	T (K)	1485.68	1477.43	1441.75	0.23	2.00	0.93	0.21
	B1		1335.68	1321.84	1280.63	0.34	1.57	2.03	0.66
	C1		700.26	710.19	730.26	0.50	1.01	3.37	1.72
	D1		1857.32	1856.39	1851.64	0.19	2.00	0.08	0.02
	B4	TKE (J/kg)	56.86	60.11	72.14	0.27	1.88	7.74	2.52
	B5		94.55	99.49	114.17	0.34	1.57	8.14	3.14
	A2	T (K)	1996.35	1991.16	1978.11	0.39	1.33	0.54	0.21
		u (m/s)	8.57	8.81	9.36	0.44	1.2	5.71	2.64
	A3	TKE (J/kg)	49.21	50.17	52.50	0.41	1.27	3.91	1.69
		u (m/s)	15.27	15.36	15.58	0.39	1.37	1.11	0.44
	B3	u (m/s)	38.74	38.27	37.20	0.44	1.19	2.79	1.18
			30.18	29.97	29.23	0.28	1.86	1.2	0.32
Cold flow	B2	u (m/s)	4.00	4.15	4.46	0.48	1.10	8.08	4.18
		v (m/s)	3.39	3.27	2.98	0.41	1.30	8.69	3.27
		w (m/s)	1.65	1.56	1.34	0.38	1.40	12.88	4.18
Average		T					1.58	1.39	0.56
		TKE					1.57	6.59	2.45
		u					1.34	3.78	1.75

2.8 Processing resources

All simulations were run thanks to the Compute Canada supercomputer (cluster). Two platforms/resources (Graham and Cedar) were used, alternatively. The processing capabilities/specifications of the used resources can easily be accessed at www.computecanada.ca/wiki/resources. The run time differs according to the run model, i.e. cold flow, non-reactive flow or reactive flow and the corresponding activated models and sub-models. For the highest run time model, the pursued combustor CFD model (reactive flow model with NO_x and radiation), an average run time of five hours was enough to reach a converged solution of at least 40,000 iterations utilizing 4 nodes (each having 48 processors), i.e. a total of 192, of any of the two indicated resources.

All simulations were post-processed using Tecplot 360 software (Tecplot 360, 2020) on a TFT-CDF, ÉTS workstation with 32 GB RAM and 12 CPU/2.4 GHz.

2.9 Chapter conclusions

The objective of this chapter was to present the CFD numerical model that will be used as a part of this dissertation. First, the mathematical equations were presented including the conservation equations, turbulence, combustion, and radiation models. Next, the numerical model geometry, mesh structure, boundary conditions, discretization technique, and processing resources were presented. In the following chapter, the CFD model validation will be presented.

CHAPTER 3

CFD NUMERICAL MODEL VALIDATION

3.1 Introduction

In this chapter, the proposed combustor CFD numerical model is validated with experimental data from Taupin (2003); Taupin *et al.* (2007); Persis, Cabot, Pillier, Gökalp, & Boukhalfa (2013), fulfilling the first research sub-objective (A1).

3.2 CFD model validation

In this section, the combustor CFD numerical model validation is presented with respect to cold flow, non-reactive flow, and reactive flow.

3.2.1 Validation of cold flow

The air-only cold flow model is validated with Particle Image Velocimetry (PIV) data from Taupin (2003).

The global flow field is verified versus experimental data from Taupin (2003) in terms of the flow streamlines distribution inside the combustion chamber Region of Interest (ROI), including the formation of the Inner and Corner Recirculation Zones (IRZ and CRZ), shear layers, and the reversed flow regions. Figure 3.1 shows the 3D cold flow global flow field inside the combustion chamber. The flow can be distinguished by the IRZ, CRZ, and shear layers separating them, similar to the LP combustors flow pattern previously reported by Turns (2000). The CRZ stops at a height (z) of 30 mm, similar to Taupin (2003). The reversed flow occupies the entire combustion chamber and is extended up to the combustion chamber exit. This reversed flow is responsible for stabilizing the resulting flame by recirculating/reburning the far stream hot products into the flame region and hence ensures a continuous and uniform burning of the fuel-air mixture (Huang & Yang, 2005; Huang, Sung, Hsieh, & Yang, 2003).

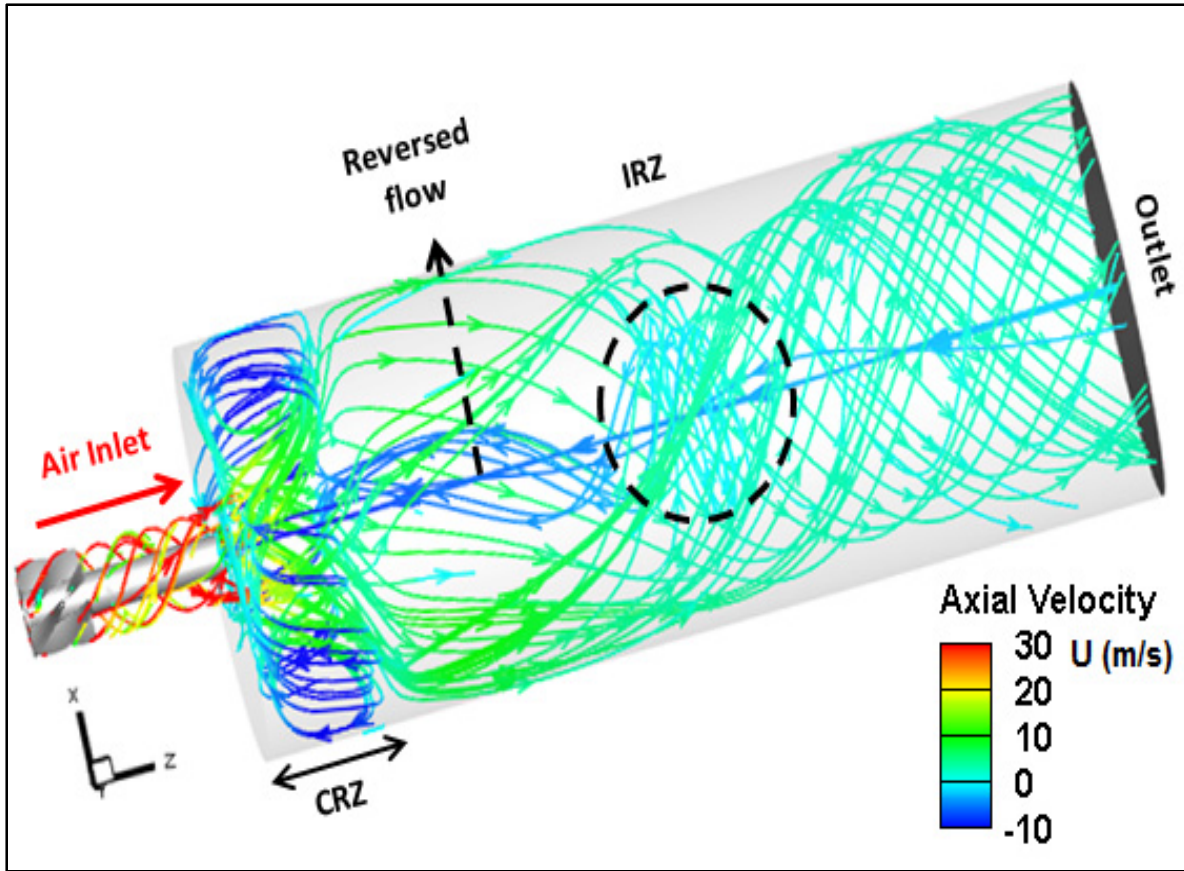


Figure 3.1 3D cold flow global flow field inside the combustion chamber

3.2.1.1 Quantitative analysis

A quantitative analysis is now presented to validate the CFD model by comparing the CFD-predicted results with the experimental data reported by Taupin (2003). First, the axial (u) and tangential (w) normalized velocities (the two components of the swirl physical definition) are compared with Taupin (2003) at the swirler outlet in Figure 3.2, where an accepted trend and values (of u and w) are observed at the swirler outlet.

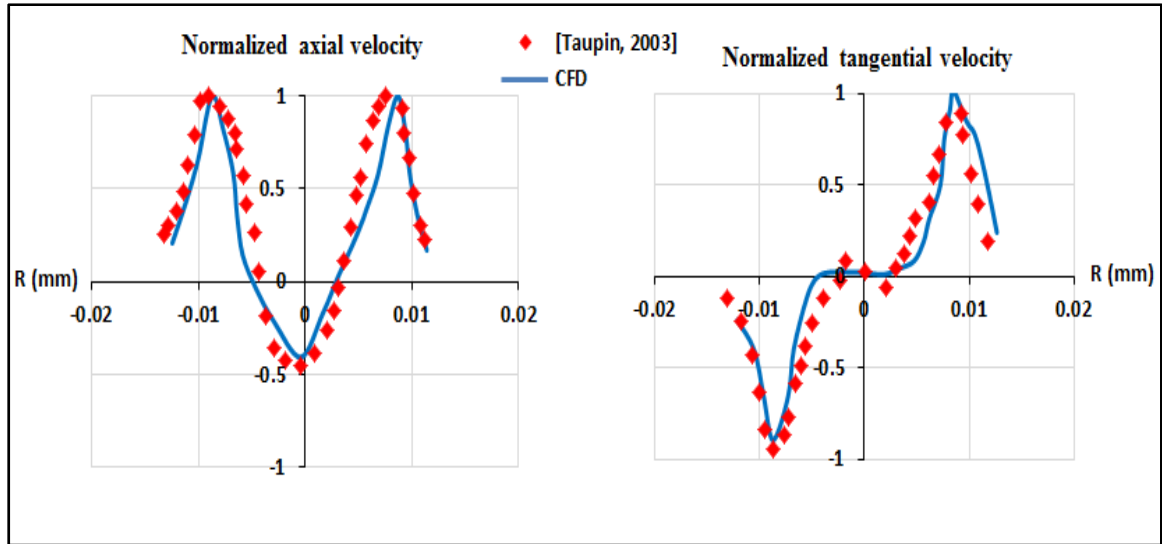


Figure 3.2 Comparisons of the cold flow normalized axial (left) and tangential (right) velocities at the combustion chamber entry, [Taupin, 2003] (red) and CFD (blue)

Then, the cold flow CFD-predicted tangential velocity (w) contours are compared to the ones measured by Taupin (2003) inside the combustion chamber, as seen in Figure 3.3. An accepted distribution of w is observed by the CFD with an average error of 3%. The maximum error is found to be near the burner longitudinal axis, where the higher velocity gradients exist. The average w is found to decrease gradually till reaching a minimal value of ≈ -35 m/s at the combustion chamber entrance at $R/D = 0.5$.

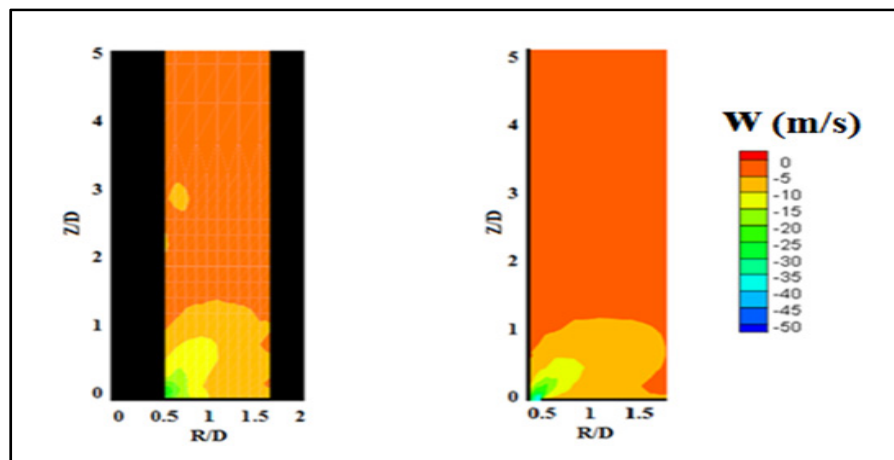


Figure 3.3 Cold flow tangential velocity contours inside the ROI measured by Taupin 2003 (left) and predicted by CFD (right)

Next, the cold flow CFD-predicted radial profiles of the normalized axial (u/u_m), radial (v/v_m), and tangential (w/w_m) averaged velocities are also compared at ten axial locations, namely from Z1 to Z10, which corresponds to Z/D from 0.22 to 4.78, respectively. However, results will be presented hereinafter at three axial locations for brevity. For all radial profiles, the radii (R) and height (Z) axes are normalized by the swirler diameter, $d_{sw} = D = 18$ mm.

Figure 3.4, Figure 3.5, and Figure 3.6 show the radial profiles of u/u_m , v/v_m , and w/w_m , respectively, at $Z/D = 0.22$ (top), 1.22 (middle), and 4.33 (bottom). These three axial locations are selected herein so as to show the general trend of a velocity component, where it starts with the highest gradient (at the combustion chamber entry, i.e. $Z/D = 0.22$) till it reach a flat trend at the ROI end (i.e. $Z/D = 4.33$). In general, an accepted similitude in trends and values are achieved by the CFD cold flow model for the radial profiles of the three swirling flow normalized velocity components (u/u_m , v/v_m , and w/w_m), as seen per Figure 3.4, Figure 3.5, and Figure 3.6, respectively.

Another conclusion is that a slight error (less than 5%) of velocity (axial, radial, or tangential) prediction appears only at the combustion chamber entry ($Z/D = 0.22$), where a velocity trend has the highest gradient. This slight error is attributed to the used modelling approach, especially that the combustion chamber entry is characterized by the highest velocity gradients. Elsewhere, the CFD has an accepted concordance with experimental data from Taupin (2003). The overall validation process is based on the maximum (peaks) and minimum values associated to each curve as well as its location in the axial (Z/D) and radial directions (R/D).

Regarding the two velocity components of swirling flow, axial and tangential, an accepted similitude (concordance) between the experimental data and numerical results is observed in Figure 3.4 for the normalized axial velocity as well as in Figure 3.6 for the normalized tangential velocity, indicating the capability of the used modelling approach to capture the swirling flow aerodynamics.

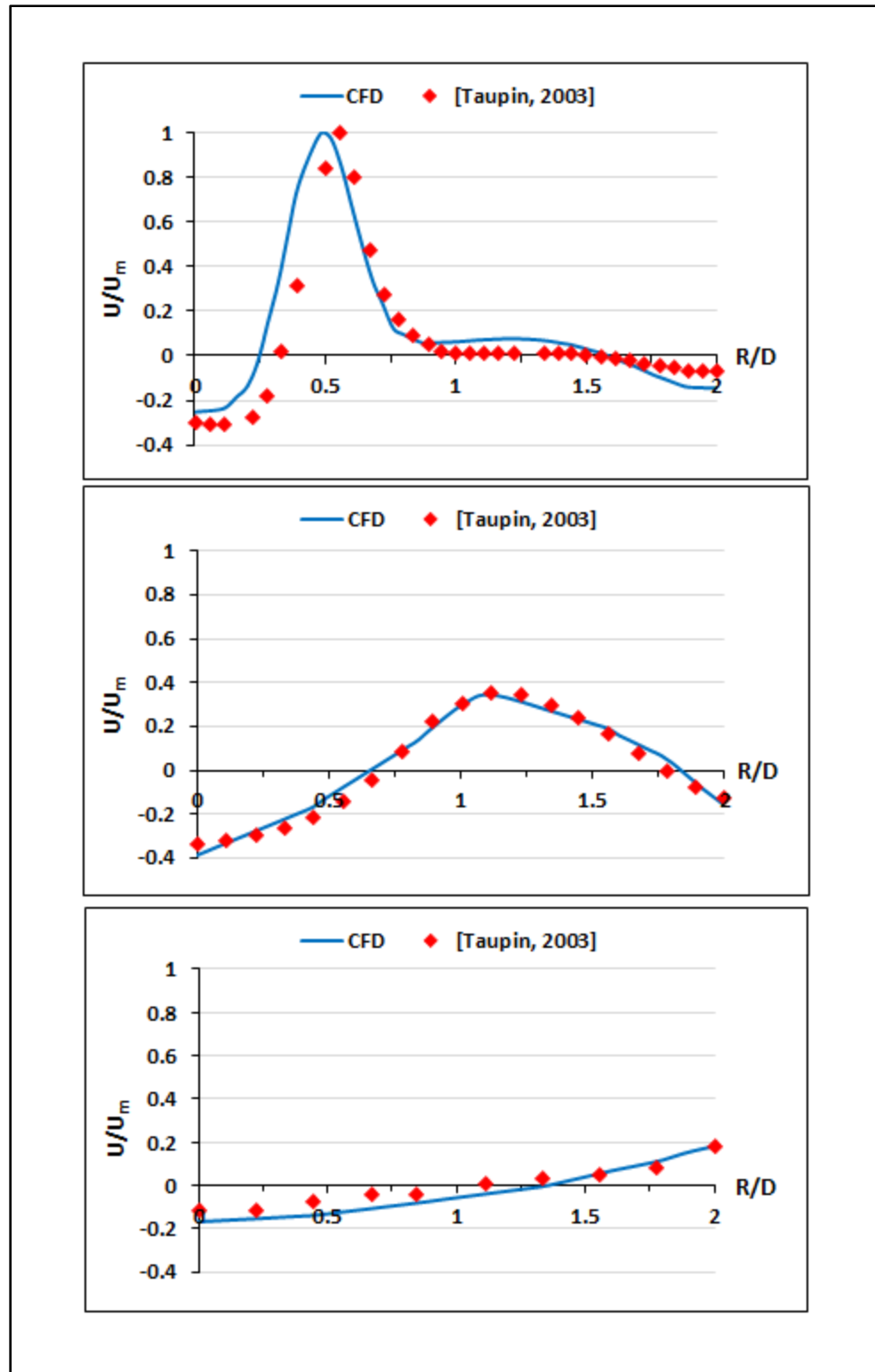


Figure 3.4 Cold flow normalized axial velocity radial profiles at $Z/D = 0.22$ (top), $Z/D = 1.22$ (middle), and $Z/D = 4.33$ (bottom)

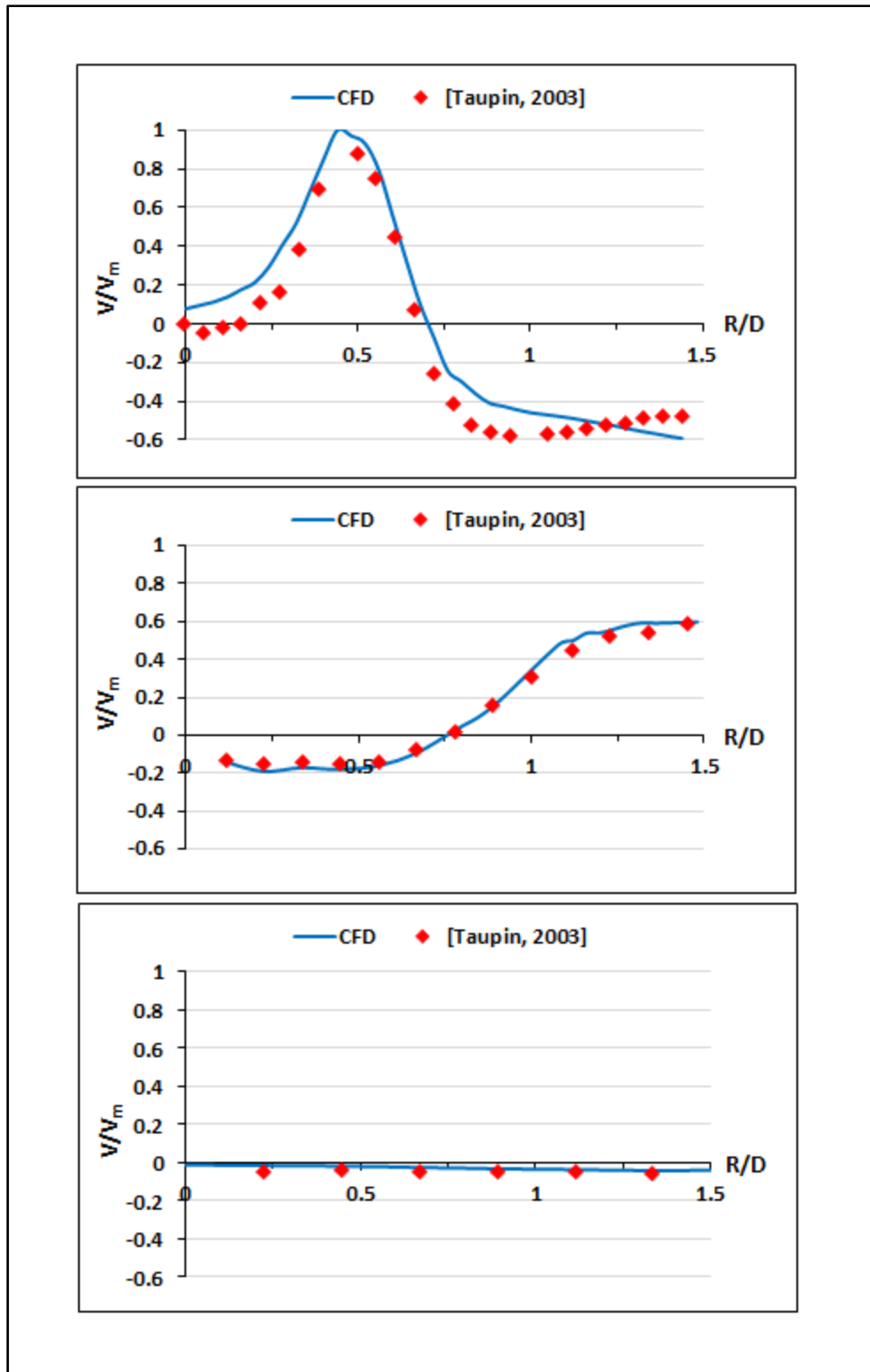


Figure 3.5 Cold flow normalized radial velocity radial profiles at $Z/D = 0.22$ (top), $Z/D = 1.22$ (middle), and $Z/D = 4.33$ (bottom)

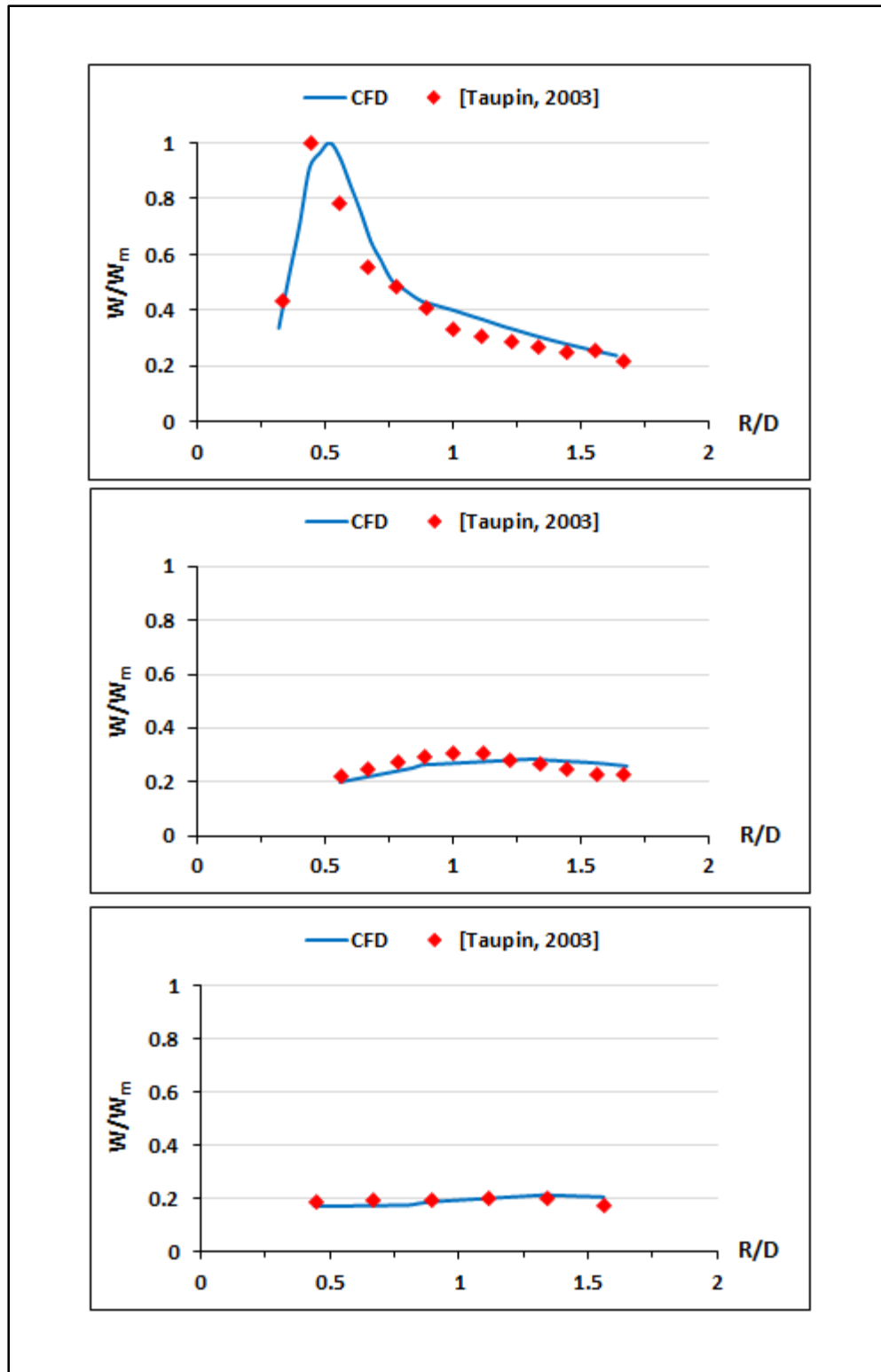


Figure 3.6 Cold flow normalized tangential velocity radial profiles at $Z/D = 0.22$ (top), $Z/D = 1.22$ (middle), and $Z/D = 4.33$ (bottom)

Now, the CFD predicted cold flow axial velocity evolution along the combustor longitudinal axis (blue dots) is compared in Figure 3.7, where an accepted similitude is observed. It can be seen that the axial velocity possesses a negative value along the shown combustor length ($Z/D = 7$), indicating the existence of the reversed flow region along the shown axial distance. The axial velocity decays suddenly in the region $Z/D < 0.75$ then increases sharply till $Z/D = 2$, before asymptotically approaching an axial velocity of zero. The same behavior have been reported by Maccallum (1967); S. Poireault (1997) as well as identified by Taupin (2003).

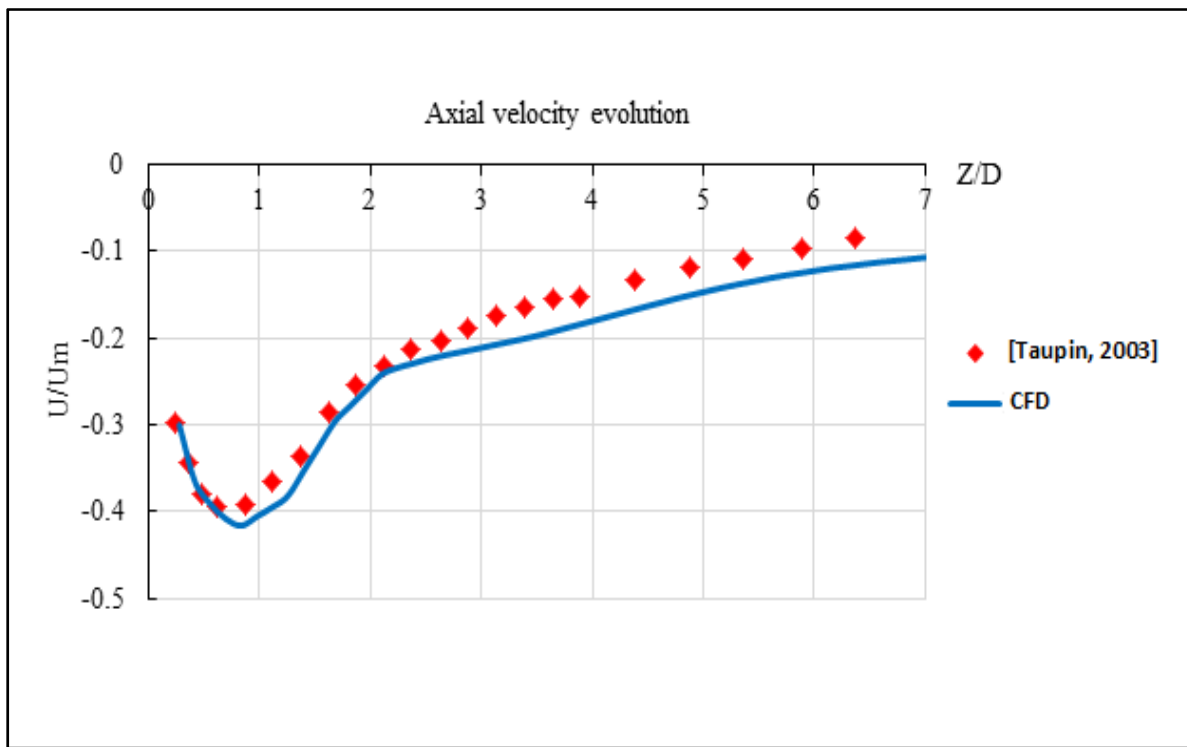


Figure 3.7 Cold flow axial velocity evolution along the combustor longitudinal axis, Taupin (2003) in red dots and CFD in blue line

From Figure 3.7, it can also be seen that the error (less than 5%) of the axial velocity prediction is relatively small at $Z/D \leq 2$, as compared to the studied length, due to the refined element size at the combustion chamber entry.

The position of the cold flow zero iso-velocity line (i.e. $u/u_m = 0$) in the radial-axial plane was also compared with Taupin (2003) and an accepted trend was observed, indicating the possibility that the combustor could suck air from the outside, similarly to Taupin (2003). Results are not presented in order to shorten the dissertation.

3.2.2 Validation of non-reactive flow

Following the cold flow model validation, the combustor non-reactive methane-air flow model (methane-air mixture without reaction) is verified at an overall equivalence ratio of 0.7, based on the methane and air mass flow rates in order to assess the methane-air turbulent mixing.

Figure 3.8 shows the CFD-predicted radial equivalence ratio profiles compared to Taupin (2003) at four axial locations, $Z/D = 0.01, 0.1, 0.5$, and 1. An accepted coincidence is observed at the four axial locations, where the methane-air mixture fluctuates between rich at the center ($-0.5 \geq R/D \leq 0.5$) and lean elsewhere at the first three locations ($Z/D = 0.01, 0.1$, and 0.5), unlike for $Z/D = 1$, where the mixture becomes homogenous and ϕ corresponds to the nominal value (0.7) at which the methane-air mixing was studied. The mixture inhomogeneity at the combustion chamber entrance is attributable to the mixing technique used, in which methane is injected radially in the upstream of the swirler and then runs preferentially along the bluff body. The same observation was reported by Taupin (2003), who affirmed that the rich zones at the combustion chamber entrance will behave as a pilot fuel.

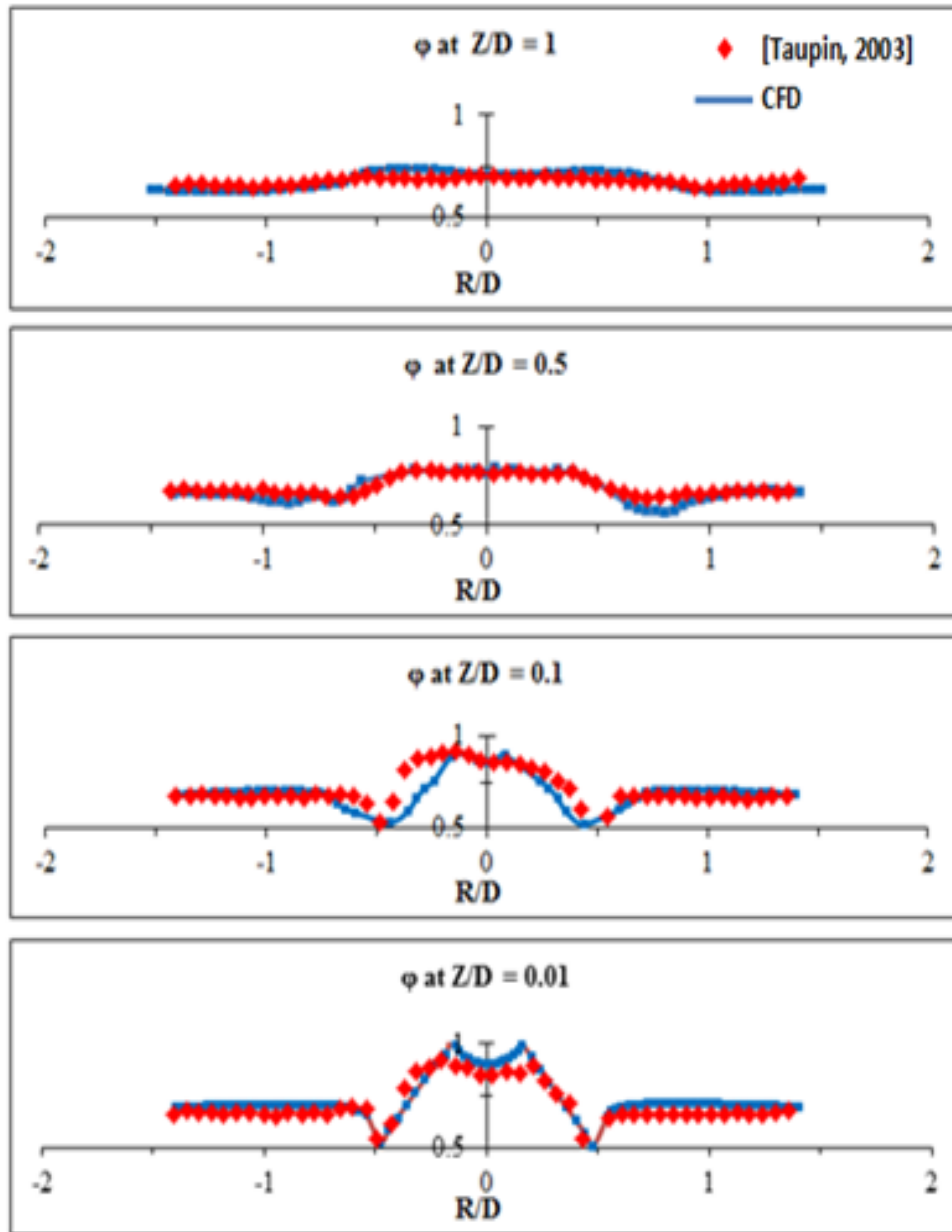


Figure 3.8 Non-reactive flow equivalence ratio radial profiles at four axial locations, Taupin (2003) in red and CFD in blue

3.2.2.1 Different non-reactive flow equivalence ratios

Beside the basic equivalence ratio ($\phi = 0.7$), the non-reactive flow model is extended to consider leaner equivalence ratios. Further validation is pursued in order to assess the methane-air turbulent mixing at a wide range of lean burning conditions.

Figure 3.9 shows the radial profiles of equivalence ratio (ϕ) at the combustion chamber entrance ($Z/D = 0.01$) for Taupin (2003) in red symbols and the CFD prediction (in blue line) for five equivalence ratios: 0.6 (top left), 0.63 (middle left), 0.65 (bottom), 0.68 (top right), and 0.7 (middle right).

An accepted trend is observed for all studied equivalence ratios, where the equivalence ratio starts from near one at the combustor symmetric axis ($R/D = 0$), and then decreases abruptly until reaching a minimum at $R/D = 0.5$, where it increases sharply again until reaching its nominal value starting from $R/D = 0.6$, where it does not evolve significantly for higher radii.

Based on non-reactive flow comparisons, the equivalence ratio inhomogeneity at the combustion chamber entrance is identified and linked to the mixing technique, as reported by Taupin (2003).

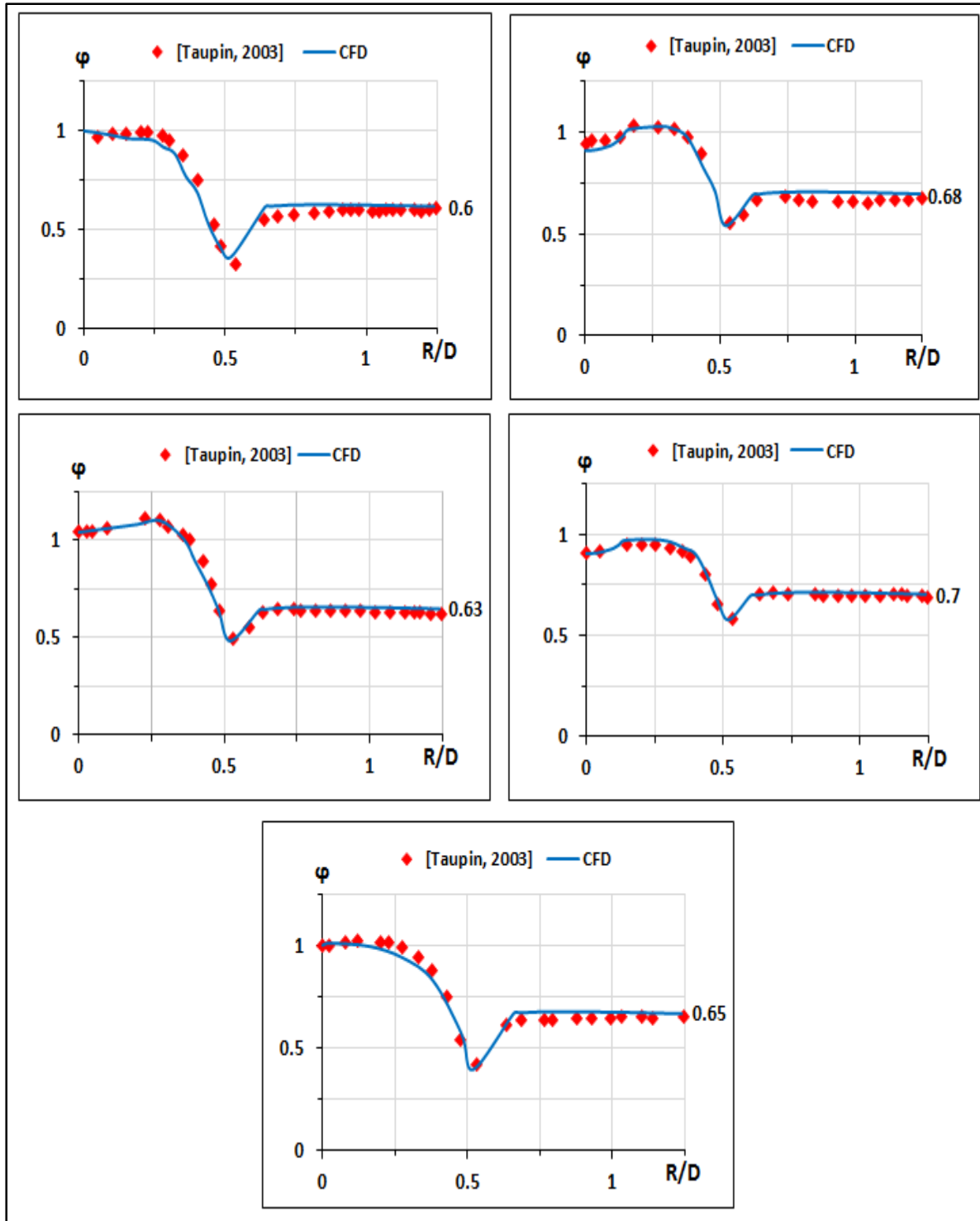


Figure 3.9 Non-reactive flow equivalence ratio radial profiles at the combustion chamber entry ($Z/D = 0.01$) for $\phi = 0.6$ (top left), 0.63 (middle left), 0.65 (bottom), 0.68 (top right), and 0.7 (middle right)

3.2.3 Validation of reactive flow ($\phi = 0.65$)

Following the validation of the cold and non-reactive flow models, the combustor reactive flow model is validated at $\phi = 0.65$. The reactive flow validation is divided into two parts: first, the reactive flow aerodynamics, including the normalized axial and radial velocities, and second, the reactive flow chemical data, such as the flame shape, AFT, and NO_x level.

3.2.3.1 Reactive flow aerodynamics

First, the reactive flow CFD predicted radial profiles of the normalized axial (u/u_m) and radial (v/v_m) averaged velocities are compared to Taupin (2003) profiles at an equivalence ratio of 0.65 at ten axial locations, Z/D from 0.22 to 4.78, however, results are presented in Figure 3.10 and Figure 3.11 at $Z/D = 0.22$ (top), 1.22 (middle), and 4.33 (bottom). The local axial and radial velocities are normalized by their respective CFD predicted cold flow maximums ($u_m = 29.8$ m/s and $v_m = 15.2$ m/s) following the procedure of Taupin (2003).

In general, an accepted similarity in trends and values is achieved by the CFD reactive flow model for the normalized axial and radial velocities at the three axial locations, considering that a slight error appears at $Z/D = 0.22$, where velocity is characterized by the highest fluctuations. In addition, the uncertainty in the experimental results of Taupin (2003) is reported to be in the order of 2.5 % (Taupin, 2003).

Looking at Figure 3.10 and Figure 3.11, it can be seen that the general trend of a velocity component (either u or v) is identified by the highest gradient (at the combustion chamber entry, i.e. $Z/D = 0.22$), then the trend approaches a gradual flat radial profile till the ROI end (i.e. $Z/D = 4.33$).

It can be also seen that the peaks of axial velocity (at $Z/D = 0.22$) are ≈ 1.25 greater than that of cold flow, due to CH_4 -air reaction, which is translated into an increase of the flow basic velocity component (U), similarly to Taupin (2003).

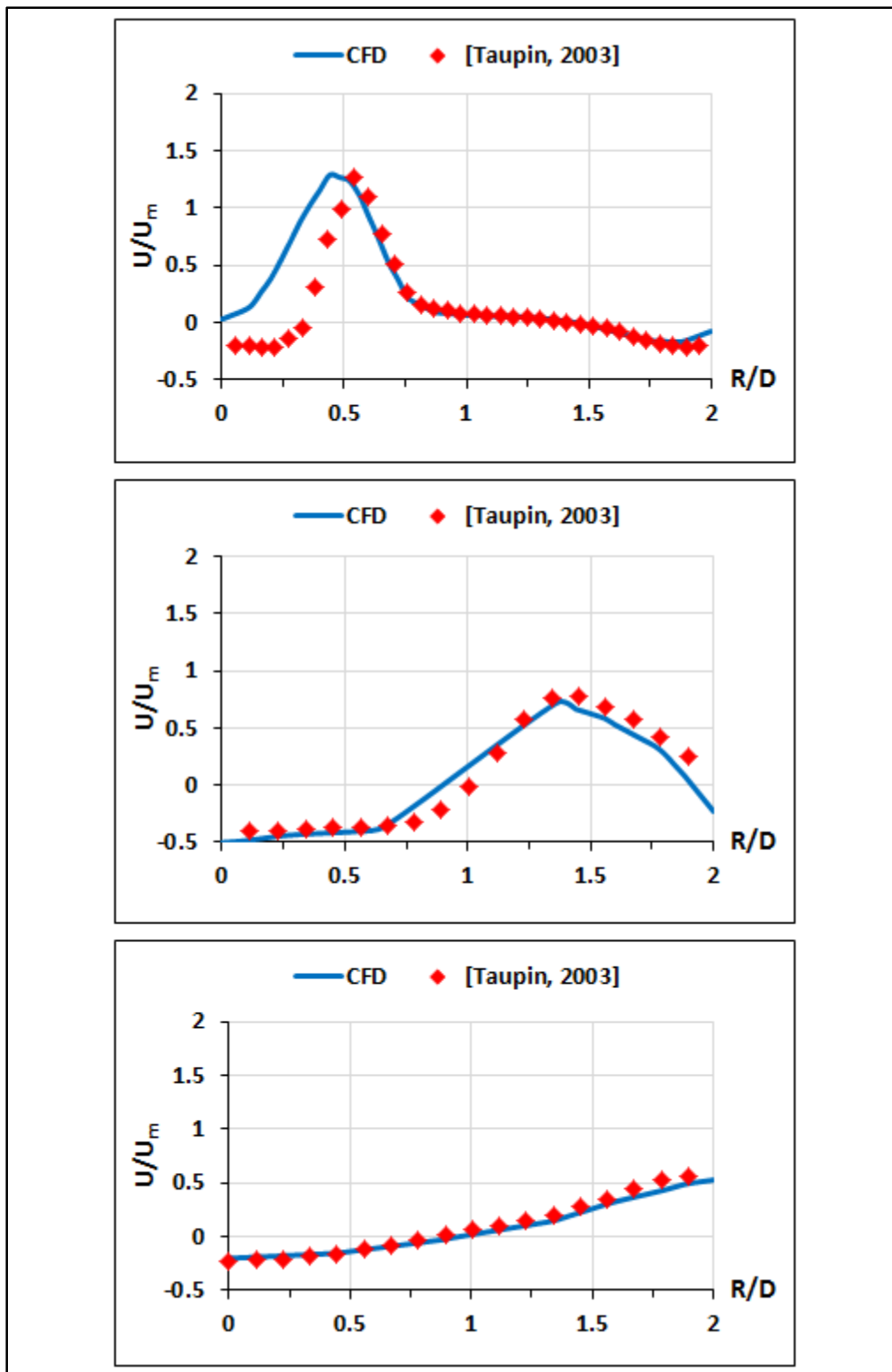


Figure 3.10 Reactive flow ($\phi = 0.65$) normalized axial velocity radial profiles at $Z/D = 0.22$ (top), $Z/D = 1.22$ (middle), and $Z/D = 4.33$ (bottom)

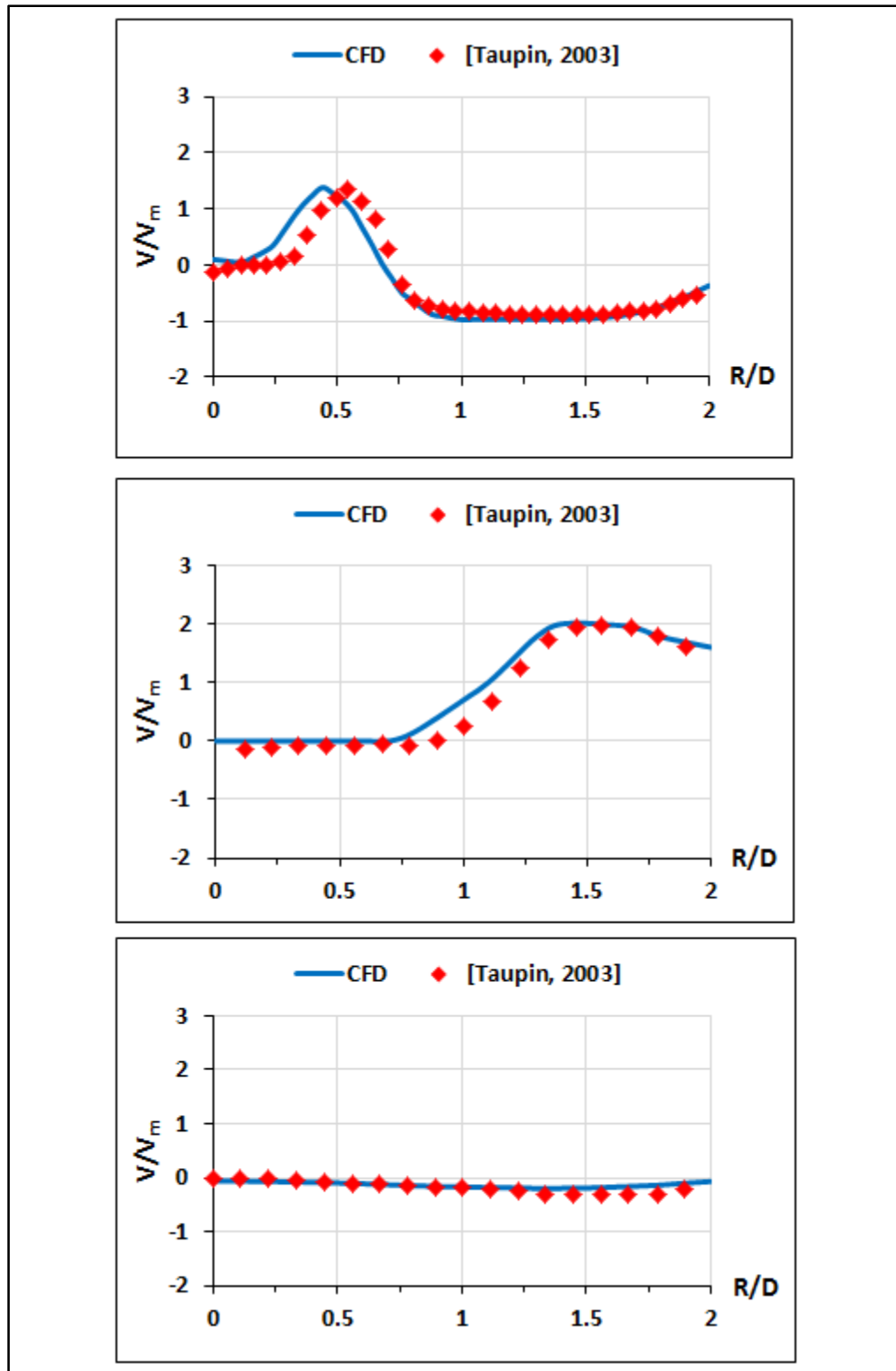


Figure 3.11 Reactive flow ($\phi = 0.65$) normalized radial velocity radial profiles at $Z/D = 0.22$ (top), $Z/D = 1.22$ (middle), and $Z/D = 4.33$ (bottom)

3.2.3.2 Reactive flow chemical data

The CFD reactive flow model ($\phi = 0.65$) will now be compared to Taupin (2003); Taupin *et al.* (2007); Persis *et al.* (2013) in terms of the flame shape, AFT, NO_x level at the burner's outlet, and combustion regime.

First, Taupin's visible flame photograph (top) is compared in Figure 3.12 to the CFD flame shape based on the AFT (middle), similarly to Samiran *et al.* (2019), or to OH radical mass fraction (bottom), similarly to Ali *et al.* (2020) for similar swirling conditions, $S = 0.9$ and $\alpha = 50^\circ$. An accepted similitude is observed between the CFD-predicted OH distribution and the visible flame shape, as OH is partly responsible for flame visible radiative emissions (Samaniego, Egolfopoulos, & Bowman, 1995).

Next, the CFD-predicted AFT at an inlet preheat condition of 600 K and $\phi = 0.7$ is compared to the kinetic study of the same flame by Persis *et al.* (2013), who reported an AFT of 2043 K, whereas a value of 2050 K is obtained with the proposed model herein. In addition, the CFD-predicted AFT at an ambient inlet temperature (300 K) is compared to the same kinetic study of Persis *et al.* (2013), who reported an AFT of 1820 at $\phi = 0.7$, whereas a value of 1800 K is obtained by the proposed model at $\phi = 0.65$.

Last, the CFD model can predict 2 ppm of NO_x at the burner's outlet for methane-air combustion at $\phi = 0.7$, which is exactly the value reported by Persis *et al.* (2013). Moreover, the CFD model could predict a Damköhler number (Da) of ≈ 7 for methane-air combustion at $\phi = 0.7$, whereas Taupin *et al.* (2007) reported $\text{Da} \approx 10$ at $\phi = 0.65$. Hence, the combustion regime is located as "Thin reactions sheets" in the Borghi diagram, as reported by Taupin *et al.* (2007) and verified numerically herein.

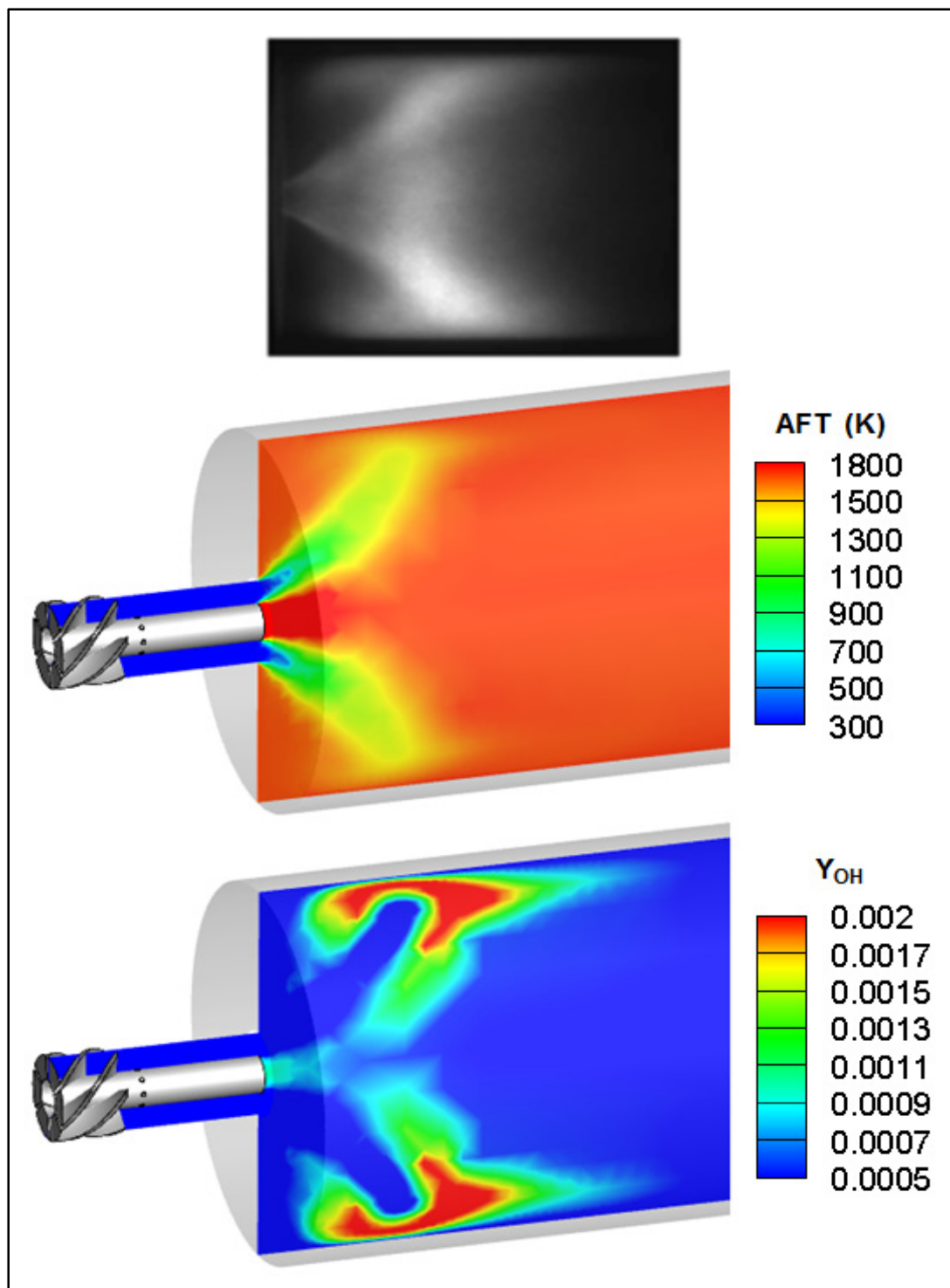


Figure 3.12 Flame shape validation versus Taupin (top) in terms of the CFD predicted AFT (middle) and OH radical (bottom), case methane-air combustion at $\phi = 0.65$

Based on the preceding validations, the pursued/proposed numerical model of the studied combustor (burner) has been judged satisfactory, which allows to meet the first research sub-objective (A1).

3.3 Chapter conclusions

The combustor numerical model has been validated versus experimental data from Taupin (2003); Taupin *et al.* (2007); Persis *et al.* (2013). The validation was in terms of cold flow, non-reactive, and reactive flow (at $\phi = 0.65$), respectively. In general, an accepted matching has been achieved for cold flow aerodynamics, non-reactive flow (methane-air turbulent mixing), reactive flow aerodynamics, and reactive flow characteristics, such as, AFT, flame shape, NO_x levels, and combustion regime.

Now, the first research sub-objective (A1) has been reached. In the next chapter, the CFD numerical model will be used to study HEC.

CHAPTER 4

HYDROGEN-ENRICHED COMBUSTION

Following the validation of the combustor numerical model, the investigation now looks over the effect of hydrogen addition to methane on the different combustion parameters and emissions, which will allow to reach the second research sub-objective, A2.

4.1 CFD reactive flow model modification with respect to hydrogen addition

The CFD reactive flow model of the basic swirl configuration ($\alpha = 50^\circ$) is modified in order to consider the methane enrichment by hydrogen, through a modification of the FGM table using the GRI 3.0 mechanism. The fuel composition is modified in order to consider hydrogen addition based on a molar/volume basis. Hydrogen-Enriched Combustion (HEC) is studied at a constant equivalence ratio. Four equivalence ratios ($\phi = 0.65, 0.7, 0.85, \text{ and } 1$) are numerically studied, however, the results will be presented for $\phi = 0.7$ and 1 for brevity. For each studied equivalence ratio, the hydrogen concentration in the $\text{H}_2\text{-CH}_4$ blend, named hereinafter the Hydrogen Volumetric Ratio (HVR), varies from 0 to 90%, however, results for some particular HVRs will be presented herein for clarity and brevity. This wide range of HVRs and equivalence ratios helps extending the HEC approach towards industrial GTE, used for power generation purpose.

4.2 Effect of hydrogen addition

In this section, the effect of hydrogen addition to methane on AFT, total energy, combustion diffusivity, global flow field, flame shape, main species concentration, vorticity, temperature field and NO_x emissions is identified. Hence, the reference case ($\text{CH}_4\text{-air}$ combustion at $\phi = 0.7$) is compared to HEC with an HVR increase of up to 90% at a fixed swirl level of $S = 0.9$ ($\alpha = 50^\circ$). Moreover, the stoichiometric $\text{CH}_4\text{-air}$ combustion is compared to HEC (with HVR up to 60%) at the same swirl level.

4.2.1 H₂ addition effect on AFT

The effect of hydrogen addition to methane on the Adiabatic Flame temperature (AFT) is shown in Figure 4.1, where each point represents the maximum CFD-predicted temperature (inside the wake region at the combustion chamber entry) for CH₄-air combustion and HEC (with HVR = 25, 50, 75, and 90%) at $\phi = 0.7$. It can be seen that increasing HVR from 0 to 90% results in an increase of AFT from ≈ 2230 to ≈ 2345 K, respectively. This increase is related to the high H₂ reactivity/combustibility associated with an HVR increase. For HEC with HVR = 25%, the AFT increased by only 15 K (compared to CH₄) indicating that the 25-75% H₂-CH₄ blend could replace CH₄ during the primary stages of GTE operation, but other calculations are needed to determine the cooling requirements.

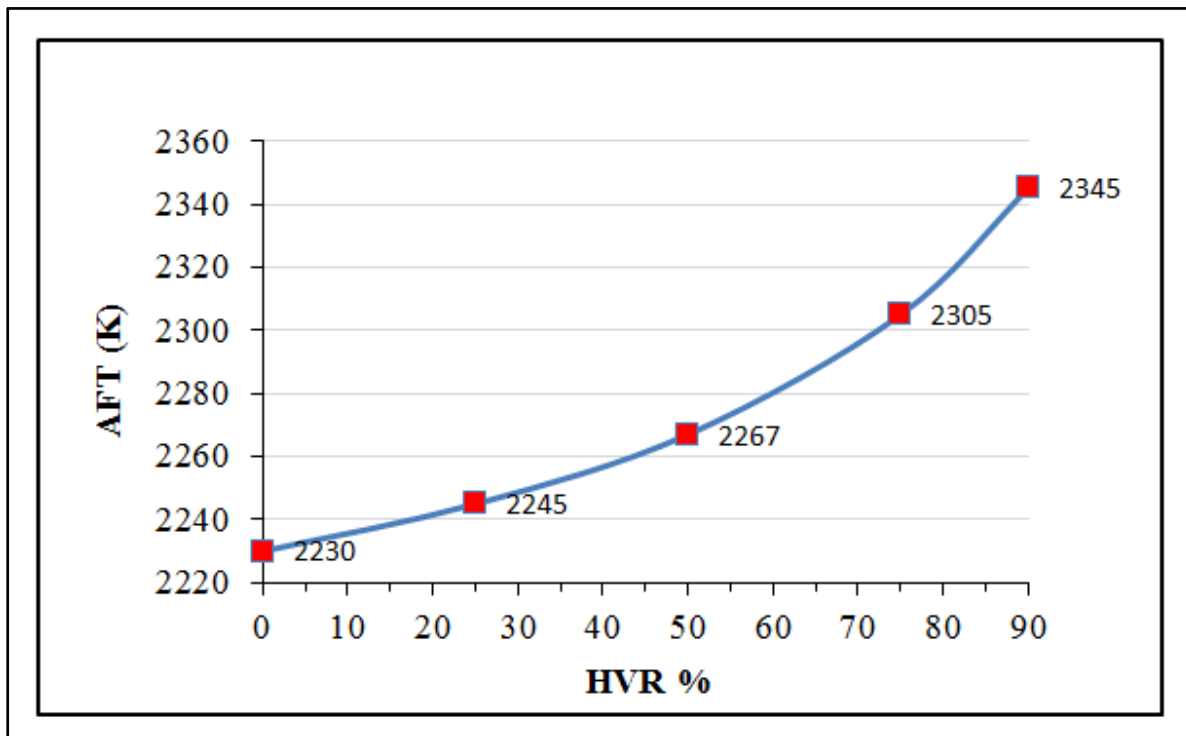


Figure 4.1 AFT versus HVR plot at $\phi = 0.7$ where each point represents the maximum CFD-predicted temperature inside the wake region for methane and HEC with HVRs = 25, 50, 75, and 90%

4.2.2 H₂ addition effect on the global flow pattern and vorticity

The effect of H₂ addition on the global flow field is presented in Figure 4.2, which shows the 2D streamlines mapped over the axial velocity contours inside the ROI for the reference CH₄ case (top left) and HEC with HVR = 25% (top right), 50% (bottom left), and 90% (bottom right) at $\phi = 0.7$. It can be seen that all flow patterns show the formation of a centered reversed flow (i.e. IRZ) and recirculation flow inside corners (namely CRZ), but that H₂ addition decreases (in a non-linear relationship with H₂ concentration) the size of centered regions with the highest negative axial velocity ($u = -10$ m/s). These effects are attributable to the high reactivity of H₂, which speeds up reactions and raises the reaction zone temperature. The effect of H₂ addition appears clearer for the case with the highest HVR (90%), which shows a shorter IRZ (than cases with H₂ up to 50%) and illustrates the non-linear behaviour of H₂ addition on the flow structure. However, the flow remains characterized by the IRZ - responsible for stabilizing the flame by recirculating the hot gas back to the flame base - including the case with 90% H₂. This conclusion infers that up to 90% H₂ could be mixed with CH₄ in the LP combustors operating at high turbulence levels and under lean burning conditions, based on RANS calculations, as also reported by Day, Tachibana, Bell, Lijewski, Beckner, & Cheng (2012); Meziane & Bentebbiche (2019). More investigations are needed to confirm this possibility.

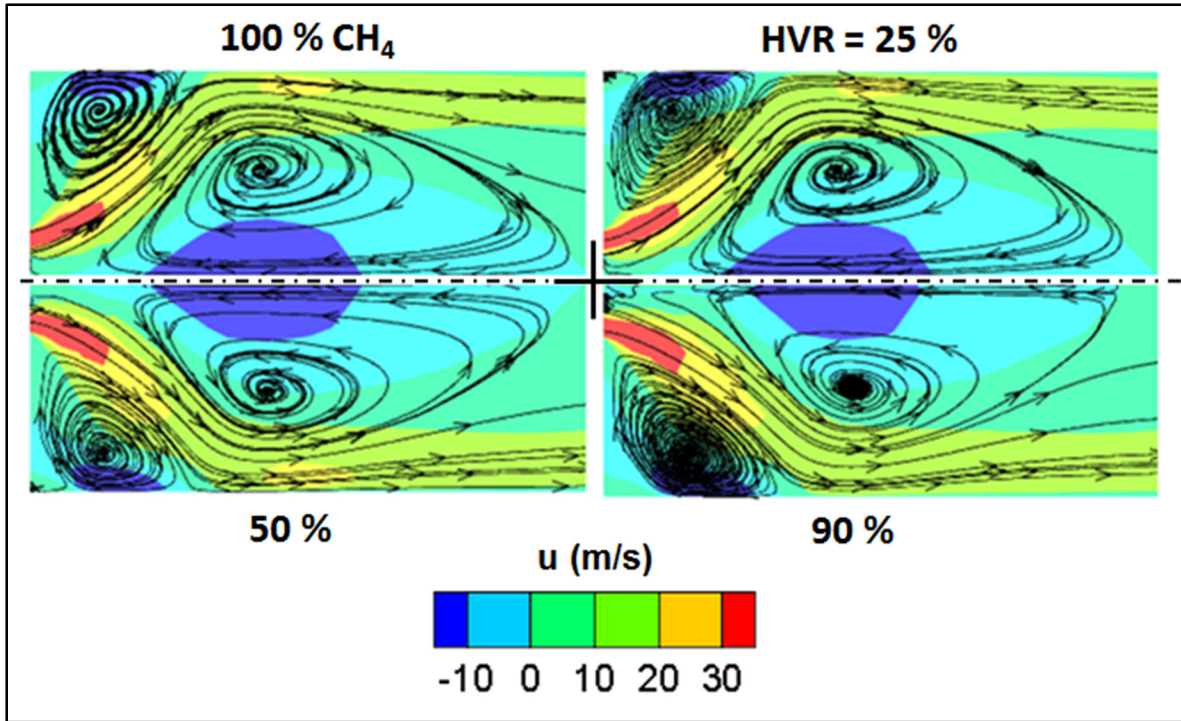


Figure 4.2 2D streamlines distribution inside the ROI at $\phi = 0.7$ mapped over the axial velocity contours for methane (top left) and HEC with HVR = 25% (top right), 50% (bottom left), and 90% (bottom right)

For further analysis, the 2D streamlines were mapped over the contours of temperature (top) and OH radical (bottom) in Figure 4.3, for the same fuel and equivalence ratio studied above. The same observations were identified for the flow pattern accompanied by a general increase in the temperature and OH radical with an increased H_2 addition. The IRZ is characterized by a high temperature and is responsible for recirculating the far stream flow into the upstream, where the flame exists and reactions take place (Huang & Yang, 2005). On the other hand, the CRZ is responsible of producing relatively cooler corners, as seen for all cases. Thus, the combustion phenomenon is characterized by a hot centered flame, relatively cooler corners which convolute the flame, and the post-flame region. Further analyses will be presented regarding the temperature and OH later on.

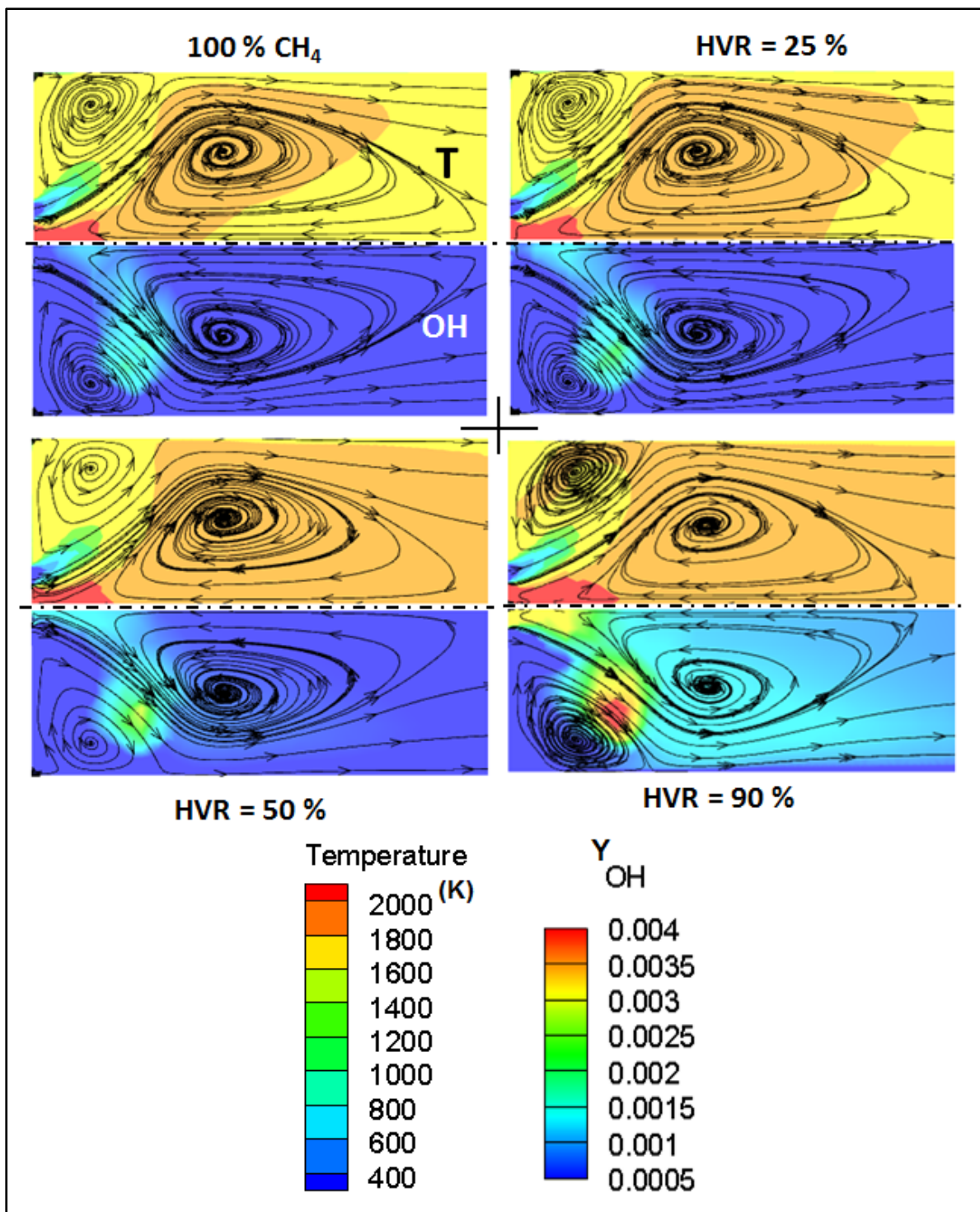


Figure 4.3 2D streamlines distribution inside the ROI at $\phi = 0.7$ mapped over the contours of temperature (up) and OH radical (down) for methane (top left) and HEC with HVR = 25% (top right), 50% (bottom left), and 90% (bottom right)

Beside the 2D flow visualization, flow was visualized at $\phi = 0.7$ using 3D streamlines inside the entire combustion chamber length in Figure 4.4 by comparing the reference CH_4 case (top) and HEC with $\text{HVR} = 75\%$ (bottom). A shift of the IRZ location by 20 mm in the downstream direction was identified for the case with $\text{HVR} = 75\%$. A similar trend was reached by Kim *et al.* (2009 a), who reported that hydrogen addition shifts the upstream stagnation location to downstream locations.

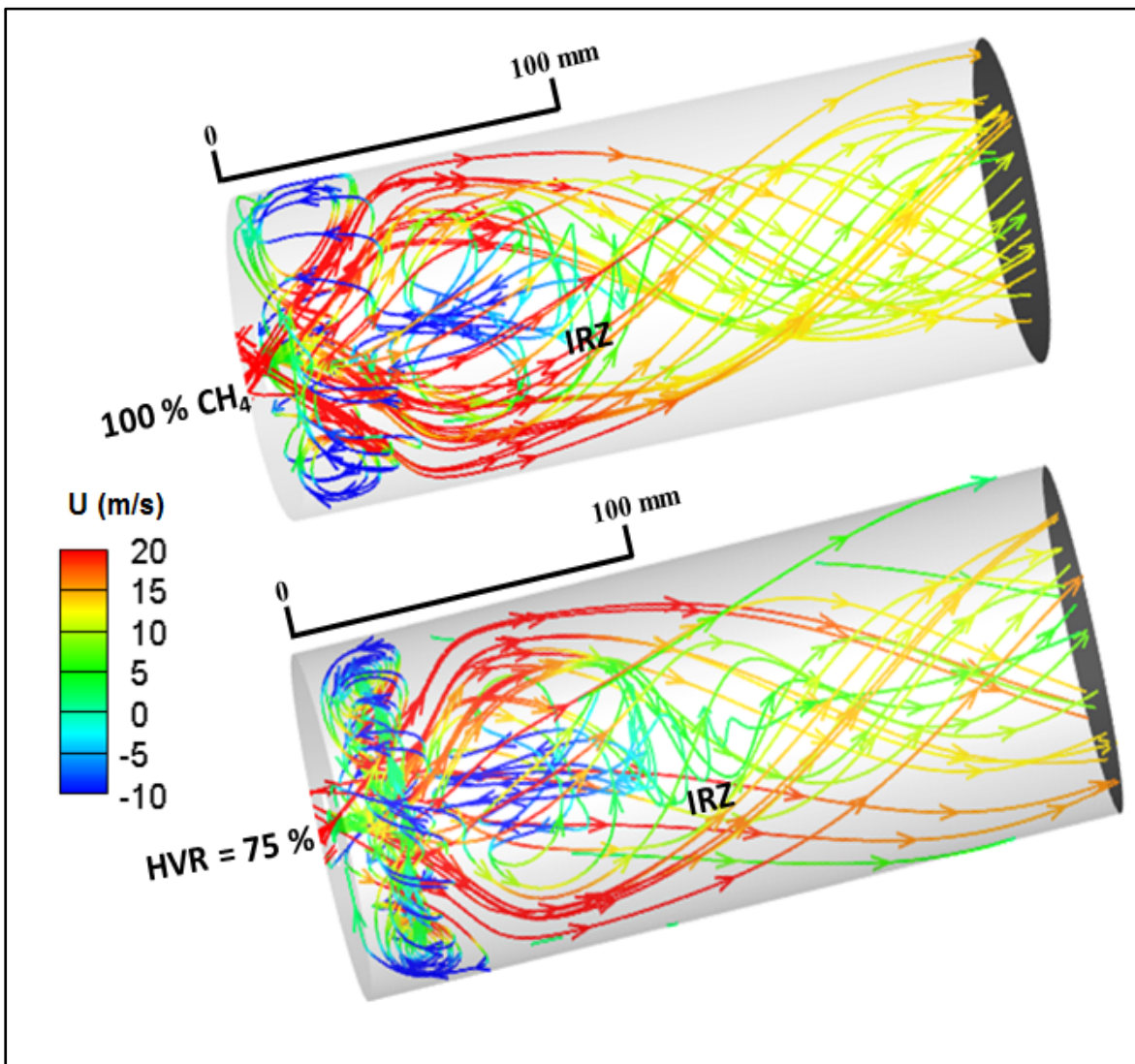


Figure 4.4 3D streamlines distribution inside the entire combustion chamber at $\phi = 0.7$ (colored by the axial velocity) for methane (top) and $\text{HVR} = 75\%$ (bottom)

Similar trends were observed for the stoichiometric HEC with HVR up to 60%. For 75 and 90% H₂, the flow could not properly reproduce the IRZ. However, a unidirectional flow filled the entire combustion chamber and hence an irregular temperature distribution is observed inside the entire combustion chamber length, indicating that the flame is unlikely to be stable. Results are not presented herein, but in the Appendix II “Unstable results”. A similar trend was identified for the stoichiometric flames of Nemitallah *et al.* (2019), who reported that any trial to increase HVR above 55% (at $\phi = 1$) failed and the flame extinguished, due to the occurrence of flashback (Nemitallah *et al.*, 2019).

The analysis is now extended to study the influence of hydrogen addition to methane on vorticity, which is the tendency of a continuum to rotate (Anderson, 2017). Vorticity is of interest herein as it plays an important role in determining the flow entrainment and flame evolution inside the ROI (Ali *et al.*, 2020).

Figure 4.5 shows the contours of the vorticity magnitude inside the ROI for CH₄ (top left) and HEC with HVR = 25% (top right), 50% (bottom left), and 90% (bottom right). It can be observed that, methane and HEC with HVR = 25 % have the same vorticity level throughout the entire ROI, under the studied turbulence level. Moreover, at up to 50% H₂, the distribution of the vorticity magnitude inside the ROI is close, with a slight increase of the vorticity level ($\omega = 8000 \text{ s}^{-1}$) for HEC with HVR = 50 % at the combustion chamber entry, near the burner’s longitudinal axis. With further H₂ concentration increases (to 90%), the corresponding vorticity level increase at the combustion chamber entry becomes clearer. This increase indicates that increasing the H₂ concentration in the fuel blend results in more intense or violent flames (Nemitallah *et al.*, 2019).

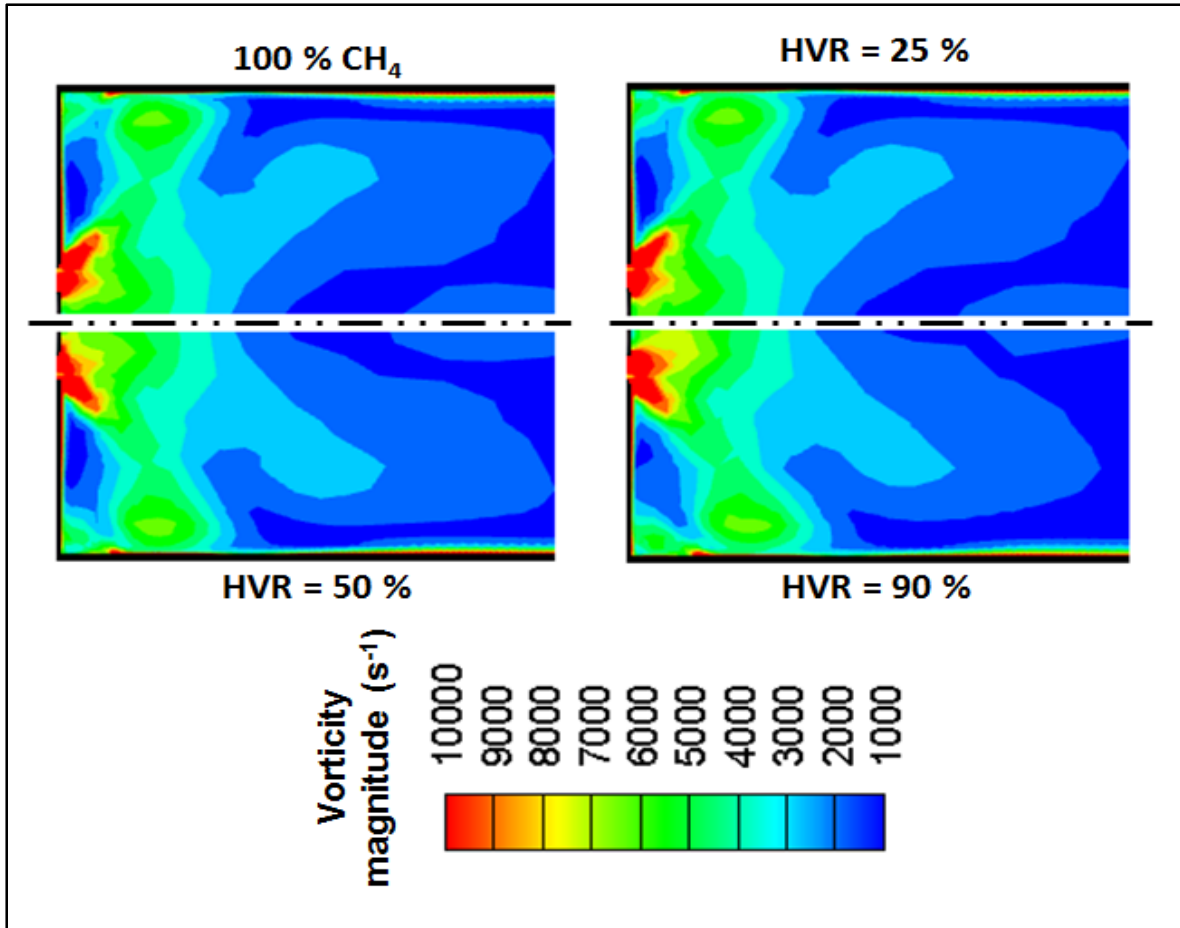


Figure 4.5 Vorticity magnitude contours inside the ROI at $\phi = 0.7$ for methane (top left) and HEC with HVR = 25% (top right), 50% (bottom left), and 90% (bottom right)

4.2.3 H₂ addition effect on the flame shape

The analysis will now proceed by identifying the influence of hydrogen addition to methane on the flame shape using two parameters, the OH radical and the progress variable. This approach is followed as the former (OH radical) is linked to the reaction zone and is partly responsible for the flame visible radiative emissions (Samaniego, Egolfopoulos, & Bowman, 1995), while the latter (progress variable, c) indicates the transition from the unburnt mixture to completely burnt products. Hence, both parameters allow identifying the changes of the flame shape and length with H₂ addition.

Figure 4.6 shows the 2D flame visualization inside the ROI at $\phi = 0.7$ using the OH radical (up) and c (down) for the CH₄ flame (top left) and HEC with HVR = 25% (top right), 50% (bottom left), and 90% (bottom right), followed by a 3D flame visualization using the iso-OH mass fraction surfaces for HEC with HVR = 25% (base left) and 90% (base right). It can be observed that increasing HVR increases the OH distribution as well as the size of the reaction zone inside the ROI, similarly to the results reported by Schefer (2003); Hawkes & Chen (2004). This increase is attributed to the increased H, O, and OH radical concentrations of the hydrogen enriched flames (Kim *et al.*, 2009 a). The effect of H₂ is clearer for the case with HVR = 90% than for the case with HVR = 25%, which appears to be similar to the reference CH₄ case, under the studied conditions. The OH radical increase with HVR increase can be also identified through the iso-OH mass fraction surfaces in the same figure (base) by comparing the lowest (25%) and highest (90%) H₂ concentrations.

When combining the OH distribution with the results from the progress variable, it can be observed that H₂ addition results in longer and thicker flames, which can be distinguished by the wider contours of $c = 0.7, 0.75, 0.8, 0.85$, and 0.9 , representing the transition from the unburnt mixture state ($c = 0.05$) to the completely burnt products ($c = 0.95$). This flame stretch is attributable to the interaction between the high turbulence and high reactivity of hydrogen. The same effect of hydrogen was identified for the stoichiometric HEC, with HVR up to 60%. Results are not presented for brevity.

The above conclusion highlights the importance of studying HEC at high turbulence levels, as turbulence affects the flame shape and length in a totally different manner than for quasi-laminar or even wrinkled flames, such as the flames studied by Ali *et al.* (2020); Nemitallah *et al.* (2019), where hydrogen addition resulted in shorter flames. This difference is related to the fact that HEC is studied herein for an inlet bulk velocity 6 times that of these flames, which were more governed by the chemical kinetics than turbulence.

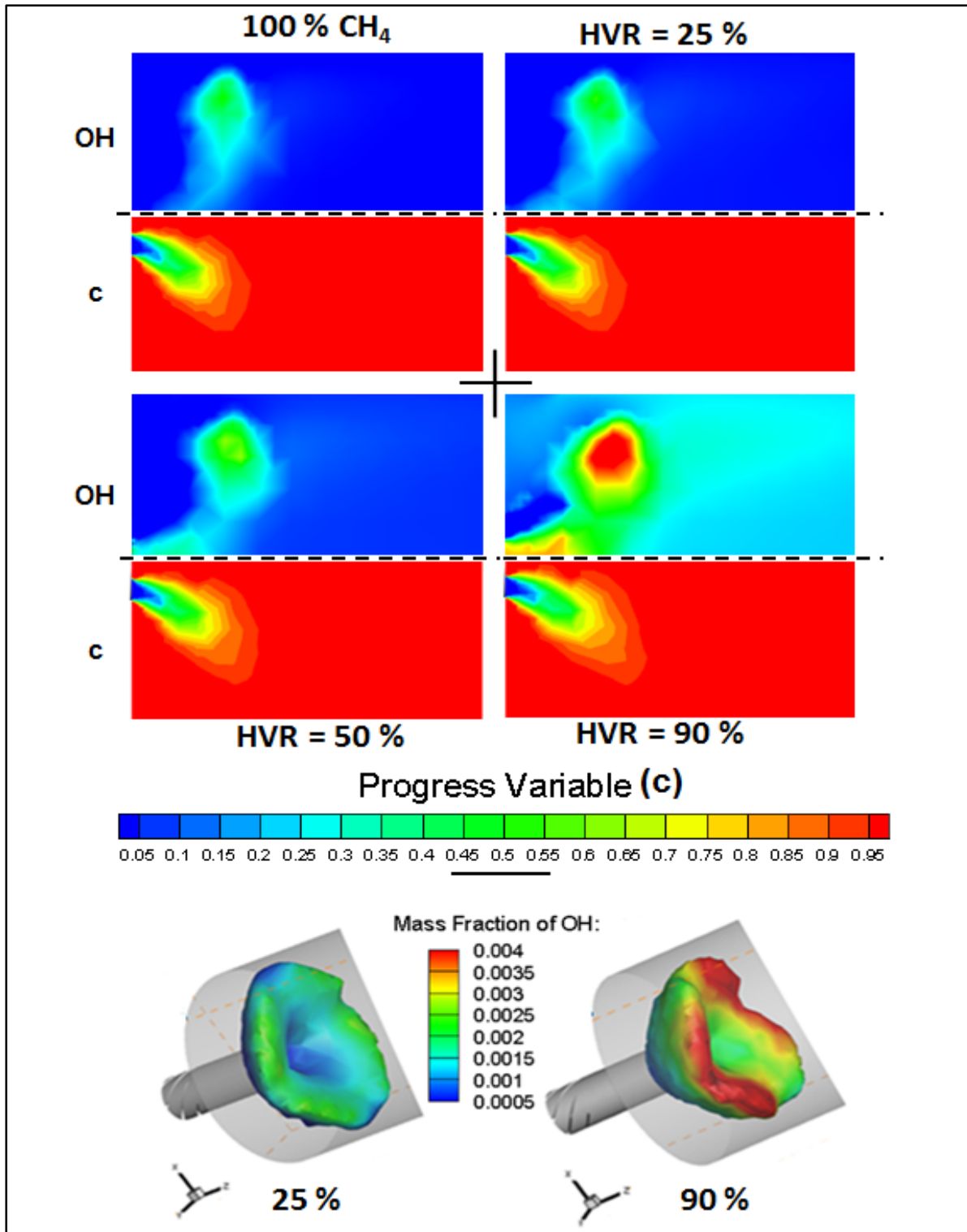


Figure 4.6 2D flame visualization inside the ROI using OH radical (up) and c (down) at $\phi = 0.7$ for CH_4 (top left) and HEC with HVR = 25% (top right), 50% (bottom left), and 90% (bottom right) with a 3D visualization of HVR = 25% (base left) and 90% (base right)

4.2.4 H₂ addition effect on the main species concentrations (CH₄, H₂, O₂, CO₂, CO, and H₂O)

The effect of hydrogen addition to methane on the main species concentrations is now identified by comparing the lowest (25%) and highest (90%) studied H₂ concentrations under lean and stoichiometric burning conditions.

Figure 4.7 shows the distribution of CH₄ (top left), H₂ (top right), O₂ (middle left), CO₂ (middle right), H₂O (bottom left), and CO (bottom right) inside the ROI. It can be seen that, increasing HVR from 25 % to 90 % increases H₂O and decreases CO₂, as expected, due to the formation of more water as a logical consequence of H₂ oxidation. Moreover, the HVR increase enlarges the oxygen concentration ($Y_{O_2} = 0.06$) in the flame front, due to the flame stretch identified earlier. Last, H₂ reduces CO in the flame front and everywhere inside the ROI, similarly to Hawkes & Chen (2004); Schefer (2003). This CO reduction is attributable to the increased OH radical, which promotes the conversion of CO into CO₂, according to equation (4.1), as well as to the increased temperature (that will be shown next) associated with HVR increase, which allows the complete oxidation of CO into CO₂.



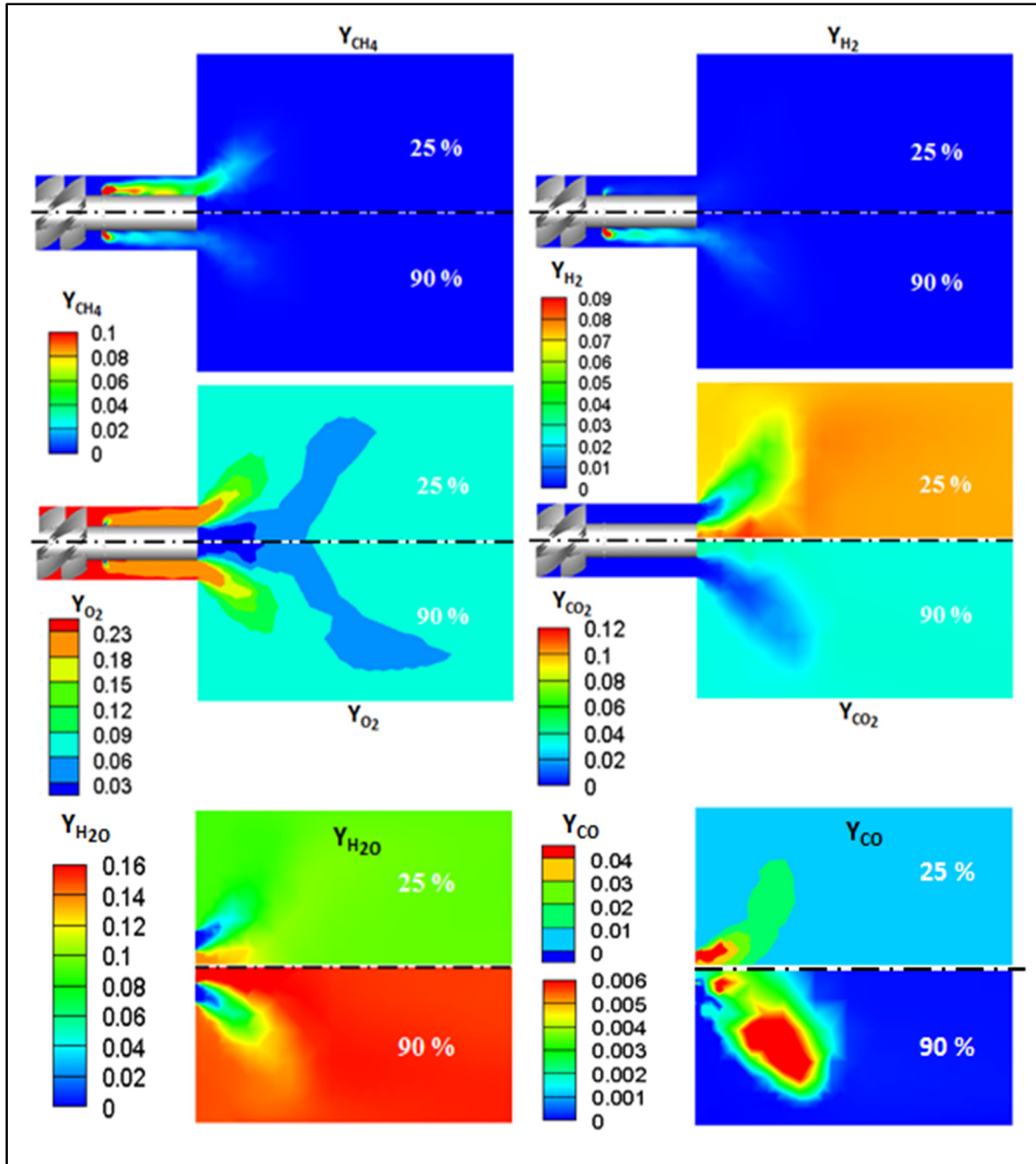


Figure 4.7 Mass fractions of CH₄ (top left), H₂ (top right), O₂ (middle left), CO₂ (middle right), H₂O (bottom left), and CO (bottom right) for HEC at $\phi = 0.7$ with HVR = 25% (up) and 90% (down)

4.2.5 H₂ addition effect on the burnt temperature (with radiation)

The analysis now proceeds with the burnt temperature, when heat transferred by radiation is considered. Figure 4.8 shows the 2D burnt temperature (considering heat loss radiation) contours inside 2/3 the chamber length at $\phi = 0.7$ for CH₄ flame (top left) and HEC with HVR = 25% (top right), 50% (bottom left), and 90% (bottom right). It can be seen that increasing HVR from 0 to 90 % increases the maximum CFD-predicted temperature (in the wake region), flame temperature, and post-flame temperature from ≈ 2228 , 1900, and 1800 K to ≈ 2346 , 2000, and 1900 K, respectively. In addition, the corners temperature increased from $\approx 1600 - 1700$ K (for CH₄) to $\approx 1800 - 1900$ K, for HEC with HVR = 90%.

It can be also observed that increasing HVR from 0 to 25 and 50% gradually enlarges the area with $T = 1900$ K, which covers the entire studied combustion chamber length for HEC with HVR = 50%. Moreover, the area with $T = 2000$ K for the highest studied HVR (90%) is larger than the area with $T = 1900$ K for HEC with HVR = 25%. Such variations indicate the flame stretch with an H₂ addition increase, which was identified earlier in terms of the OH radical and progress variable in section 4.2.3.

Regarding the temperature of the corners and shear layers, it is noted that increasing HVR increases the corners temperature. As well, the flame is always attached or hung on the bluff body and extended to the ROI with relatively cooler corners. Lastly, the shear layers temperature remains cold at the entry and then increases smoothly.

Generally, hydrogen has the impact of increasing the temperature inside the combustion chamber. This temperature increase is due to the increased total energy liberated with an increased H₂ addition (as shown before in section 4.2.1) in combination with the role of hydrogen in decreasing the IRZ size, which was also identified earlier in section 4.2.2.

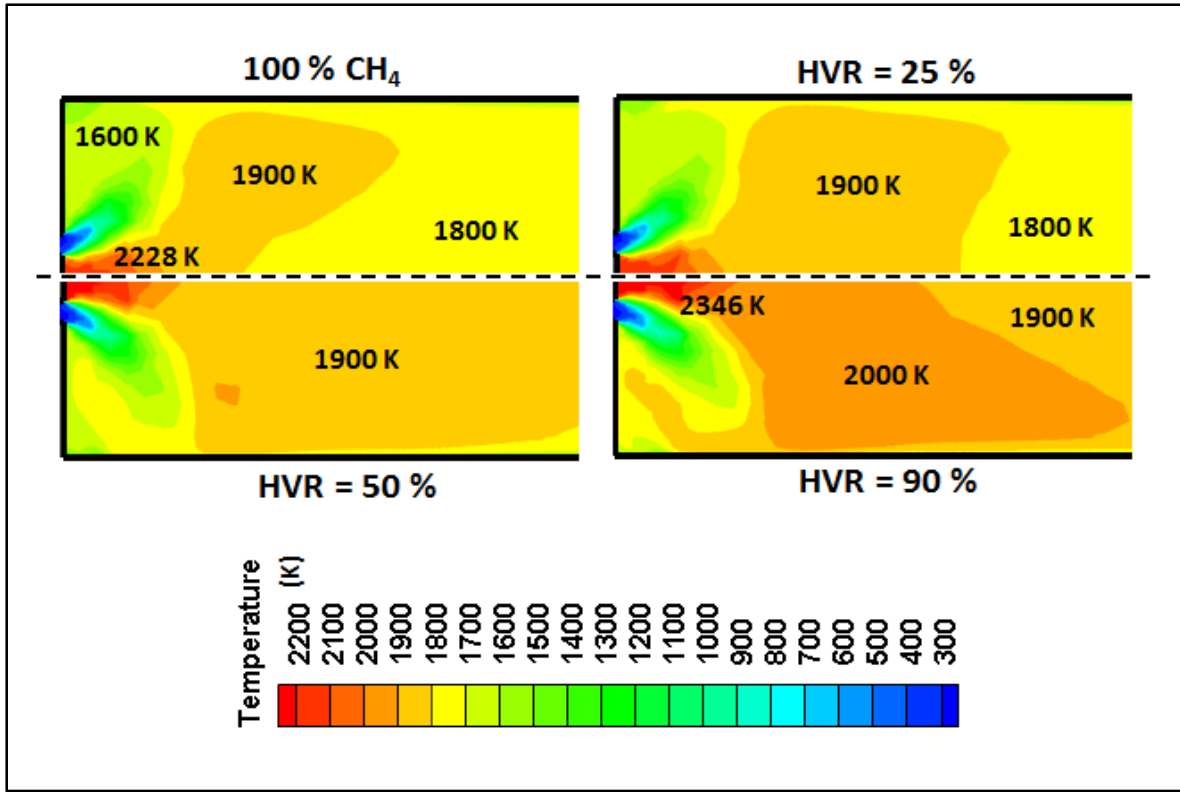


Figure 4.8 2D temperature distribution inside $2/3 L_{cc}$ at $\phi = 0.7$ for methane (top left) and HEC with HVR = 25% (top right), 50% (bottom left), and 90% (bottom right)

4.2.6 H₂ addition effect on NO_x emissions

The last parameter to be studied in this study is NO_x emission. Since radiation heat loss impacts temperature, which in turn will determine the NO_x emissions levels, simulations are run with and without considering heat loss by radiation for CH₄-air combustion and HEC (with H₂ concentrations up to 90%) at $\phi = 0.7$.

Figure 4.9 shows the temperature (top) and NO_x (bottom) plots extracted along the burner's longitudinal axis at $\phi = 0.7$ for methane flame and HEC with HVRs up to 90%. It can be seen that NO_x trends always follow the temperature and the higher temperature - with higher HVR - results in higher NO_x, similarly to data reported by Kim *et al.* (2009 a); Kim *et al.* (2009 b). Moreover, all profiles reach the outlet temperature near $Z/D = 2$. Last, the highest NO_x levels are identified in the wake region, i.e. at the combustion chamber entry ($Z/D \leq 1$), where fuel-

air mixture is always rich. The same conclusion was reported by Taupin (2003) and previously identified through the experiments of Schefer *et al.* (2002); Novosselov *et al.* (2006), due to the identified fuel-air mixture inhomogeneity at the LP combustors entry.

A 2D visualization of NO_x inside the entire combustion chamber at $\phi = 0.7$ is presented in Figure 4.10 for methane flame (top) and HEC with HVR = 25% (middle) and 90% (bottom). It is observed that for HEC with HVR = 25% (middle), the zone of the highest NO_x levels increases versus methane (top). However, the NO_x level at the burner's outlet remains near 2 ppm. Adding 90% of H_2 shows that nearly the entire combustion chamber volume is occupied by a high NO_x level of ≈ 10 ppm.

For further analysis, NO_x levels as well as the temperature are reported versus the HVR at the burner's outlet in Table 4.1, with and without considering heat loss by radiation. It is observed that increasing HVR up to 90% translated in an increase of the outlet temperature by ≈ 115 K, irrespectively of whether or not the calculations consider radiation heat loss. However, the net consequence of considering heat loss by radiation is a decrease of the outlet temperature by ≈ 110 K, which is translated into a reduction of the outlet NO_x by half. For HEC with HVR up to 50% and for lean combustion, the consequence of increasing H_2 concentration on NO_x emission is low as NO_x levels are generally in the order of a few ppm. Such a slight increase can be considered to be practically insignificant, as long as the outlet NO_x levels are generally low, similarly to Schefer (2003); Hawkes & Chen (2004). However, at high concentrations (75 and 90%) and as the equivalence ratio approaches stoichiometric conditions, radiation heat loss will play an important role in the predictions of NO_x emissions, due to the higher temperature involved.

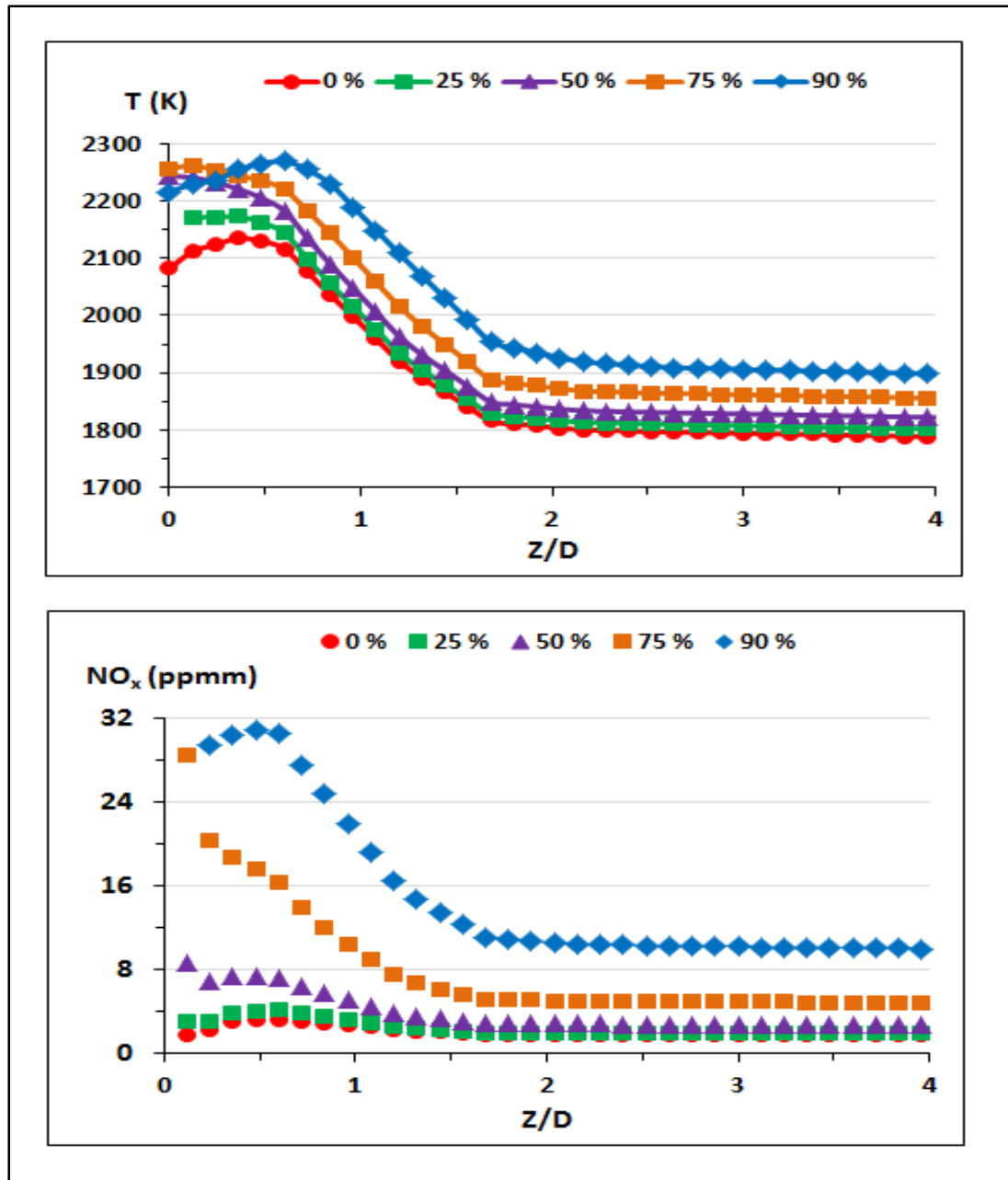


Figure 4.9 Plots of temperature (top) and NO_x (bottom) along the burner's longitudinal axis at $\phi = 0.7$ for methane and HEC with different HVRs: 25, 50, 75, and 90%

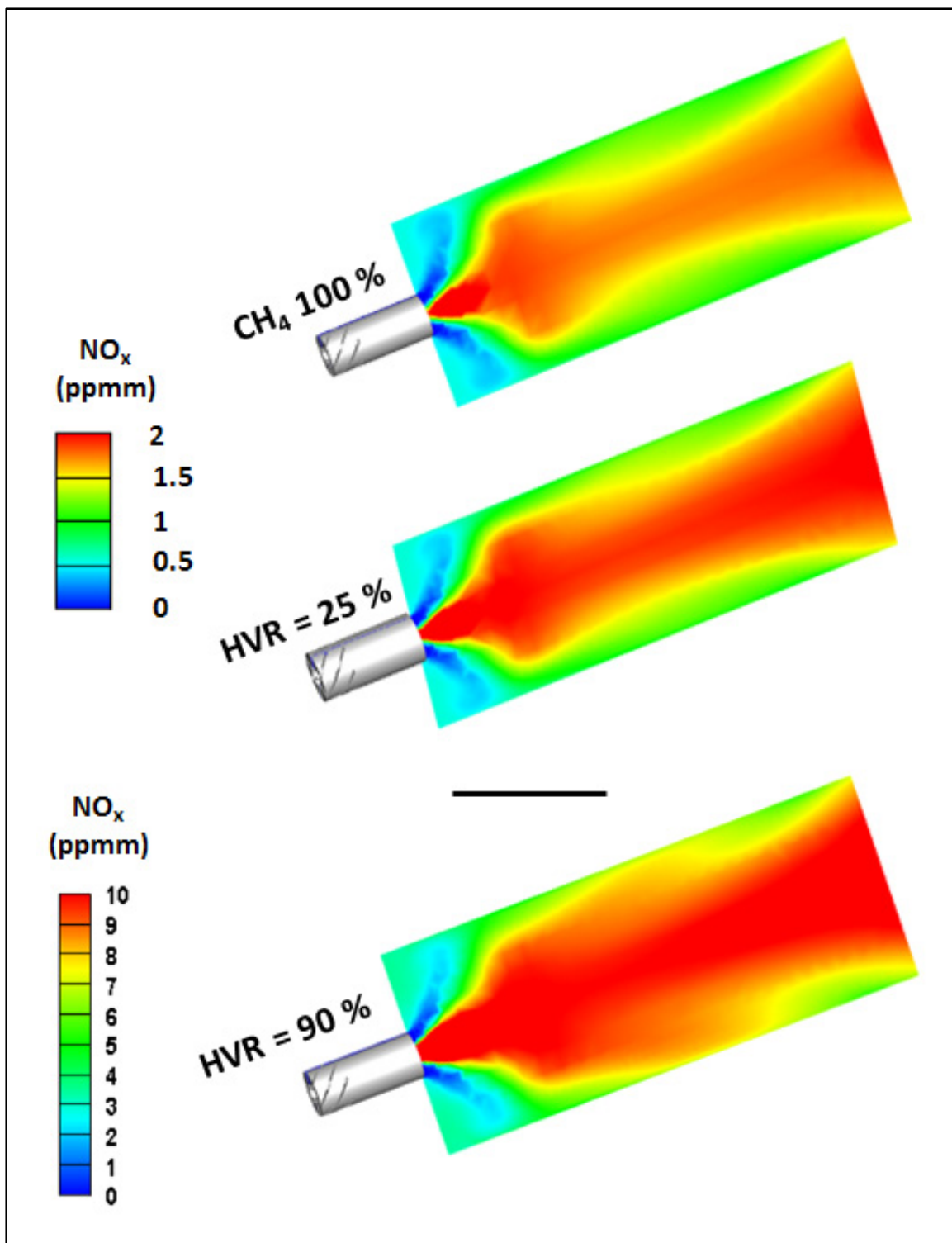


Figure 4.10 2D NO_x distribution inside the entire combustion chamber at $\phi = 0.7$ for methane (top) and HEC with HVR = 25% (middle) and 90% (bottom)

Table 4.1 Temperature and NO_x at the burner's outlet versus HVR, case $\phi = 0.7$

HVR (%)	With radiation		Adiabatic	
	T _{outlet} (K)	NO _x (ppmm)	T _{outlet} (K)	NO _x (ppmm)
0	1725	2	1836	4
25	1747	3	1852	5
50	1775	4	1875	7
75	1800	6	1913	13
90	1840	11	1958	28

Similar trends, but higher temperature and NO_x levels are observed when the equivalence ratio increases to 1, while the opposite is true if the equivalence ratio is decreased.

Since the GRI 3.0 detailed mechanism has been used to define the detailed chemistry (including the NO_x chemistry) and considering the fact that NO_x emissions form through different pathways. It is instructive herein to identify the effect of hydrogen on the trends of some of these species, such as an NNH route, which depends on the presence of H atom and OH radical (Ayoub, Rottier, Carpentier, Villermaux, Boukhalfaa, & Honoré, 2012).

Figure 4.11 shows the 2D distributions of temperature (top left), NO (top right), NNH (bottom right), and NO₂ (bottom left) inside the ROI for CH₄-air combustion at $\phi = 0.7$, while Figure 4.12 and Figure 4.13 show the same parameters distributions at the same equivalence ratio, but for HEC with HVR = 25 and 90%, respectively. Comparing the three figures, it can be seen that increasing HVR increases the temperature, leading to a decrease in NO₂ production, but an increase in the NO species. Moreover, increasing HVR increases the NNH concentration, which strongly depends on the H, O, and OH radicals, as per equations (4.2) to (4.9) that represent the formation and destruction of NNH species. Therefore, NNH is rapidly formed in the flame and increases with respect to the HVR increase.





It can be also seen that NO is formed in the high temperature region after the flame, through the Zeldovich mechanism. Moreover, NO is considered predominant with respect to NO₂, which is formed in the flame through the presence of carbon atom and is favored by low flame temperatures (below 1500 K) (Kim *et al.*, 2009 b). Otherwise, NO₂ is converted back to NO at high temperature.

Based on the results, it can be confirmed that the NNH route does not contribute significantly to the production of NO and can thus be ignored. This conclusion is made based on the fact that NNH concentration is 6 times lower than the NO obtained at the outlet of the combustion chamber. Thus, NNH associated chemistry is not necessary for the conditions tested herein.

Similar trends but different levels were identified for the NO, NO₂, and NNH species concentrations under stoichiometric burning conditions, with HVRs up to 60%. Results are not shown in order to shorten the dissertation.

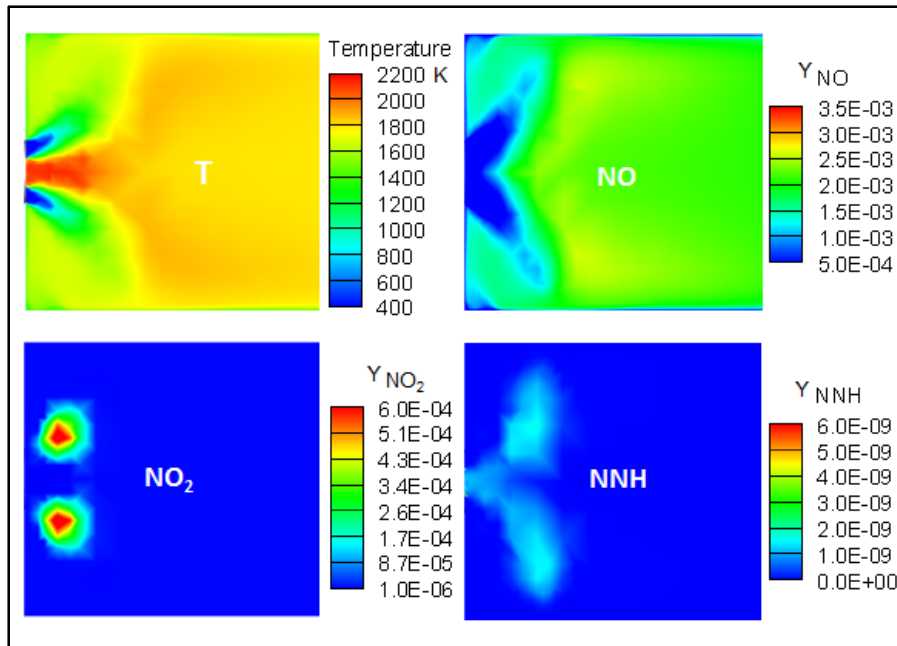


Figure 4.11 2D distributions of temperature, NO, NNH, and NO₂ (stacked clockwise) inside the ROI for methane flame at $\phi = 0.7$

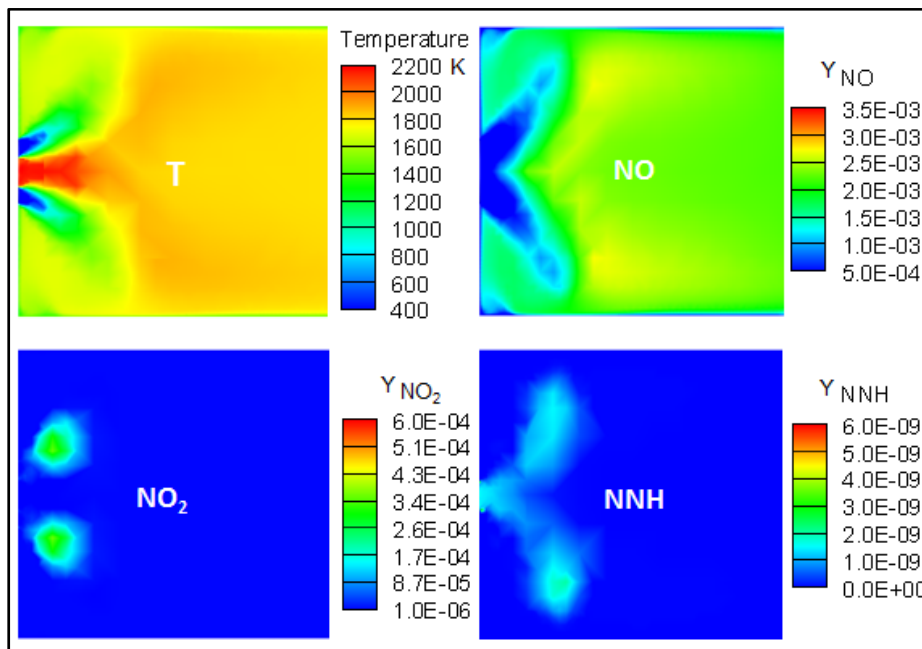


Figure 4.12 2D distributions of temperature, NO, NNH, and NO₂ (stacked clockwise) inside the ROI for HEC with 25% H₂ at $\phi = 0.7$

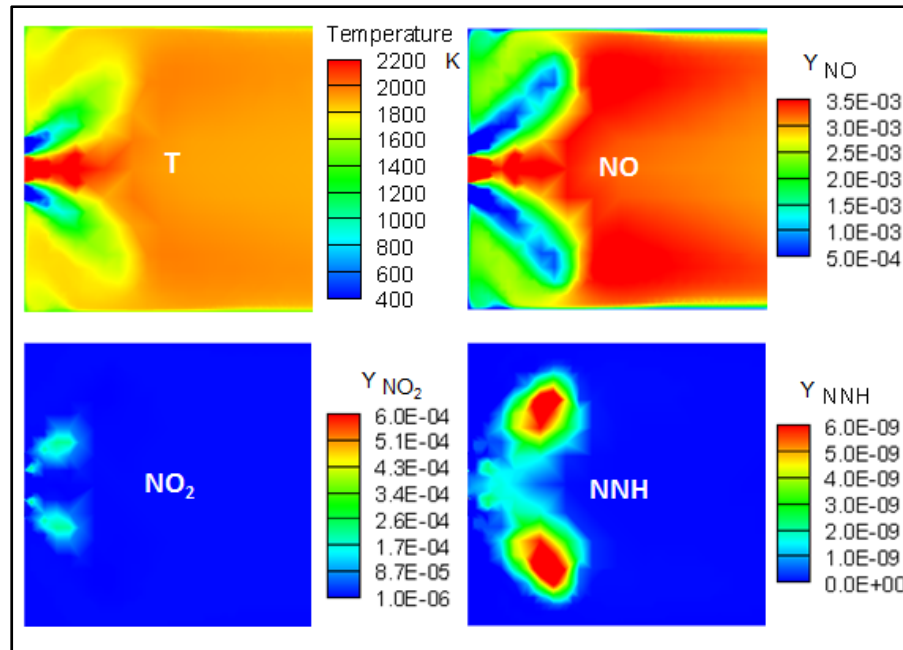


Figure 4.13 2D distributions of temperature, NO, NNH, and NO₂ (stacked clockwise) inside the ROI for HEC with 90% H₂ at $\phi = 0.7$

4.3 Chapter discussion and conclusions

This discussion presents the real burner (Microturbo Saphir 150) that has been modeled in this dissertation and tested before by Taupin (2003), considering the “Institut National des Sciences Appliquées de Rouen” laboratory restrictions of 215 g/s for the air mass flow rate. This burner was designed for electrical energy production. Based on these lab restrictions, a test rig was established (by INSA, CORIA Rouen) and it was decided to test 1/7 the power of the real burner. Another restriction was then imposed, as the maximum injection velocity of air was limited to 30 m/s. Table 4.2 includes the operating conditions (air and fuel mass flow rates and air injecting velocity) of the real burner, lab burner, and restricted-lab scale burner, involving the power of each configuration as well as the modeled power proportions.

Table 4.2 Power scaling and inlet conditions for the real burner, lab burner, and restricted lab-scale burner

Parameter	Real burner	Lab burner	Restricted-lab scale burner (modeled herein)
Power (kW)	1228 (1MW)	179	10
V_{in} (m/s)	98	98	30
m_a (g/s)	1245	43	8
m_f (g/s) $\phi = 0.7$	12.2	1.74	0.325
Power proportion	\uparrow 1/7 14%		\uparrow 1/20 5%
	1%		

The analysis presented in Table 4.2 indicates that the modeled power herein represent 1% (10 kW) of the real burner's power. Hence, very low levels of NO_x are expected. This power analysis explains the low NO_x levels (≈ 2 ppm) identified herein for the methane-air combustion at $\phi = 0.7$, which is also comparable to Kim *et al.* (2009 a) and Kim *et al.* (2009 b), who reported similar low NO_x levels for a similar lab scale combustor with 5.81 kW power.

The same power analysis highlights the importance of considering inlet conditions approaching the real GTE operating conditions, when conducting numerical modelling or even when being restricted to some experimental constraints. For instance, considering an inlet velocity of 30 m/s herein (instead of the real one, 98 m/s) keeps the turbulence level as high as in the real conditions, where the flame remains characterized by a high fluctuation velocity ($u' \approx 10$ m/s) that could reach up to 45 times the laminar burning velocity ($S_L \approx 22$ cm/s at $\phi = 0.65$). On the other hand, some studies in the literature neglected turbulence and considered lower inlet velocities, such as that by Nemitallah *et al.* (2019), who studied HEC at an inlet velocity of 5 m/s, which resulted in wrinkled flames that were governed by chemical kinetics.

Another difference this discussion presents is the phenomenological HEC study concept, based on the study approach - either experimental or numerical - and the consequence on the combustion characteristics. Table 4.3 summarizes the distinctions of concept and consequences, when HEC is studied experimentally or numerically.

Table 4.3 Hydrogen addition phenomenological concept according to the study approach

Experimentally	Numerically
Occurs at a constant heat load	Assumes a constant equivalence ratio
Results in an overall leaner mixture	Results in more heat release as equivalence ratio is kept fixed
Hence, lower AFT is reported	Hence, higher AFT is predicted

Table 4.3 explains the contradiction of results presented herein with Kim *et al.* (2009 a) and Kim *et al.* (2009 b) with respect to the effect of hydrogen addition to methane on AFT as well as the effect of swirl intensity on the flame shape and length. For instance, hydrogen addition was reported by Kim *et al.* (2009 a) and Kim *et al.*, (2009 b) to decrease the equivalence ratio from 0.717 to 0.706 and 0.694 when hydrogen increased from 0 to 4 and 9 %, respectively, while on the contrary, the equivalence ratio has been kept fixed (at 0.7) in this dissertation, considering the case of the lean HEC. As a result, AFT was reduced by ≈ 3.5 °C for each hydrogen ratio increase at a fixed heat load (5.81 kW), according to Kim *et al.* (2009 a) and Kim *et al.* (2009 b), whereas AFT and HRR were increased herein with an HVR increase. This opposition also illustrates the difference between the effect of hydrogen addition on NO_x emissions reported by studies in the literature, some of which report that hydrogen addition might increase the NO_x emissions due to the higher flame temperature at a constant heat load, while others report an overall leaner mixture with hydrogen addition to methane. These studies include Hawkes & Chen (2004), Kim *et al.* (2009 a), and Kim *et al.* (2009 b).

The goal of this chapter was to identify the effect of hydrogen addition to methane on the flame structure and emissions under lean and stoichiometric burning conditions. First, the

combustor reactive flow model was modified in order to account for hydrogen addition. Then, the effect of hydrogen addition on AFT, total energy, combustion diffusivity, flow field, vorticity, main species concentrations, flame shape and temperature, and emissions was identified for a fixed swirl condition of $S = 0.9$ ($\alpha = 50^\circ$).

It was found that hydrogen has the following effects: it increases AFT, total energy, and combustion diffusivity, decreases the IRZ size and shifts its location in the far stream flow, increases the vorticity level inside the wake region, increases the OH radical and results in longer flames, raises the reaction zone temperature and hence increases the NO_x levels at the combustion chamber entry. Such an increase of NO_x was considered insignificant (for moderate hydrogen concentrations) as long as NO_x levels were generally in the order of a few ppm at the burner's outlet. Hydrogen was found responsible for reducing CO emissions as it helps CO conversion into CO_2 , which was also reduced with a hydrogen increase.

Finally, it is noteworthy that the irregularity of the flow pattern and temperature distribution identified for the stoichiometric HEC with high hydrogen concentrations (HVR = 75 and 90%) triggered a study of HEC at higher swirl levels, which will be presented in the next chapter.

CHAPTER 5

SWIRL INTENSITY

Following chapter 4, the effect of swirl intensity on the main flame characteristics and emissions will be studied in this chapter, which will allow to reach the third research sub-objective (A3). A partial modification of the combustor - by varying the swirl vanes angle - is thus applied and then numerically tested for methane-air combustion and HEC.

5.1 CFD model geometry modification with respect to swirl intensity

The combustor numerical model is modified in order to account for the change of swirl intensity, S , by changing the swirl vanes angle, α , as seen per Figure 5.1. Based on this angle, a swirl number, S , could be defined according to Equation (5.1), rewritten below, where a is the ratio of the bluff body to the swirler diameters.

$$S = \frac{2(1-a^3)}{3(1-a^2)} \tan(\alpha) \quad (5.1)$$

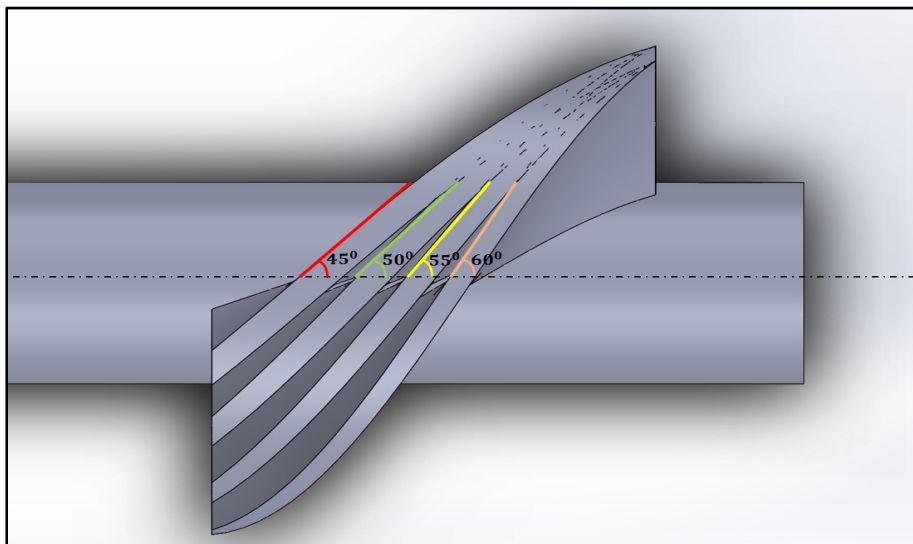


Figure 5.1 Combustor model geometry modification with respect to the swirl intensity in terms of the swirl angle (α)

Table 5.1 shows the resulting swirl intensity/number (indicating the ratio of the axial flux of tangential velocity to the axial flux of axial velocity) for each swirl angle, where S varies between 0.64 (for the smallest swirl vanes angle, 40°) to 1.3 (for the highest swirl angle, 60°).

Table 5.1 Swirl intensity change with respect to swirl vanes angle

Swirl angle (α)	Swirl intensity/number (S)
40°	0.64
42°	0.68
45°	0.76
50°	0.90
52°	0.97
55°	1.08
60°	1.30

5.2 Cold and reactive flow analyses for different swirl angles

The wide range of swirl angles presented in Table 5.1 is numerically studied in terms of the cold flow and reactive flows properties and the same conclusion of Taupin (2003) and Taupin *et al.* (2007) is reached for the swirl configurations lower than 50° (40° , 42° , and 45°). Such configurations couldn't sustain a stable flame, for either pure methane or H_2 -enriched methane combustion. Neither IRZ nor reversed flow regions are formed (for reactive flow) in addition to an irregular temperature distribution is observed inside the ROI. Hence, these configurations are eliminated from the analysis and results are not presented. On the other hand, the swirl configurations higher than 50° (52° , 55° , and 60°) showed favourable results, which will be presented next.

5.2.1 Cold flow analysis

In this section, the 52°, 55°, and 60° swirl configurations are studied from the cold flow perspective. Figure 5.2 shows the distribution of the axial velocity inside the ROI for the 52°, 55°, and 60° swirl configurations, from top to bottom, respectively. It is noted that all swirl configurations show a cold flow pattern characterized by the IRZ, two CRZs, and shear layers. Moreover, increasing the swirl vanes angle from 52° (top) to 55° (middle) and 60° (bottom) gradually increases the size of the iso-surface $u = -5$ m/s. Such a conclusion indicates that increasing the swirl vanes angle increases the IRZ size.

In order to scrutinize the flow pattern and identify distinctions between the studied configurations, the 2D velocity vectors (coloured by the axial velocity) are compared in Figure 5.3 for two swirl configurations, namely, the basic swirl configuration (50°) that has been validated before in Chapter 3 (and where HEC has been studied in Chapter 4) and the highest swirl configuration, 60°. It can be seen that the 50° swirl configuration shows a wider CRZ, which closes at 30 mm, similarly to Taupin (2003). On the other hand, the 60° swirl configuration shows a shorter CRZ that closes before 26 mm. The same effect was reported by Kim *et al.* (2009 a), when the swirl vanes angle increased from 30° to 45° and 60° as well as by Huang & Yang (2005), when the swirl intensity increased from 0.44 to 1.1.

Figure 5.3 also indicates that the 60° swirl configuration shows a larger area with the highest negative axial velocity ($u = -10$ m/s) inside the wake region just behind the bluff body, indicated by the dashed box. Such a conclusion indicates that increasing the swirl vanes angle increases the IRZ size, as indicated above.

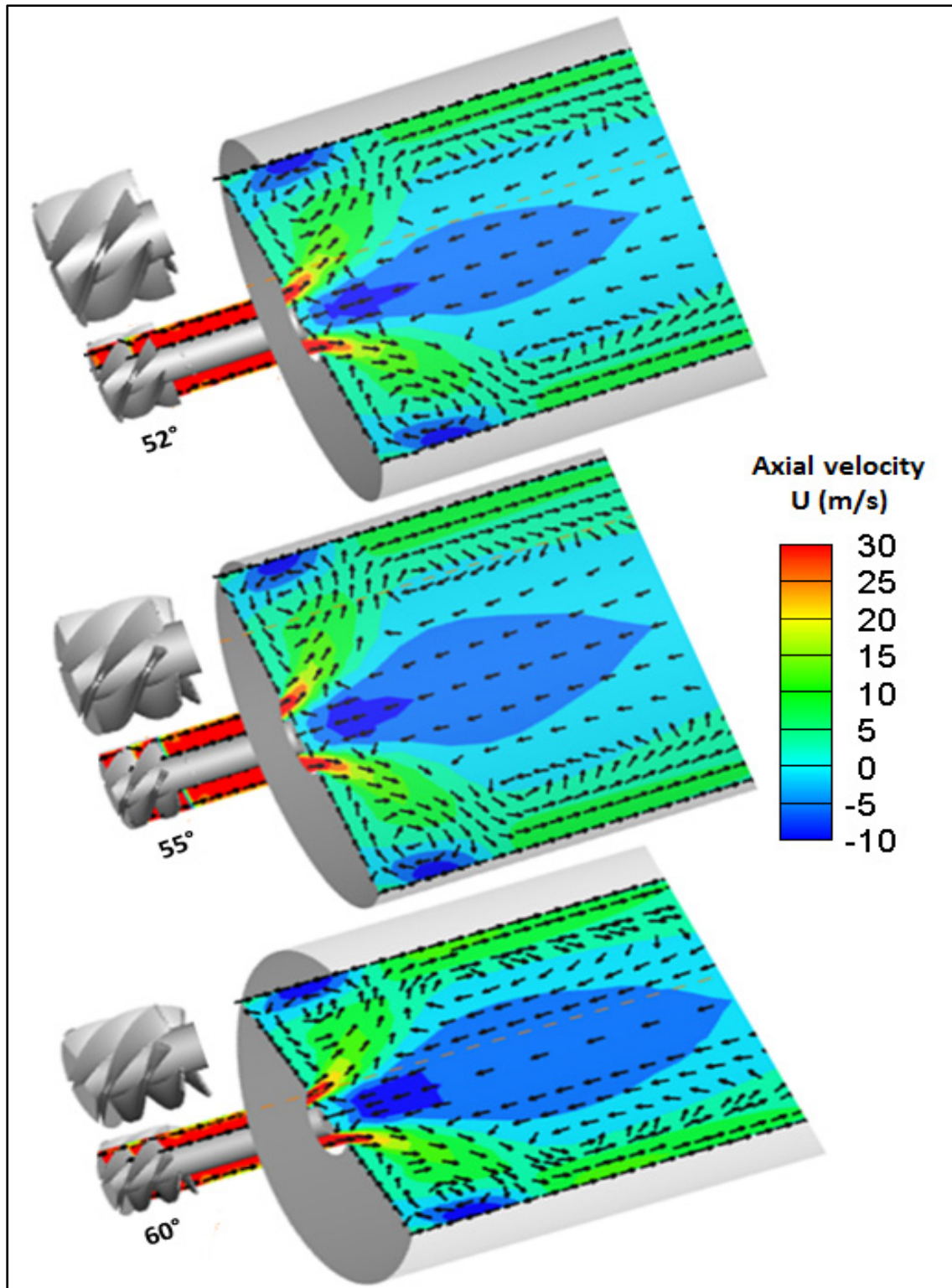


Figure 5.2 Cold flow analysis in terms of the axial velocity distribution inside the ROI for the 52°, 55°, and 60° swirl configurations, from top to bottom, respectively

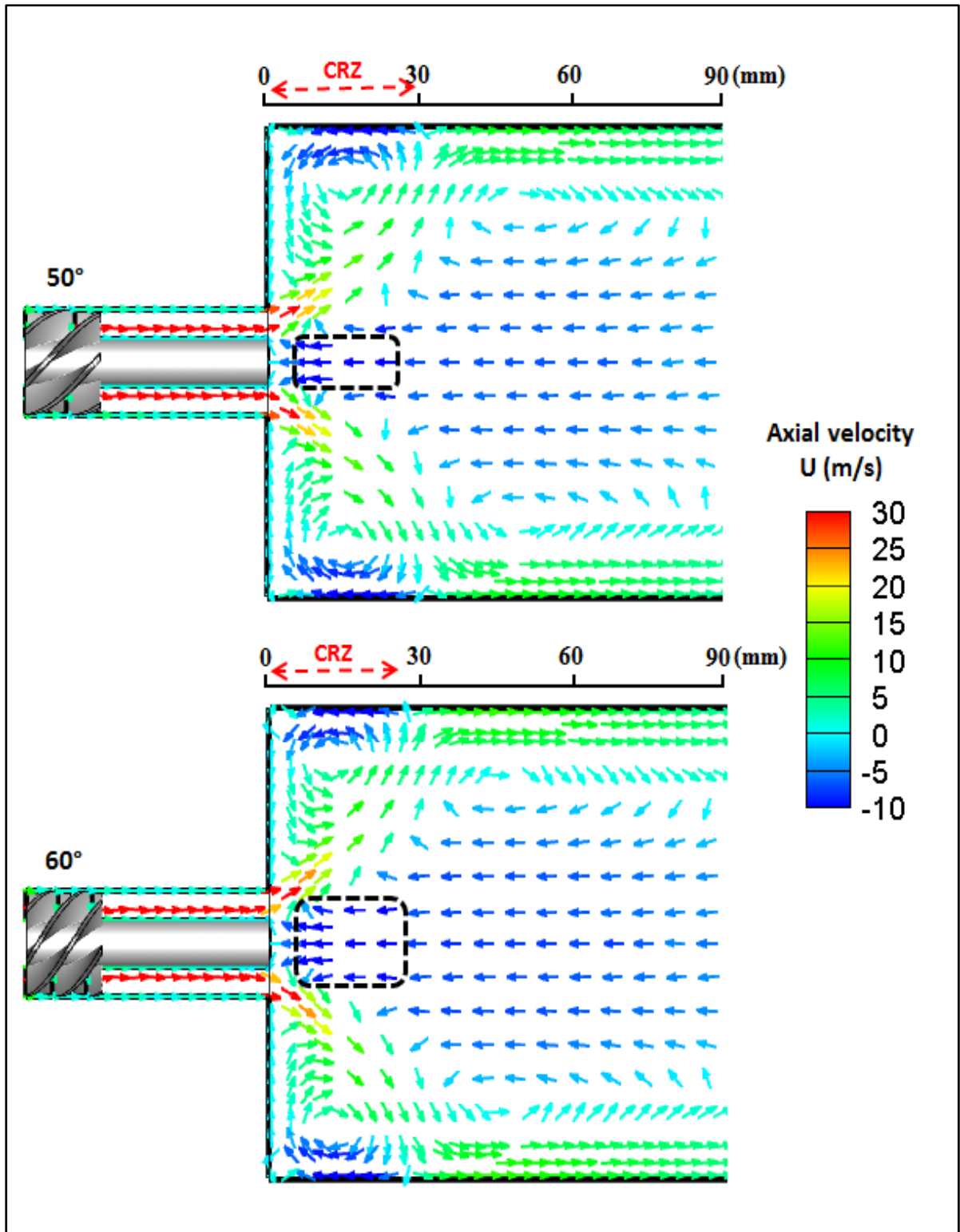


Figure 5.3 Cold flow analysis in terms of the 2D velocity vectors (coloured by u) distribution inside the ROI for the basic (50°, top) and highest (60°, bottom) swirl configurations

5.2.2 Reactive flow analysis (CH₄-air combustion at $\phi = 0.7$)

Following the cold flow analysis, the effect of swirl intensity on the main characteristics of CH₄-air combustion at $\phi = 0.7$ is studied and compared with numerical data from Huang et al. (2003) and Huang & Yang (2005). The analysis includes the flow aerodynamics (such as swirling flow velocity components and fluctuation) and chemical data (such as the heat release rate, equivalence ratio, and temperature). Results will be presented by comparing the basic swirl level ($S = 0.9$, $\alpha = 50^\circ$) to the highest one ($S = 1.3$, $\alpha = 60^\circ$), as the 55° results are in between, as expected.

5.2.2.1 Reactive flow aerodynamics

In this section, the 50° and 60° swirl configurations are compared from the aerodynamics perspective. Figure 5.4 shows the 2D streamlines mapped over the axial velocity contours inside the ROI for the reference methane case at $\phi = 0.7$. It can be seen that, first, the centered area with the stagnant flow ($u = 0$ m/s) in light blue (surrounded by a white contour) is shifted into the upstream direction for the 60° swirl configuration. Second, increasing the swirl vanes angle from 50° to 60° increases the size of IRZ. This increase can be identified through the larger region of 60° with the stagnant axial velocity, which is extended till the combustion chamber entry (unlike the 50°), as well as through the enlarged IRZ diameter of the 60° . The IRZ increase is related to the strong pressure gradients in the wake region (Huang et al., 2003), as verified in Figure 5.5, in combination with the increased centrifugal force associated with swirl intensity increase (Kim *et al.*, 2009 a; Gupta, Lilley, & Syred, 1984), as verified in Figure 5.6.

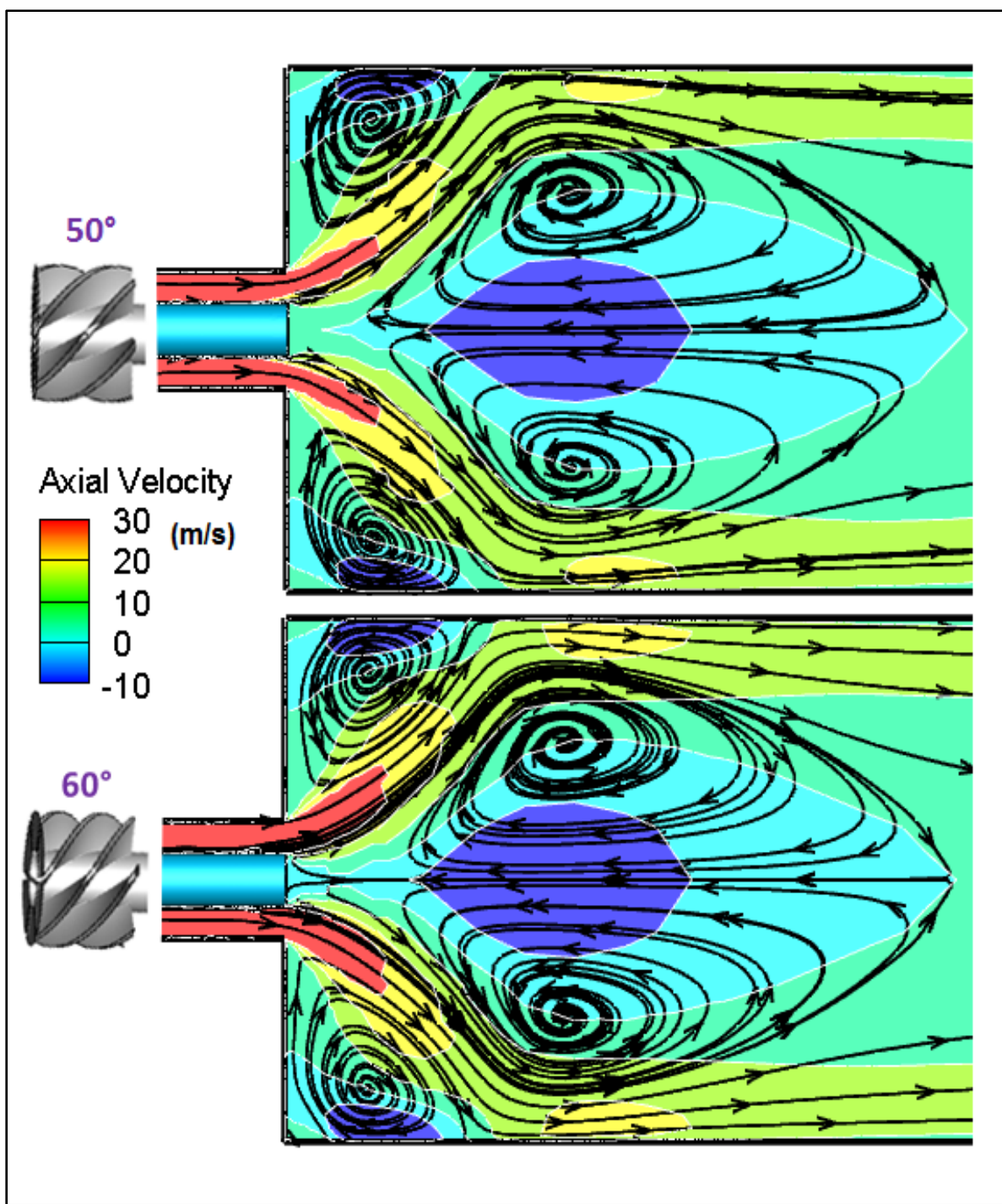


Figure 5.4 Reactive flow analysis using the 2D streamlines (mapped over u) inside the ROI of the 50° (top) and 60° (bottom) swirl configurations for CH₄-air combustion at $\phi = 0.7$

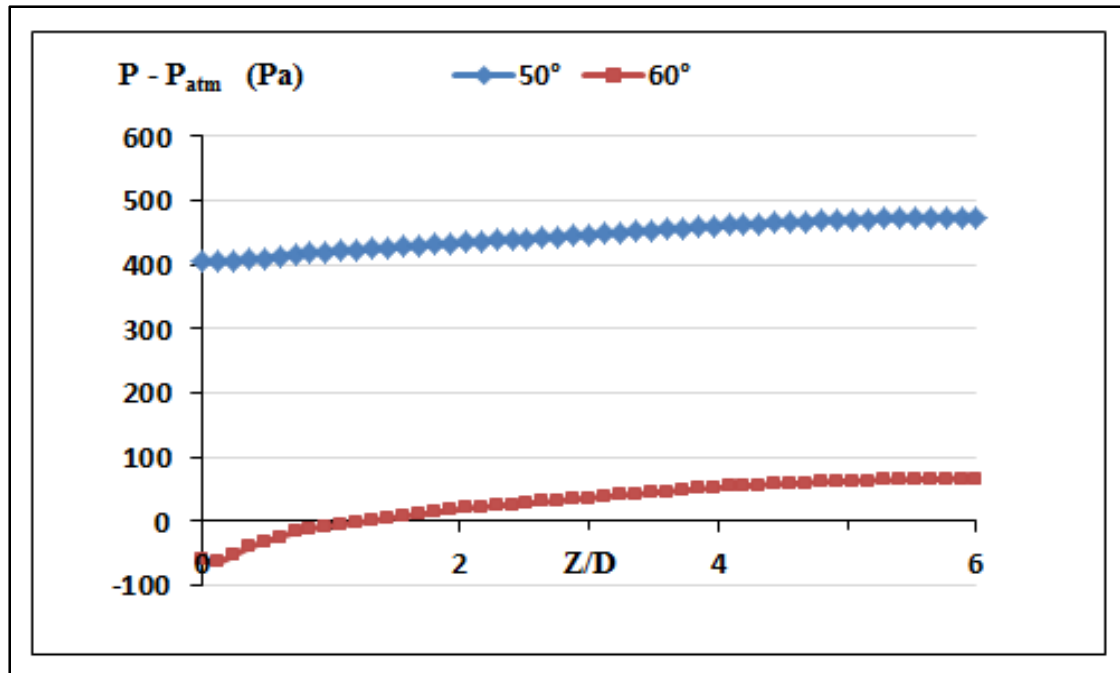


Figure 5.5 Pressure plots along the burner's longitudinal axis for CH₄-air combustion at $\phi = 0.7$ inside the 50° and 60° swirl configurations, where $P_{\text{atm.}} = 101325$ Pa

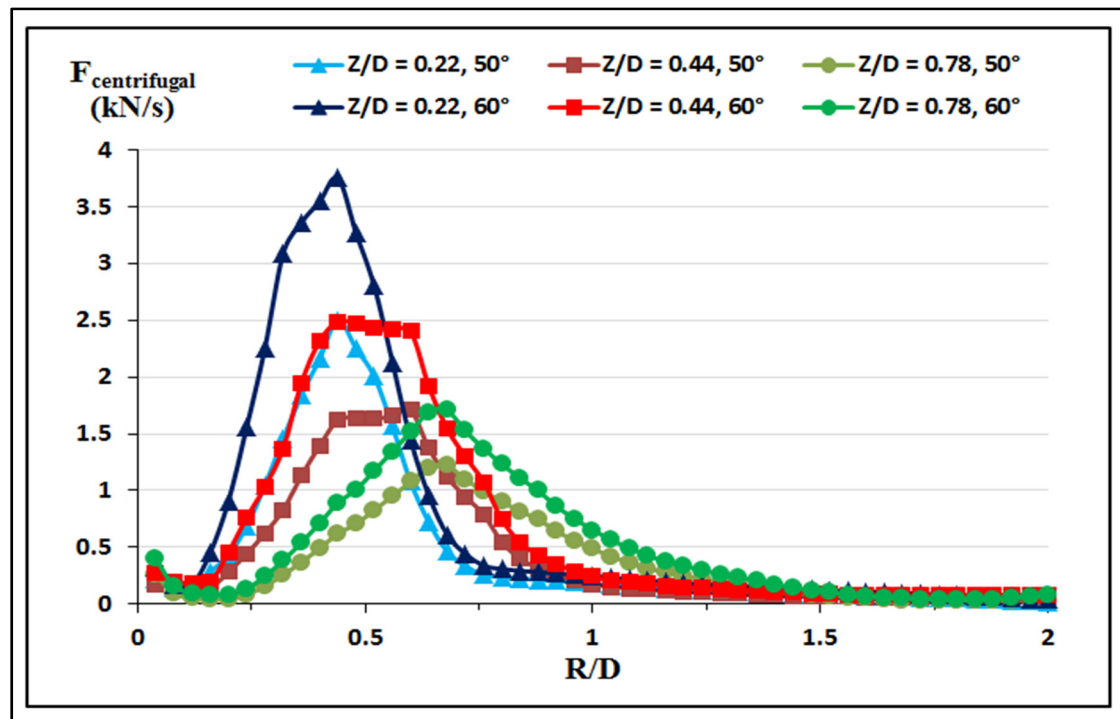


Figure 5.6 Centrifugal force plots versus R/D (at three axial heights) for CH₄-air combustion at $\phi = 0.7$ inside the 50° and 60° swirl configurations

Looking at Figure 5.5, it can be seen that the relative pressure (where $P_{\text{atm}} = 101325 \text{ Pa}$) drops from $\approx [400 - 500] \text{ Pa}$ for the 50° swirl configuration to $\approx [-100 - 100] \text{ Pa}$ for the 60° along the burner's longitudinal axis, which in turn will impact the IRZ flow velocity. On the other hand, by looking at Figure 5.6, it is noticed that the centrifugal force acting on the fluid increases with the swirl angle increase at the three studied axial heights, $Z/D = 0.22, 0.44$, and 0.78 . Such pressure drop and centrifugal force increase result in increasing the IRZ size and strength.

Figure 5.4 also shows that increasing the swirl vanes angle increases the axial velocity of the flow (inside the shear layers in red) entering the combustion chamber, similarly to De & Achary (2012) and Huang & Yang (2005). This increase of the axial velocity is related to the faster expansion of the jet entering from the swirler into the combustion chamber, under the centrifugal force effect, as identified before.

For further analysis, the reference methane case is characterized for both swirl configurations in terms of the total and radial velocities in Figure 5.7 and Figure 5.8, respectively.

Looking at Figure 5.7, it can be observed that the 60° swirl configuration shows a higher total velocity inside the shear layers, which can be identified through the larger regions with the total velocity of 50 m/s (in red) and 40 m/s (in yellow). Moreover, the 60° swirl configuration shows wider regions with the total velocity of 20 m/s inside the wake region and corners. The increased jet velocity of the 60° swirl configuration is attributed to the faster flow entering the combustion chamber from the swirler under the centrifugal force effect with a positive radial velocity in the shear layers, as reported by Huang & Yang (2005), and verified herein in Figure 5.8.

Looking at Figure 5.8, it can be seen that the 60° shows a larger region with the radial velocity of 20 m/s (in red), compared to the 50° swirl configuration. Accordingly, and considering the increase of the inlet jet axial velocity, the total velocity of the entering jet increases with the swirl intensity (angle) increase.

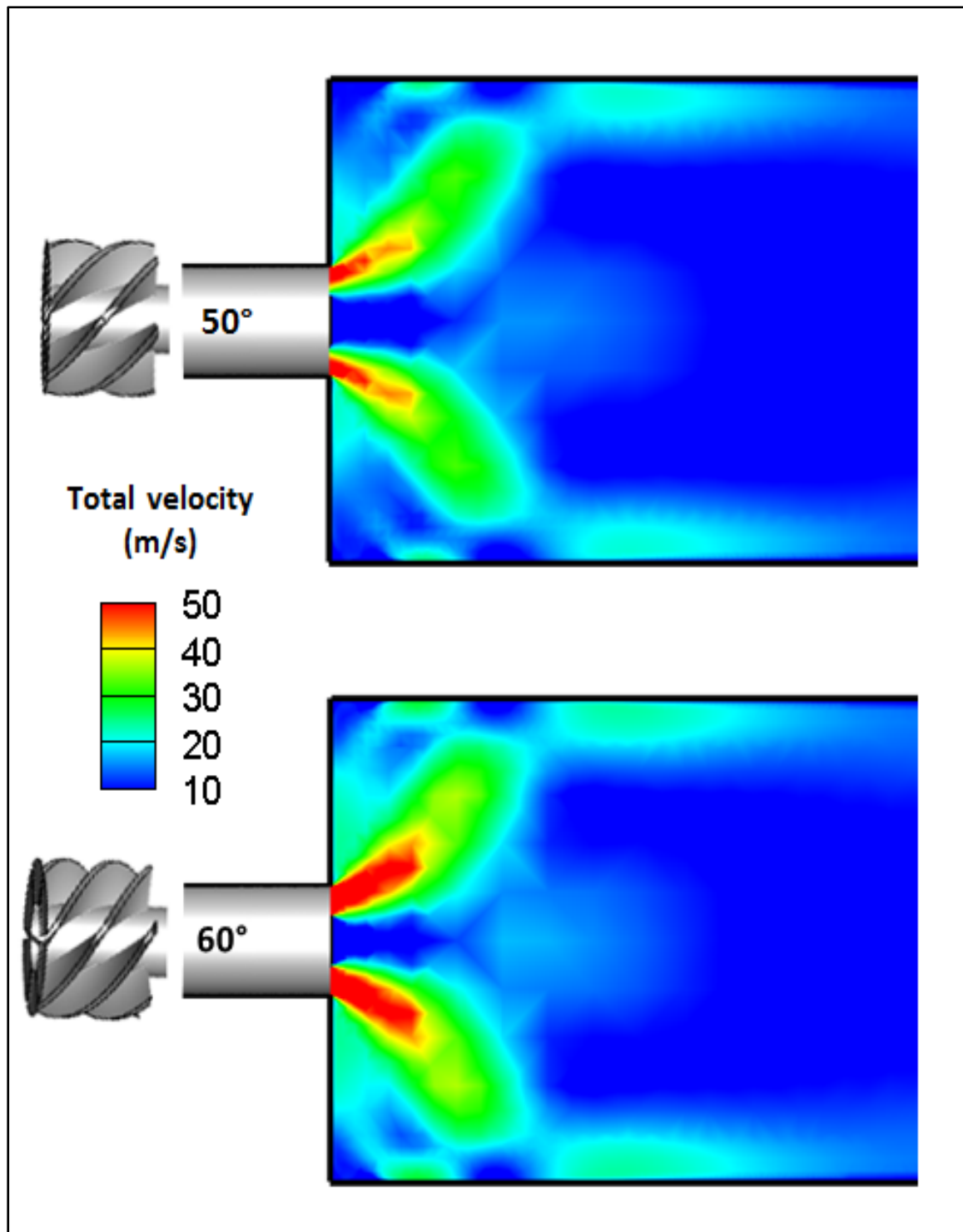


Figure 5.7 Reactive flow analysis using the total velocity distribution inside the ROI of the 50° (top) and 60° (bottom) swirl configurations for CH₄-air combustion at $\phi = 0.7$

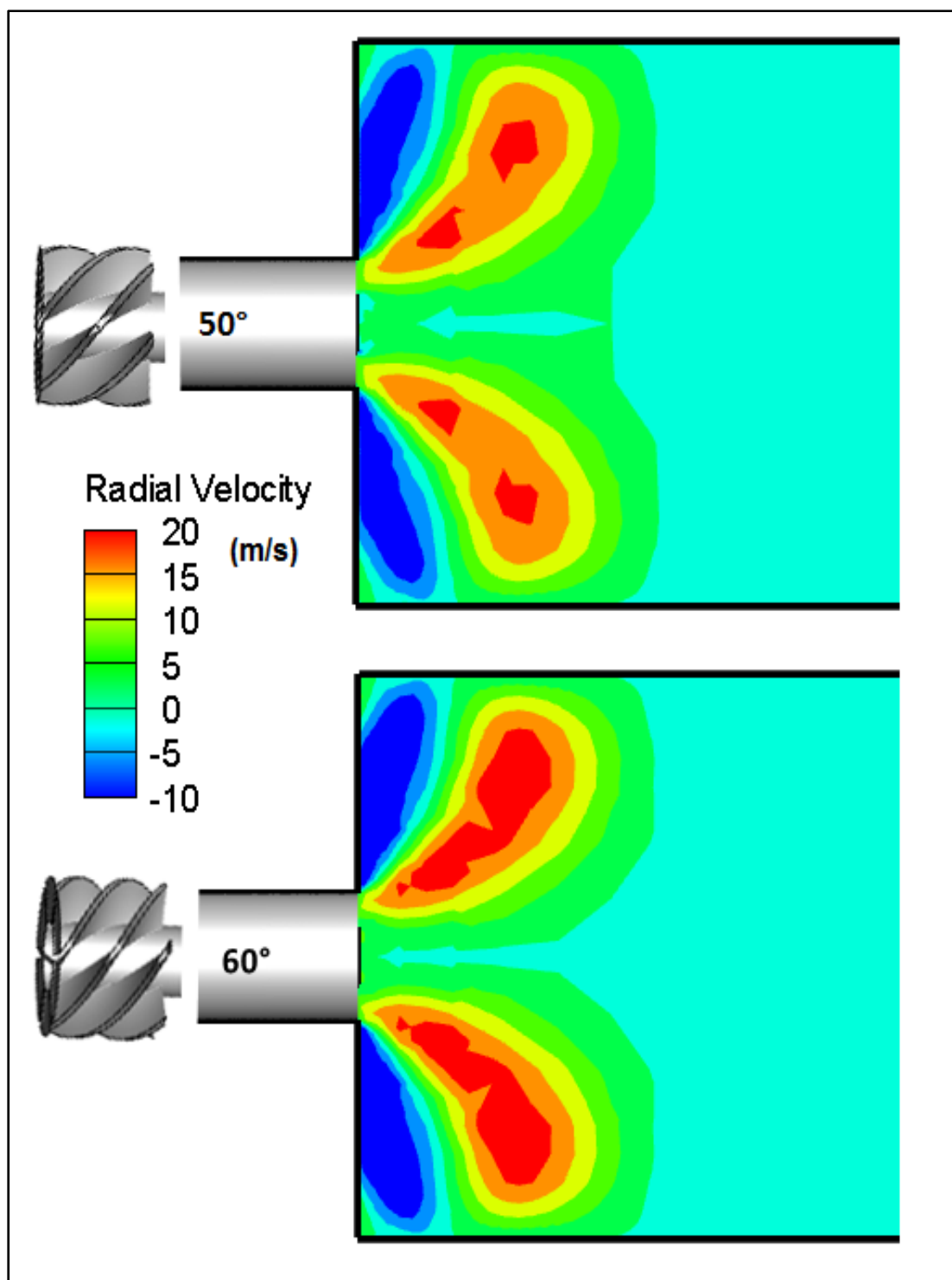


Figure 5.8 Reactive flow analysis using the radial velocity distribution inside the ROI of the 50° (top) and 60° (bottom) swirl configurations for CH₄-air combustion at $\phi = 0.7$

Following the averaged axial, radial, and total velocities, the distribution of the axial velocity fluctuation (\hat{u}) inside the ROI is compared for the 50° (top) and 60° (bottom) swirl configurations in Figure 5.9. It can be seen that the 60° swirl configuration shows a higher axial velocity fluctuation inside the ROI. This increase is related to the enhanced turbulent mixing between the entering flow and recirculated flow inside the shear layers, when the swirl intensity increases (Huang & Yang, 2005).

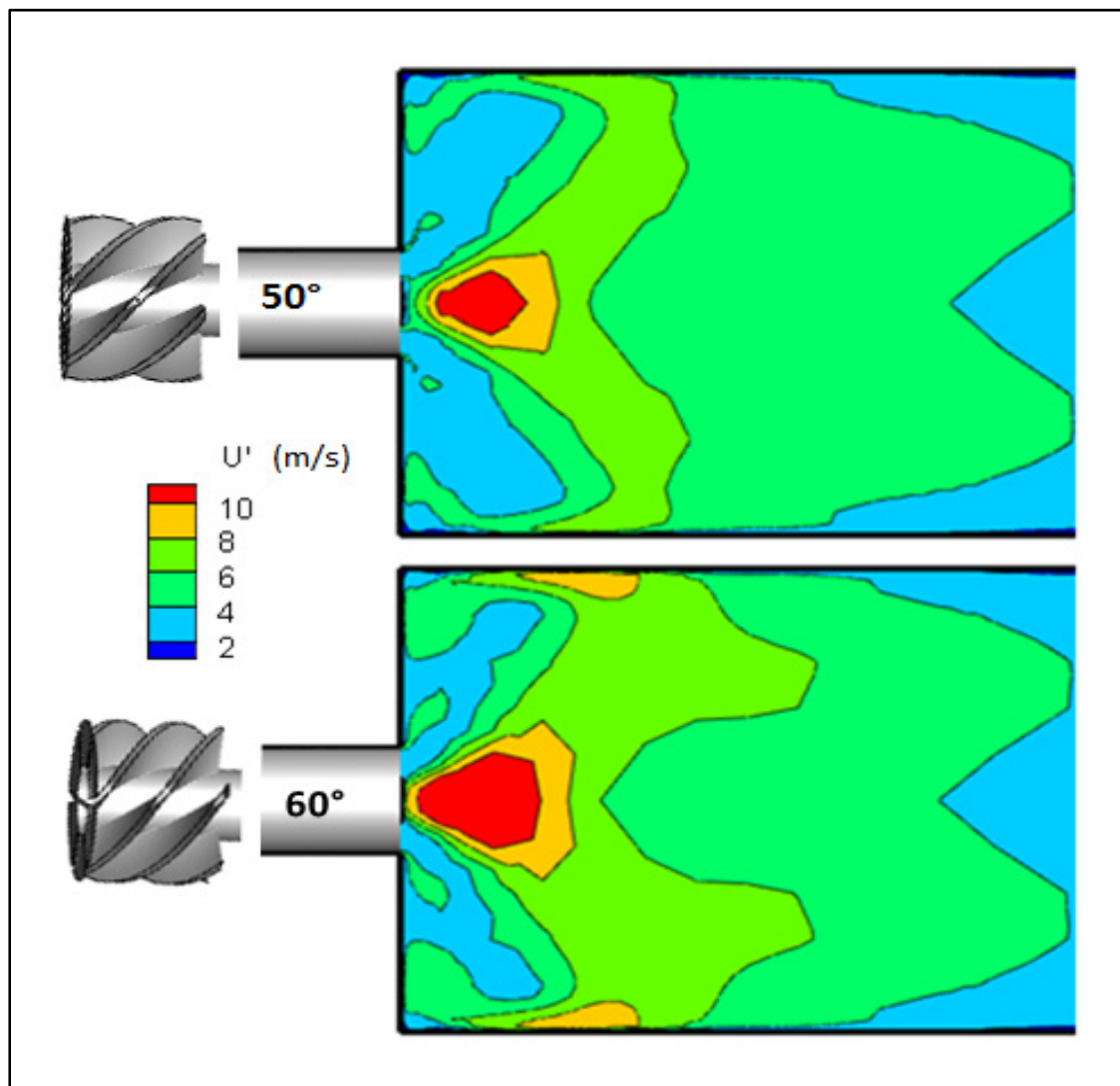


Figure 5.9 Reactive flow analysis using the axial velocity fluctuation (\hat{u}) distribution inside the ROI of the 50° (top) and 60° (bottom) swirl configurations for CH₄-air combustion at $\phi = 0.7$

The last parameter to be included in the reactive flow aerodynamics analysis is vorticity. Figure 5.10 shows the distribution of vorticity magnitude inside the ROI of the 50° (top) and 60° (bottom) swirl configurations for the reference methane case. It can be seen that the 60° swirl configuration shows enhanced vorticity levels inside the wake ($\omega \approx 8000 \text{ s}^{-1}$) and post flame ($\omega \approx 2000 - 3000 \text{ s}^{-1}$) regions, due to the 60° continuum higher tendency to rotate.

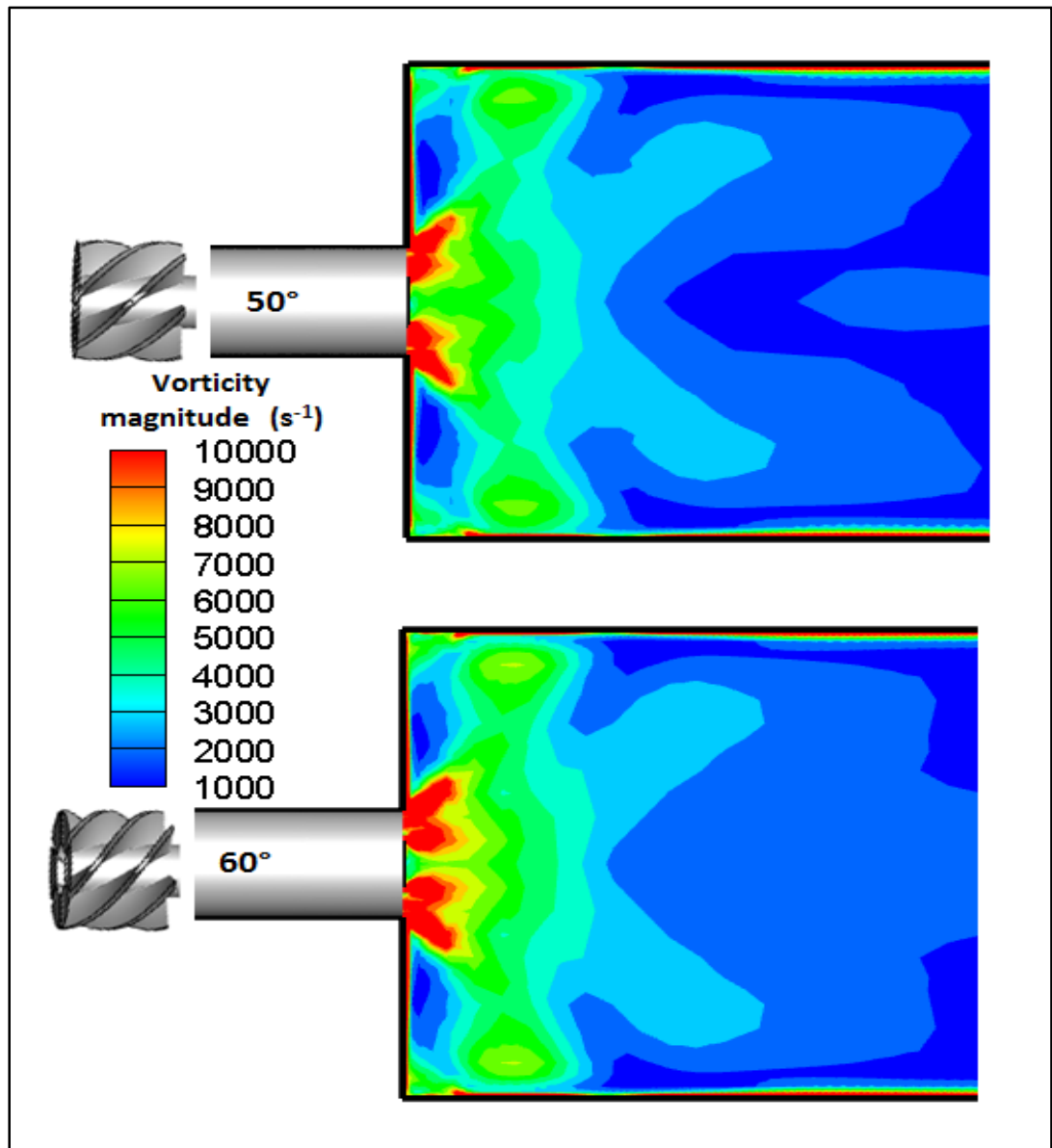


Figure 5.10 Reactive flow analysis using the vorticity magnitude distribution inside the ROI of the 50° (top) and 60° (bottom) swirl configurations for CH₄-air combustion at $\phi = 0.7$

5.2.2.1 Reactive flow chemical data

Similar to the reactive flow aerodynamics analysis, the 50° and 60° swirl configurations are compared herein from the chemistry perspective. Figure 5.11 shows the distribution of the Volumetric Heat Release Rate (VHRR), defined as the multiplication of the progress variable source term ($\dot{\omega}_c$) by the heat of reaction (considering a single-step fuel-oxygen reaction), inside the ROI of the 50° (top) and 60° (bottom) swirl configurations for the reference CH₄-air combustion at $\phi = 0.7$.

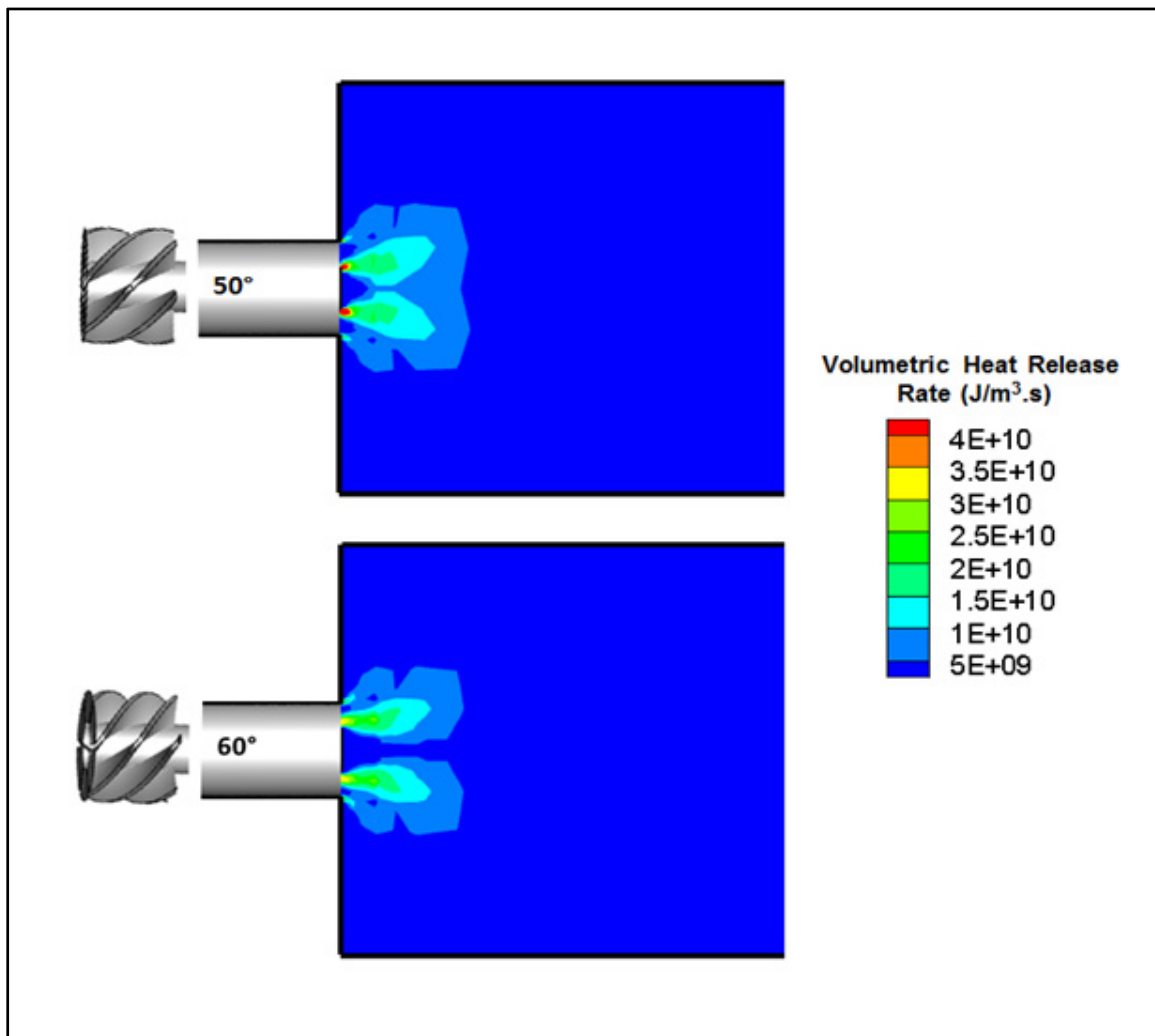


Figure 5.11 Reactive flow analysis using the volumetric heat release rate distribution inside the ROI of the 50° (top) and 60° (bottom) swirl configurations for CH₄-air combustion at $\phi = 0.7$

It can be seen that increasing the swirl vanes angle from 50° to 60° decreases the heat released at the combustion chamber entry - where flame exists - indicating that a reduced flame is one consequence of the swirl intensity increase.

Following the VHHR, the distribution of progress variable inside the ROI - indicating the flame shape - of CH_4 flame at $\phi = 0.7$ inside the 50° (top) and 60° (bottom) swirl configurations is presented in Figure 5.12. It can be seen that increasing the swirl vanes angle from 50° to 60° results in a reduced flame identified by a narrower contours of $c = 0.1$ to 0.9 , representing the transition from the unburnt mixture ($c = 0$) to the fully burnt products ($c = 1$). This reduction is attributed to the faster combustion associated with swirl increase.

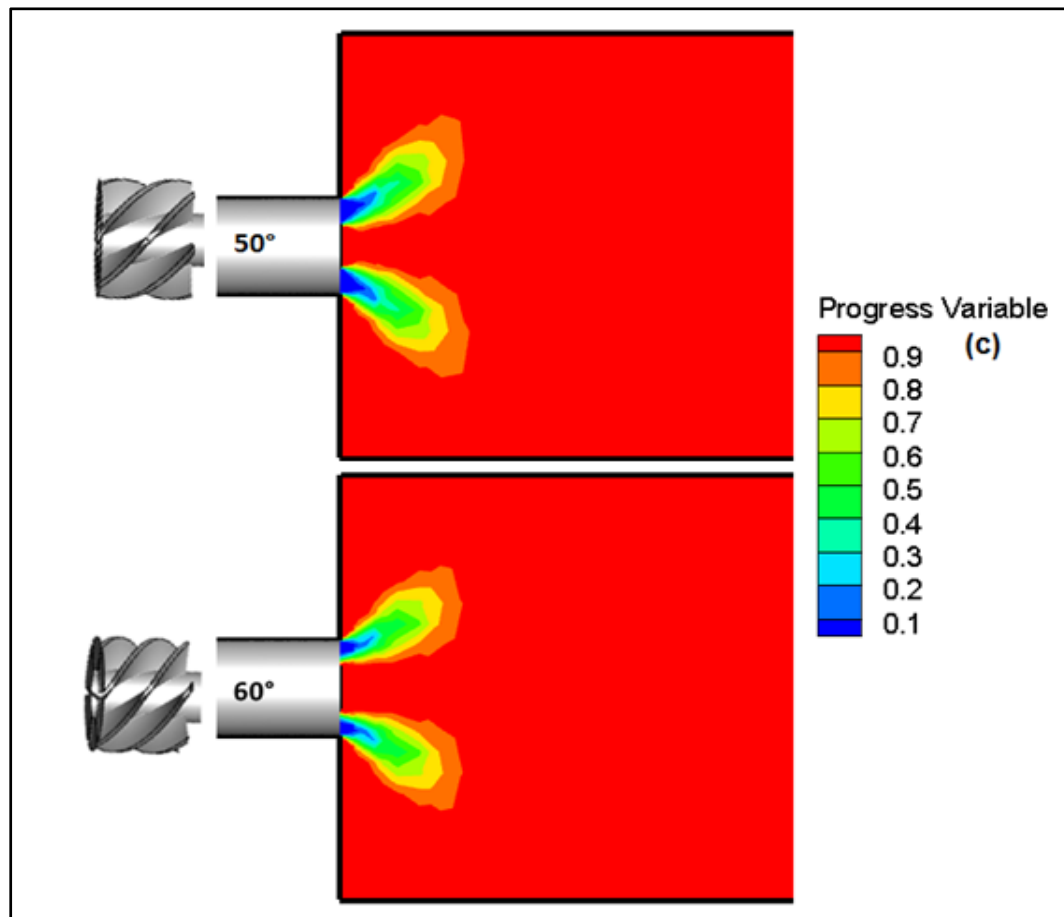


Figure 5.12 Reactive flow (CH_4 -air combustion at $\phi = 0.7$) c distribution inside the ROI of the 50° (top) and 60° (bottom) swirl configurations

Next, the 50° (top) and 60° (bottom) swirl configurations are compared in Figure 5.13 with respect to AFT. It can be seen that the 60° swirl configuration has a shorter and more compacted flame, compared to the 50°, similarly to Huang & Yang (2005). The flame compactness can be identified through the reduced size of shear layers with AFT of 1700 K (in yellow), 900 – 1300 K (in light and dark green), and the coldest temperature in light blue, 500 K. This flame compactness is linked to the reduced flame surface area and associated heat release with the swirl intensity increase, as identified earlier.

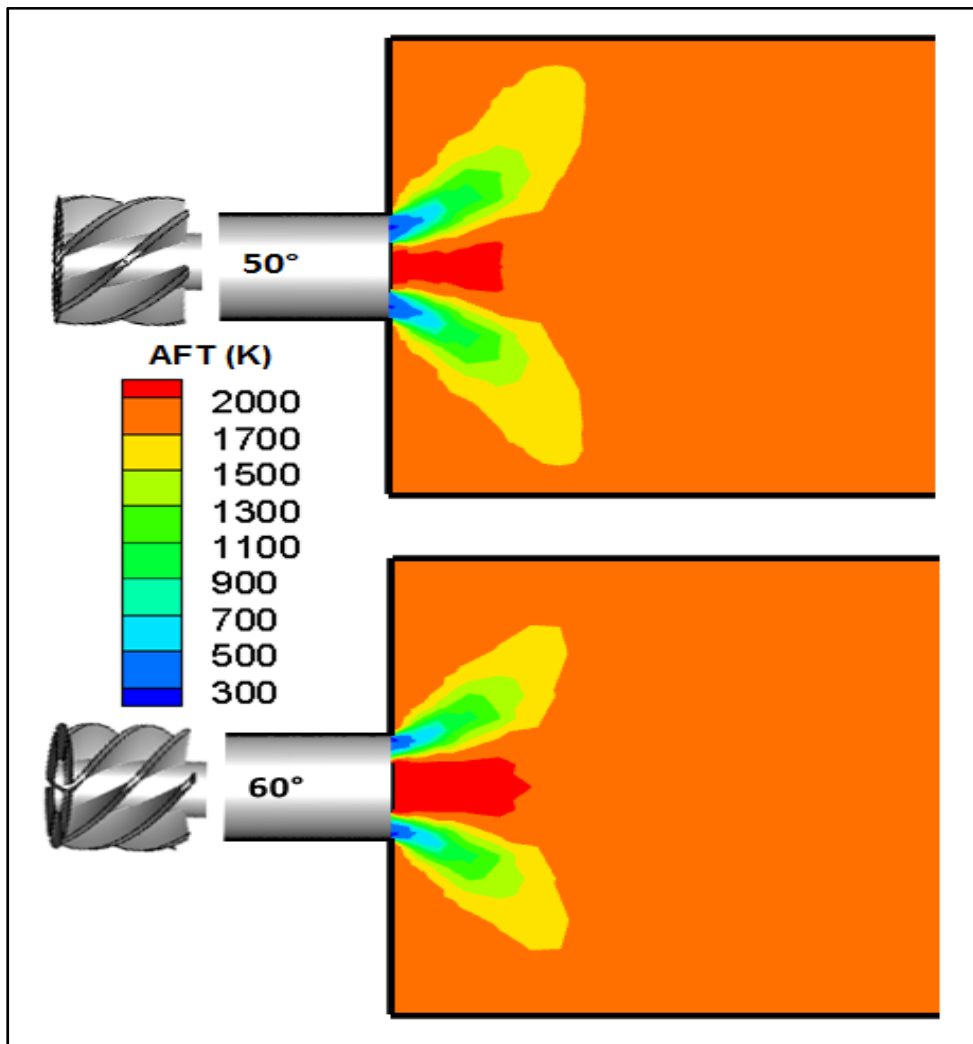


Figure 5.13 Reactive flow (CH_4 -air combustion at $\phi = 0.7$) AFT contours inside the ROI of the 50° (top) and 60° (bottom) swirl configurations

The last parameter to be included in the reactive flow chemical data analysis is the burnt temperature, including heat loss by radiation. Figure 5.14 shows the 2D burnt temperature contours inside the ROI of the 50° (up) and 60° (down) swirl configurations for the reference CH₄ flame at $\phi = 0.7$. It can be observed that the 60° swirl configuration shows a narrower area with $T = 1900$ K (in orange) compared to the 50° swirl configuration.

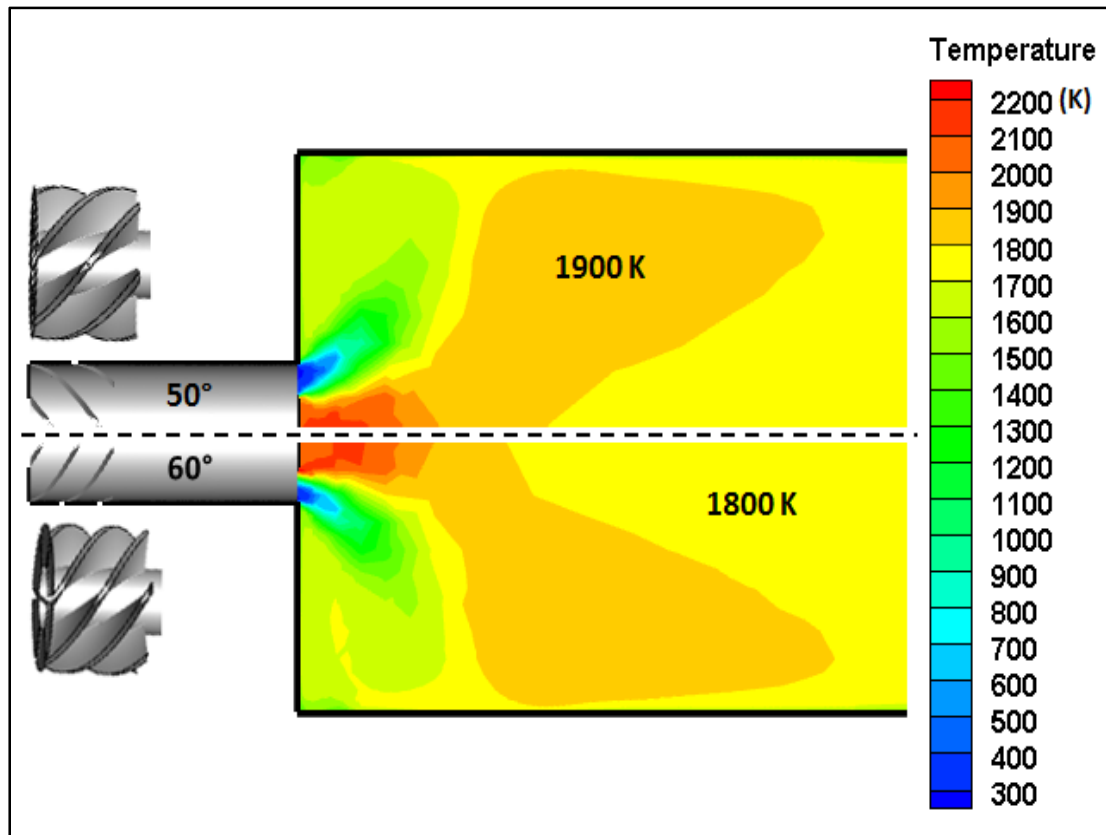


Figure 5.14 Reactive flow (pure methane, $\phi = 0.7$) 2D temperature (with radiation) contours inside the ROI for the 50° (top) and 60° (bottom) swirl configurations

For further analysis, the 3D iso-temperature surfaces at $T = 300$ (blue), 1300 (green), and 1800 (gold) K are presented for the 50° (top) and 60° (bottom) swirl configurations in Figure 5.15. It can be observed that increasing the swirls vanes angle from 50° to 60° results in a more compacted and shorter isothermal layer with $T = 1800$ K (in gold). Such a conclusion matches with the reduced VHHR (identified earlier) and AFT distribution inside the shear layers, identified above.

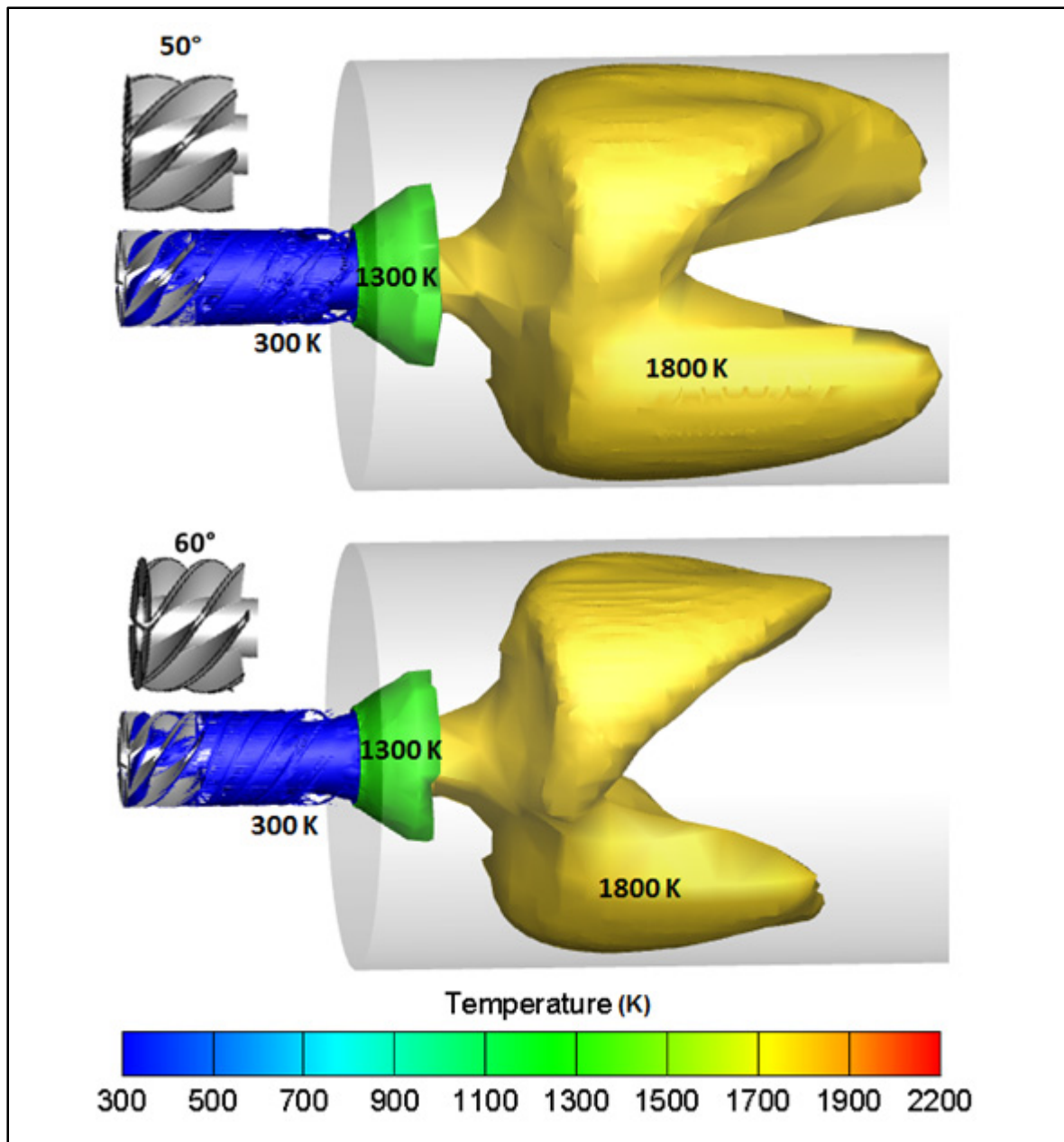


Figure 5.15 Reactive flow (pure methane, $\phi = 0.7$) 3D temperature (with radiation) iso-surfaces at 300 (blue), 1300 (green), and 1800 K (orange) for the 50° (top) and 60° (bottom) swirl configurations

Based on the aforementioned analyses and comparisons, the effect of swirl intensity on the cold flow properties and reactive CH_4 -air combustion characteristics is identified. Next, HEC will be characterized under high swirl levels.

5.3 HEC study at high swirl level

In this section, the effect of the swirl intensity on the global flow pattern, VHRR, flame shape, burnt temperature and NO_x emissions, and combustion regime will be studied at high swirl (S up to 1.3) in combination with particular hydrogen addition under lean and stoichiometric burning conditions, which will allow to reach the third research sub-objective (A3).

5.3.1 H_2 -swirl- ϕ effect on the global flow pattern and vorticity

In this section, the effect of swirl intensity on the global flow pattern is studied for particular hydrogen addition and equivalence ratios. Results are presented by comparing the CH_4 -air combustion (top) to HEC with HVR up to 90% at $\phi = 0.7$ in Figure 5.16, where the 2D streamlines are mapped over the temperature (up) and OH radical (down). Then, and for further analysis, CH_4 -air combustion (top) and HEC with HVR = 60% (bottom) are compared at $\phi = 0.7$ (left) and 1 (right) in Figure 5.17, where the 2D streamlines are mapped over the axial velocity contours. Such a fuel blend (HVR = 60%) is selected herein so as to show meaningful distinctions, as it is considered the highest HVR that could be used for enriching the CH_4 -air combustion inside the 50° and 60° swirl configurations, under lean and stoichiometric burning conditions.

Looking at Figure 5.16, a general conclusion can be reached that is under GTE operating conditions, turbulence governs the combustion phenomenon than hydrogen addition or swirl intensity. Such a conclusion is reached as all studied cases show the typical flow pattern, characterized by the formation of IRZ, CRZ, and shear layers, indicating that up to 90% of H_2 could be used for enriching the lean premixed CH_4 -air combustion process inside both swirl configurations, under the studied conditions of high turbulence and atmospheric pressure and temperature. However, further investigations are needed to confirm this possibility. The same figure also indicates the global effect of hydrogen addition and swirl intensity on the IRZ size, which increases with the swirl intensity increase. However, it decreases with the hydrogen concentration increase.

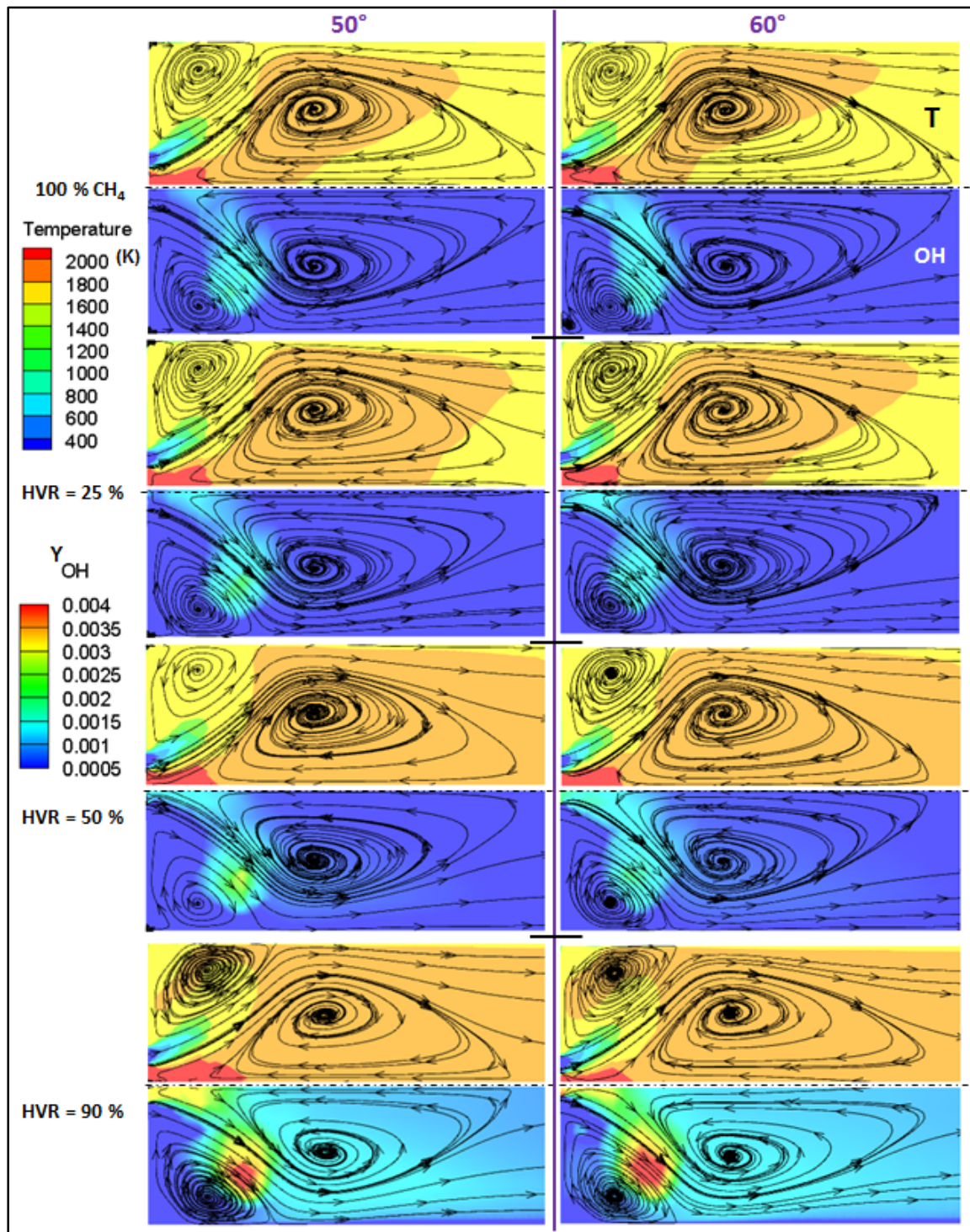


Figure 5.16 2D streamlines distribution inside the ROI at $\phi = 0.7$ mapped over the temperature (up) and OH radical (down) for methane and HEC with HVRs = 25, 50, and 90% (from top to bottom)

Looking at Figure 5.17, it can be seen that increasing the swirl vanes angle from 50° to 60° for both flames increases the size of IRZ ($u = -10$ m/s), due to the increased swirl intensity, as well as increases the axial velocity inside the shear layers ($u = 30$ m/s in red), due to the faster expansion of the inlet jet from the swirler into the combustion chamber, under the centrifugal force effect. The effect of swirl intensity increase on the IRZ size is clearer at the stoichiometric burning condition (for both flames) as well as at $\phi = 0.7$ for HEC with HVR = 60% (compared to the reference CH_4 flame), due to the hydrogen higher reactivity that helps promoting the reactions.

Another conclusion could be reached that is the upstream flow is more susceptible to swirl intensity change than hydrogen addition to methane, which was also reached by Kim *et al.* (2009 a), even for less turbulent conditions.

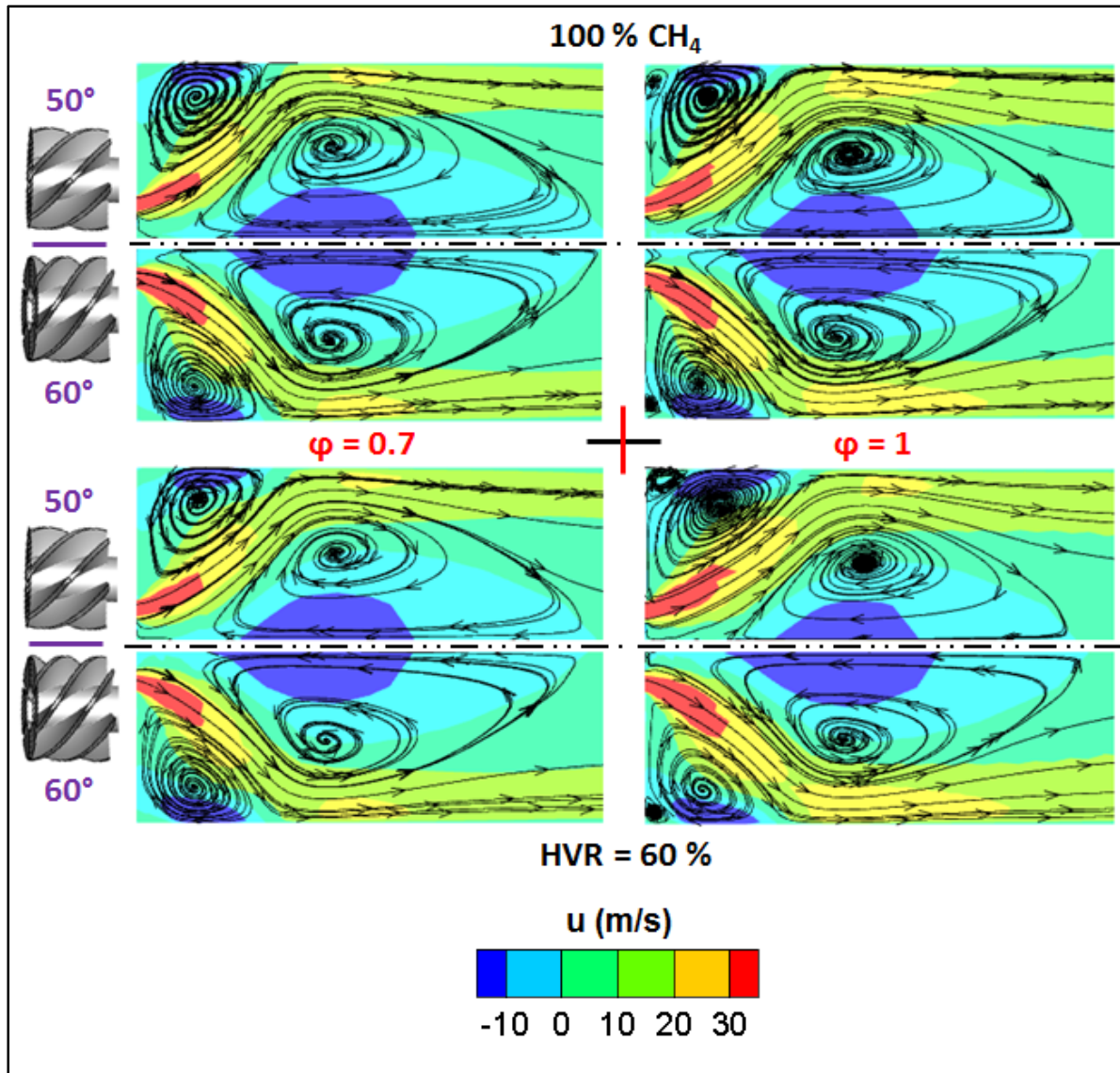


Figure 5.17 2D streamlines distribution inside the ROI mapped over the axial velocity for the reference CH₄ case (top) compared to HEC with HVR = 60% (bottom) at $\phi = 0.7$ (left) and 1 (right) for the 50° (up) and 60° (down) swirl configurations

The study is then pursued for the effect of swirl intensity on vorticity. Figure 5.18 shows the 2D vorticity magnitude distribution inside the ROI of the 50° (up) and 60° (down) swirl configurations by comparing the reference CH₄ flame (top) to HEC with HVR = 60 % (bottom) at $\phi = 0.7$ (left) and 1 (right). It can be seen that increasing the swirl vanes angle from 50° to 60° enhances the vorticity levels inside the wake ($\omega \approx 8000 \text{ s}^{-1}$) and post flame ($\omega \approx 2000 - 3000 \text{ s}^{-1}$) regions, due to the 60° continuum higher tendency to rotate. Moreover,

swirl intensity is more influential on the vorticity levels than HVR (up to 60%) or equivalence ratio.

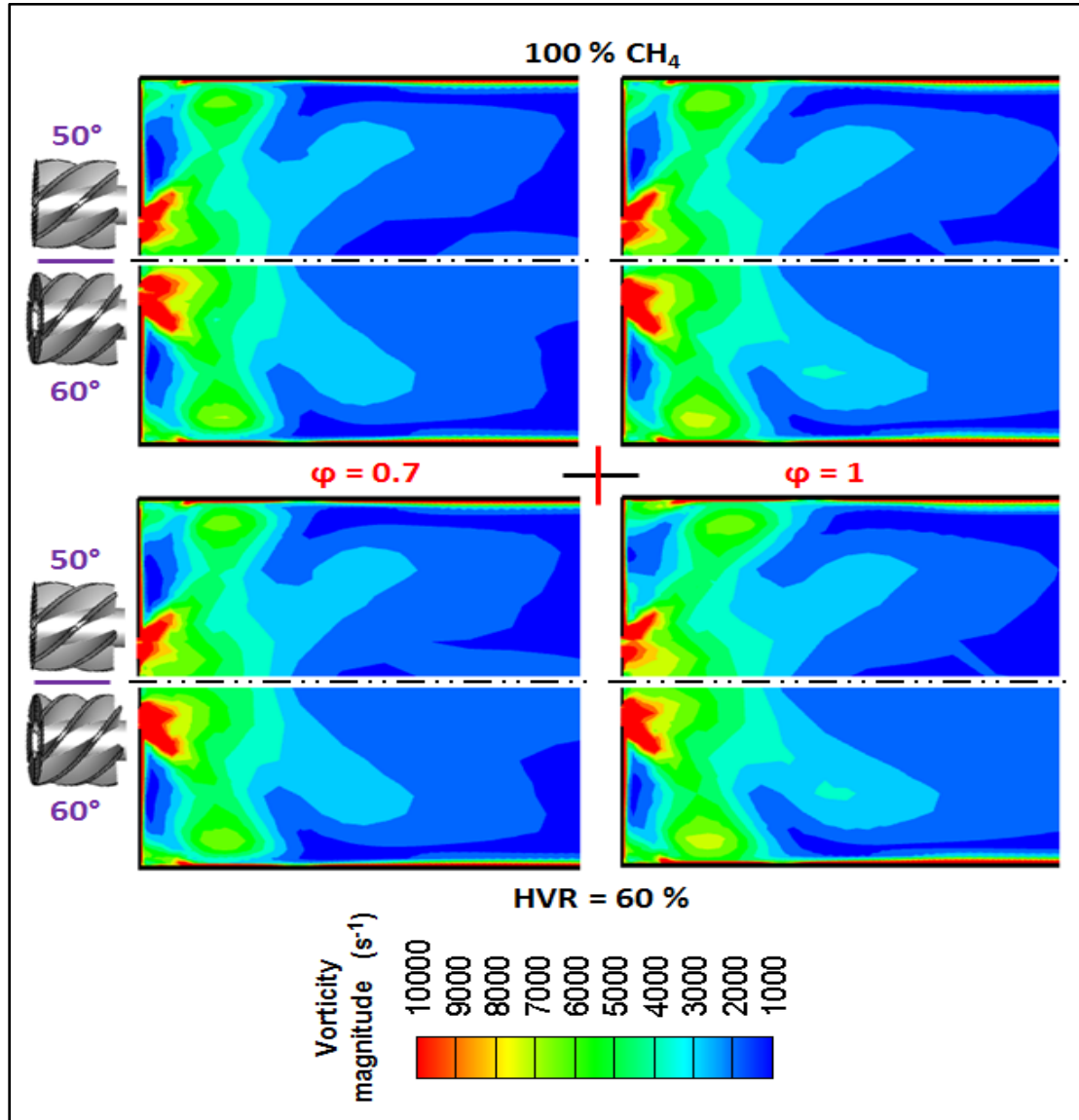


Figure 5.18 Vorticity contours inside the ROI for the reference methane case (top) compared to HEC with HVR = 60 % (bottom) at $\phi = 0.7$ (left) and 1 (right) for the 50° (up) and 60° (down) swirl configurations

For the stoichiometric HEC with HVR = 60%, the vorticity level inside the wake region is high ($\omega \approx 8000 \text{ s}^{-1}$) for both swirl angles, however, the 60° swirl configuration shows an enhanced level of vorticity ($\omega \approx 2000 - 3000 \text{ s}^{-1}$) in the post-flame region.

5.3.2 H₂-swirl- ϕ effect on the Volumetric Heat Release rate (VHRR)

The effect of swirl intensity on the VHRR is studied in Figure 5.19 at $\phi = 0.7$ (top) and 1 (bottom) for CH₄-air combustion and HEC with HVR = 25, 50, and 60%, from left to right, respectively, inside the 50° (up) and 60° (down) swirl configurations. It can be seen that increasing the swirl vanes angle from 50° to 60° decreases the VHRR at the combustion chamber entry, where flame exists. Such a conclusion holds true for CH₄ and the three studied H₂-CH₄ blends (25, 50, and 60%) at both equivalence ratios (0.7 and 1). The VHRR decrease is linked to the increased turbulent intensity with swirl angle increase, which reduces the flame surface area and associated heat release, as stated before.

From the same figure also, it can be observed that increasing the equivalence ratio from 0.7 to 1 increases the VHRR, due to the increased amount of liberated heat when burning richer fuel-air mixtures. Such a conclusion holds true for all studied fuels and is clearer for the 50° swirl configuration than the 60°, as the VHRR is decreasing with the swirl intensity (angle) increase.

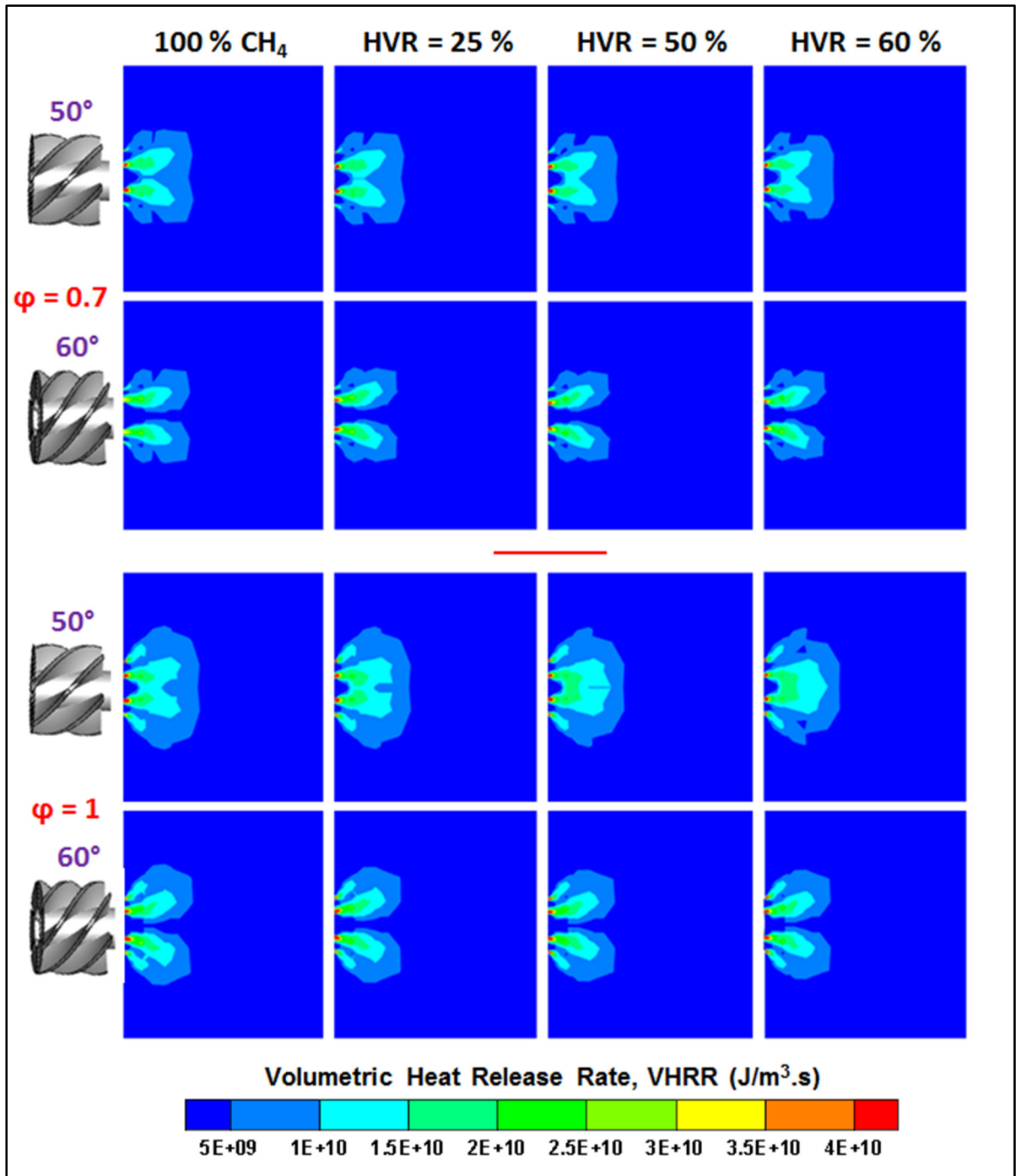


Figure 5.19 Volumetric heat release rate contours inside the ROI of the 50° (up) and 60° (down) swirl configurations at $\phi = 0.7$ (top) and $\phi = 1$ (bottom) for the reference methane case and HEC with HVR = 25, 50, and 60% (from left to right)

5.3.3 H₂-swirl- ϕ effect on the flame shape

Following the flow field, the effect of swirl intensity on the flame shape is identified in terms of the OH radical at $\phi = 0.7$ in Figure 5.20 by comparing the reference CH₄ flame (top left) to HEC with HVR = 25% (top right), 50% (bottom left), and 60% (bottom right) as well as in terms of the progress variable in Figure 5.21 by comparing the reference CH₄ flame (top) to HEC with HVR = 60% (bottom) at $\phi = 0.7$ (left) and 1 (right).

Looking at Figure 5.20, it can be seen that increasing the swirl vanes angle from 50° to 60° helps reattaching the CH₄-air flame (top left), which looks detached for the 50°, as well as decreases the size of OH peaks in the flame, indicating a more compacted flame. This flame compactness appears clearer for HEC with HVR = 50 and 60% (bottom left and right), due to H₂ higher reactivity, and is attributed to the increased turbulent intensity which in turn reduces the flame surface area and associated heat release, as indicated earlier.

Figure 5.20 also shows that CH₄ (top left) and 25-75% H₂-CH₄ (top right) flames look similar under both swirl levels, highlighting that this hydrogen blend could replace CH₄-air combustion at the primary stage of GTE operation, even at high swirl level.

Looking at it Figure 5.21, it can be observed that increasing the swirl vanes angle from 50° to 60° results in shorter flames (due to faster flame speed) and enhances the fuel-air mixing inside the shear layers, which can be distinguished by the narrower contours of c representing the transition from the unburnt mixture status ($c = 0.05$) to the completely burnt products ($c = 0.95$). Such a conclusion holds true for both fuels at both equivalence ratios.

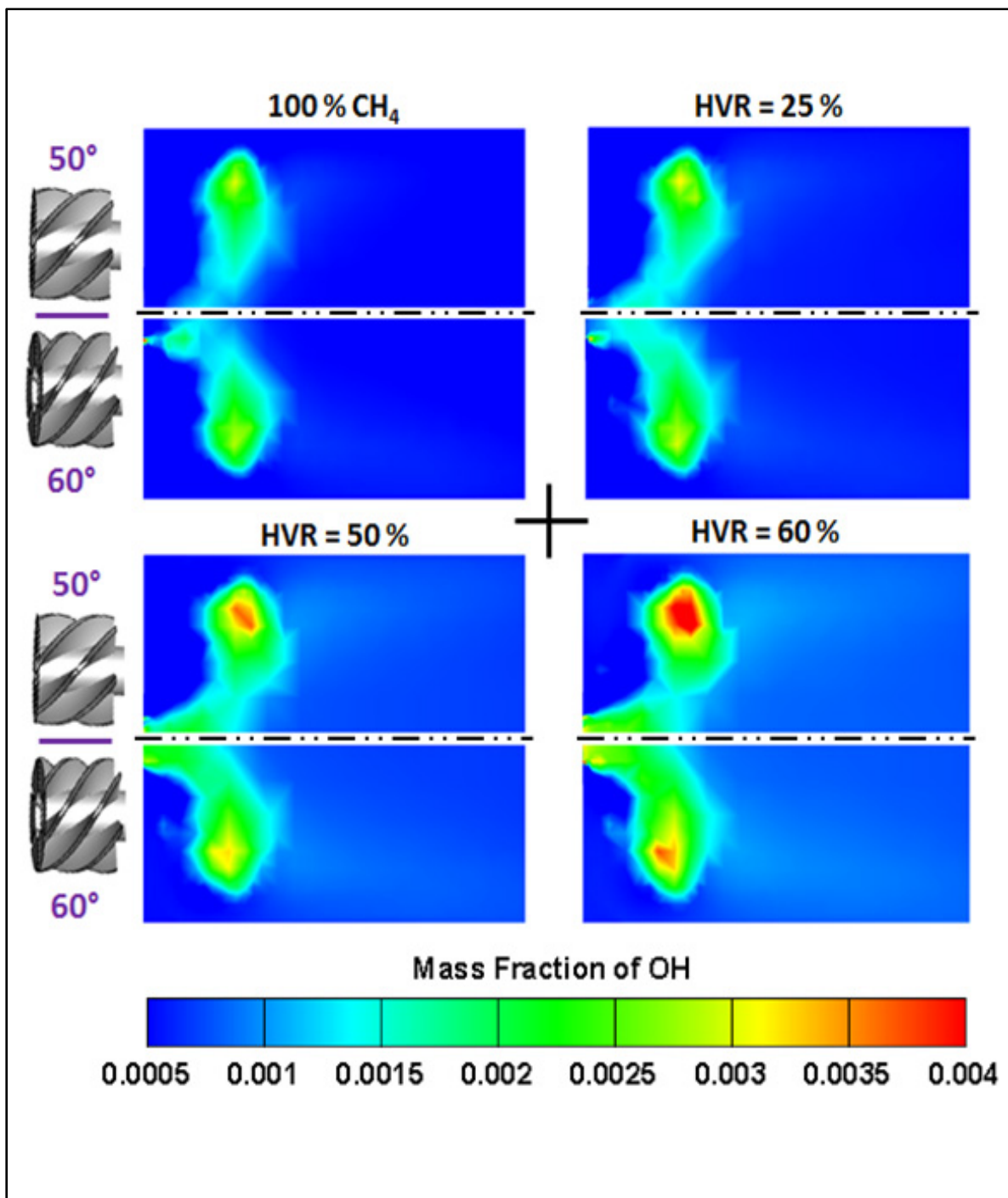


Figure 5.20 OH mass fraction contours inside the ROI of the 50° (up) and 60° (down) swirl configurations at $\phi = 0.7$ for the reference methane flame (top left) compared to HEC with HVR = 25% (top right), 50% (bottom left), and 60% (bottom right)

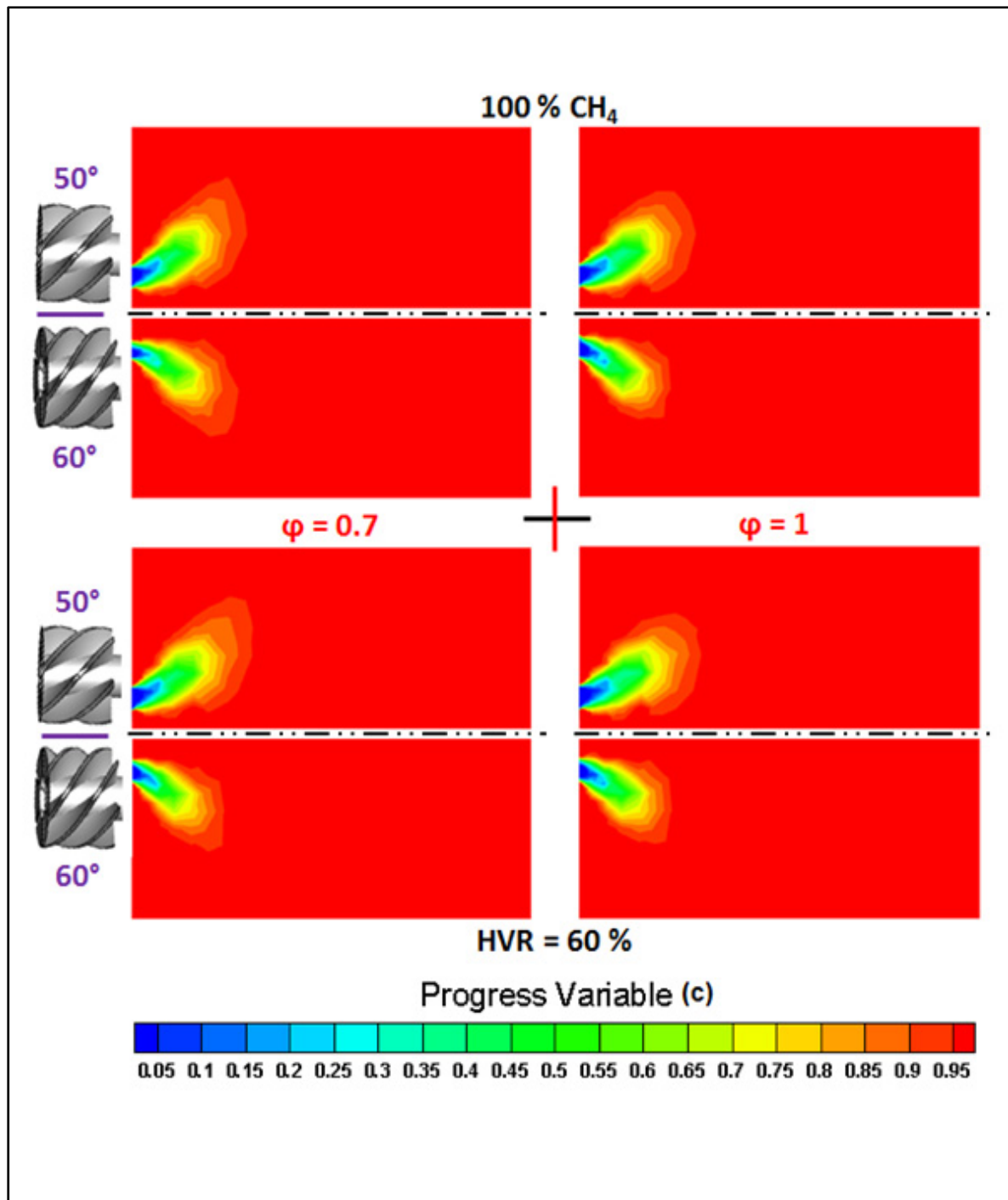


Figure 5.21 Progress variable contours inside the ROI for the reference methane case (top) compared to HEC with HVR = 60% (bottom) at $\phi = 0.7$ (left) and 1 (right) for the 50° (up) and 60° (down) swirl configurations

5.3.4 H₂-swirl- ϕ effect on the burnt temperature (with radiation)

The study now is pursued to identify the effect of swirl intensity on the burnt temperature - considering heat loss by radiation - by comparing the reference CH₄ flame (top) to HEC with HVR = 60% (bottom) at $\phi = 0.7$ (left) and 1 (right), as seen per Figure 5.22.

It can be seen that increasing the swirl vanes angle from 50° to 60° results in reducing the size of regions with $T = 1900$ K at $\phi = 0.7$ for CH₄ flame and with $T = 2280$ K at $\phi = 1$ for HEC with HVR = 60%. Moreover, the 60° swirl configuration shows a more uniform temperature, which is evident at $\phi = 0.7$ for HEC with 60% H₂. Last, the 60° swirl configuration shows a different temperature distribution inside the shear layers and corners (compared to the 50°), due to the higher axial, radial, and total velocities identified in the 60° shear layers, which in turn enhances the fuel-air mixing, as identified before in terms of the progress variable (Figure 5.21).

A more uniform temperature at the combustion chamber outlet is a benefit in gas turbine application because an uniform temperature distribution on the turbine blades is required. In addition, the difference in temperature distribution (such as in corners) is as an implication on combustion chamber cooling design.

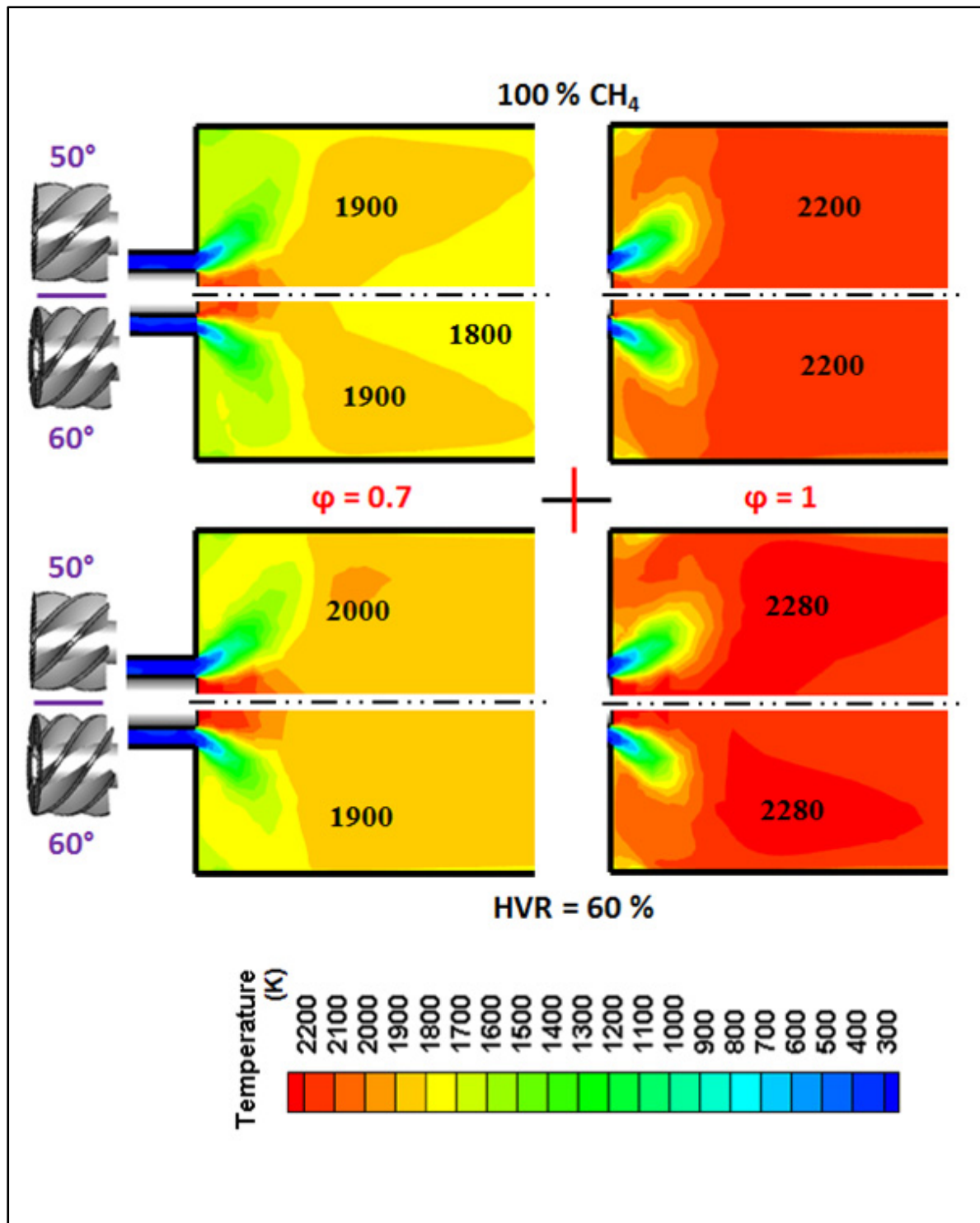


Figure 5.22 2D temperature contours inside the ROI for the reference methane case (top) compared to HEC with HVR = 60% (bottom) at $\phi = 0.7$ (left) and 1 (right) for the 50° (up) and 60° (down) swirl configurations

5.3.5 H₂-swirl effect on emissions

Following the temperature, the effect of swirl intensity on NO_x emissions is studied for particular HVRs in combination with three swirl levels. To do so, the averaged outlet NO_x at $\phi = 0.7$ are presented in Figure 5.23 as a function of the outlet temperature under three swirl levels, $S = 0.9, 1.1$, and 1.3 , corresponding to $\alpha = 50^\circ, 55^\circ$, and 60° , with (top) and without (bottom) considering radiation heat loss. The figure shows the non-linear effect of H₂ addition on temperature for a given swirl angle. Moreover, it shows the interaction between H₂ addition and swirl intensity as the temperature increase (for a given H₂ concentration) is more important with increasing the swirl angle. The net consequence is an exponential increase of NO_x emissions with increasing H₂ addition for a constant swirl angle and a very fast increase of NO_x emission with increasing the swirl angle when combined with high H₂ concentrations (75 and 90%).

Regarding the effect of radiation, it can be seen that considering heat transfer by radiation results in an average reduction of the predicted temperature at the burner's outlet by ≈ 100 K, which is translated into a reduction of the predicted NO_x by $\approx 50\%$. Such a conclusion highlights the importance of considering heat loss by radiation, while conduction numerical modelling.

Similar trends but different levels are identified for the stoichiometric HEC; where considering heat loss by radiation appears significant for the predictions of NO_x emissions, due to higher temperatures. Results are not presented for brevity.

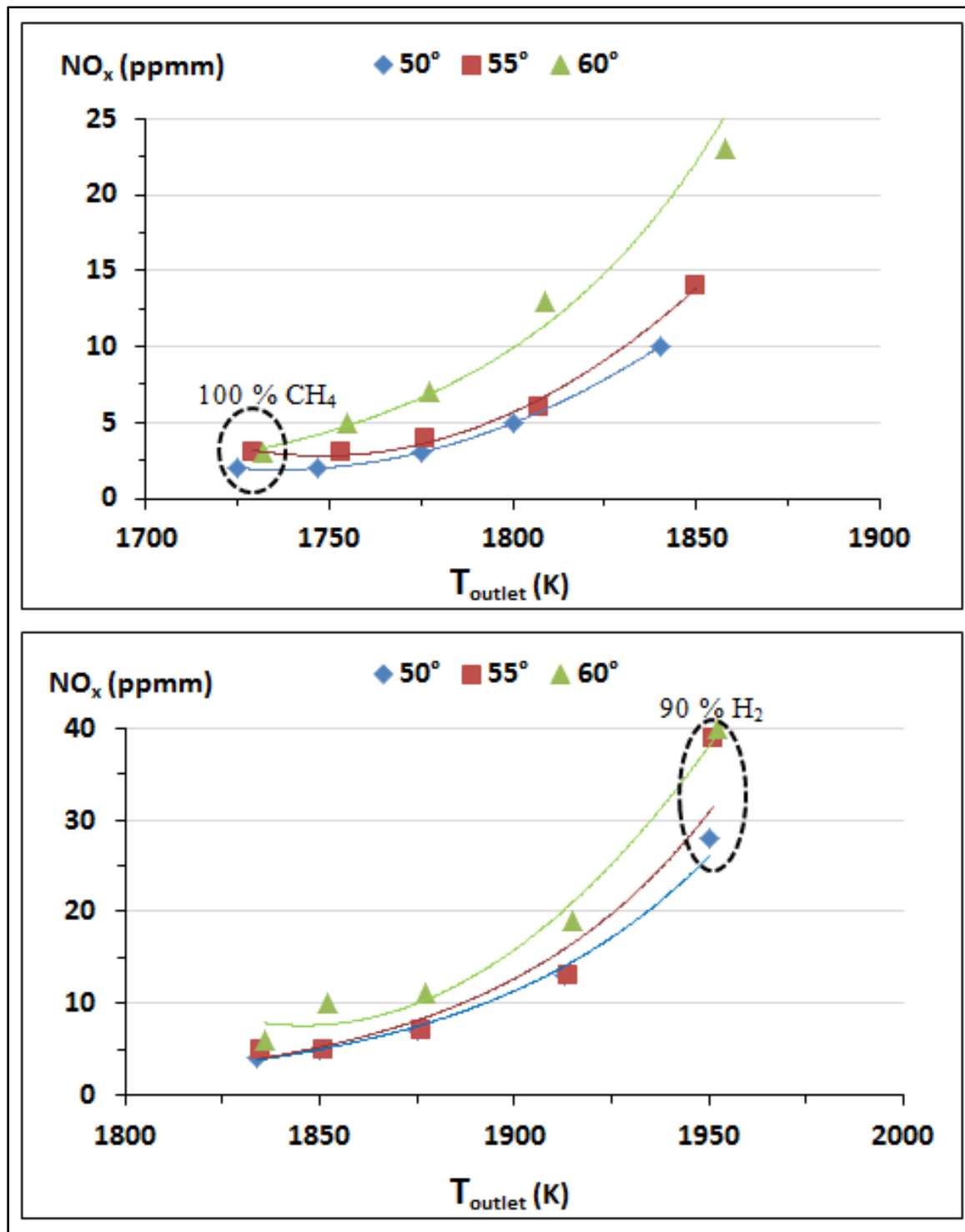


Figure 5.23 NO_x versus the temperature at the burner outlet for the 50°, 55°, and 60° swirl configurations and HVRs: 0, 25, 50, 75, and 90%, from left to right, respectively, considering radiation (top) and adiabatic (bottom), case $\phi = 0.7$

In addition to NO_x emissions, the effect of swirl intensity on NO and CO trends is studied for the stoichiometric HEC, following the same approach stated above to analyze NO_x . Figure 5.24 shows the outlet NO (left axis) and CO (right axis) mass fractions versus the outlet temperature for the 50° , 55° , and 60° swirl angles in combination with HVRs up to 90% at $\phi = 1$, with (top) and without (bottom) considering heat loss by radiation.

It can be seen that considering heat transfer by radiation reduces the outlet NO and CO mass fractions by half. This reduction is attributed to an average temperature difference of ≈ 130 K. Hence, radiation is concluded to be influential.

It can also be observed that NO and CO always have a reciprocal trend, where NO is maximum and CO is minimum for the highest temperature, and vice versa when the temperature is lowest. Small variations of NO and CO mass fractions are observed between the three swirl configurations - for a given temperature - when considering heat transfer by radiation. This is linked to the slight variations in temperature governing NO and CO formation.

For further investigation of carbon emissions, two analyses of the carbon atom (C) mass balance between the inlet C (from CH_4 stream) and the outlet C (in products) are performed. First, the carbon atom mass balance is performed for the basic swirl configuration (50°) in combination with HVRs up to 90% at $\phi = 0.7$ in Table 5.2, where $\text{Mc}/\text{CO}_2 / \text{Mc}/\text{CH}_4$ is the ratio between the mass fraction of carbon in the outlet carbon dioxide stream to the mass fraction of carbon in the inlet methane stream. Second, the carbon atom mass balance is performed for the three swirl configurations (50° , 55° , and 60°) in combination with HVRs up to 50% at $\phi = 1$ in Table 5.3.

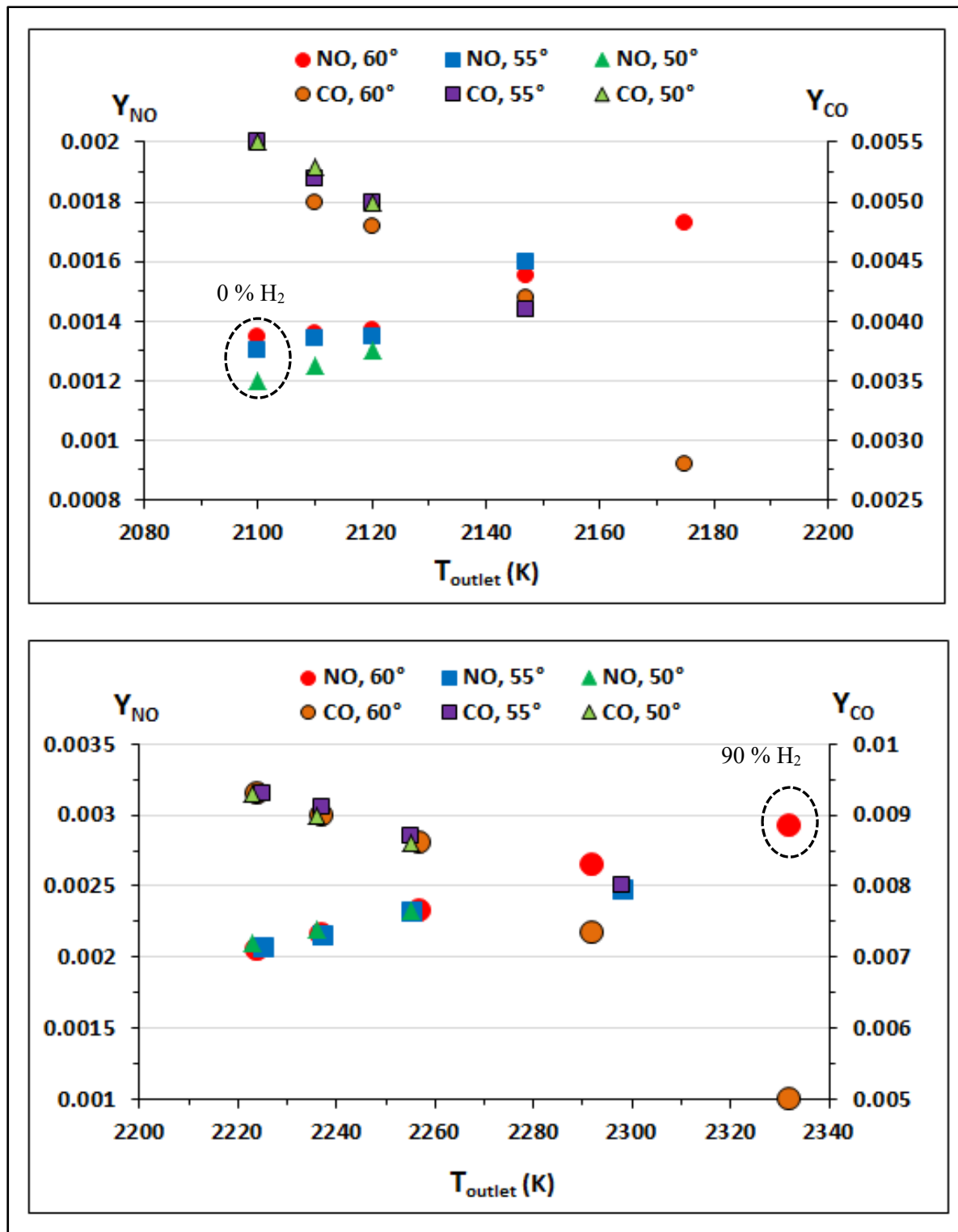


Figure 5.24 NO (left axis) and CO (right axis) versus the temperature at the burner outlet for the 50°, 55°, and 60° swirl configurations and HVRs: 0, 25, 50, 75, and 90%, from left to right, respectively, considering radiation (top) and adiabatic (bottom), case $\phi = 1$

Table 5.2 Carbon atom (C) mass balance between the inlet CH₄ and outlet CO₂ for the basic swirl configuration at $\phi = 0.7$ and HVRs up to 90%

Parameter	Thermal state	HVR %				
		0	25	50	75	90
Mc/CH_4		0.029	0.027	0.024	0.017	0.009
Mc/CO_2	Radiation	0.029	0.027	0.024	0.017	0.009
	Adiabatic	0.029	0.027	0.024	0.017	0.009
$\text{Mc}/\text{CO}_2 / \text{Mc}/\text{CH}_4$	Radiation	0.995	1.000	1.000	1.000	1.000
	Adiabatic	0.995	1.000	1.000	1.000	1.000

Based on the analysis presented in Table 5.2, it can be concluded that the HEC process at $\phi = 0.7$ is complete, for whatever HVR, as $\text{Mc}/\text{CH}_4 = \text{Mc}/\text{CO}_2 \text{ radiation} = \text{Mc}/\text{CO}_2 \text{ adiabatic}$. Such a conclusion is not applied for the stoichiometric HEC, which is not likely to be complete, for whatever HVR also. Results are not presented for the stoichiometric HEC for brevity. However, it is concluded that considering radiation is important for both burning conditions.

Table 5.3 Carbon atom (C) mass balance between the inlet CH₄ and outlet CO and CO₂ for the three swirl configuration (50°, 55°, and 60°) at $\phi = 1$ and HVRs up to 50%

Swirl angle (α)	Parameter	HVR %		
		0	25	50
50°	$\frac{\text{A. Mc}/\text{CO}_2}{\text{Mc}/\text{CH}_4}$	0.946	0.938	0.932
	$\frac{\text{B. Mc}/\text{CO}}{\text{Mc}/\text{CH}_4}$	0.057	0.059	0.065
55°	$\frac{\text{A. Mc}/\text{CO}_2}{\text{Mc}/\text{CH}_4}$	0.948	0.944	0.936
	$\frac{\text{B. Mc}/\text{CO}}{\text{Mc}/\text{CH}_4}$	0.057	0.059	0.065
60°	$\frac{\text{A. Mc}/\text{CO}_2}{\text{Mc}/\text{CH}_4}$	0.949	0.944	0.936
	$\frac{\text{B. Mc}/\text{CO}}{\text{Mc}/\text{CH}_4}$	0.057	0.059	0.062

Based on the analysis presented in Table 5.3, it can be concluded that increasing the swirl vanes angle is likely to slightly increase CO conversion into CO₂, due to the slight increase in temperature and residence time associated with the swirl vanes angle increase.

5.3.6 H₂-swirl- ϕ effect on the turbulent premixed combustion regime

The last parameter to be studied herein is the turbulent premixed combustion regime, which is characterized in terms of the turbulent Damköhler (Da) and Karlovitz (Ka) numbers, representing the ratios of the turbulent mixing time scale to the chemical one and the chemical time scale to the Kolmogorov one (smallest eddy), respectively. The unity Prandtl number assumption is considered, similarly to Taupin et al. (2007); Peters (2001). Moreover, the turbulent Da and Ka number calculations are also verified using the heuristic expressions from Turns (2000), relating the turbulent velocity, turbulent time scale, and turbulent length scale in the Kolmogorov and integral scales.

The combustion regime is located in the Borghi diagram (u'/S_L versus l_0/δ) in Figure 5.25, similarly to Tu, Xu, Zhou, Wang, Yang, & Liu (2019) and it can be characterized by: a. $Da \approx 1$, b. $1 < Re_{turb} \leq 10^4$, c. $1 < u'/S_L < 50$, d. $l_0/\delta \approx 50$, and e. $1 < Ka < 100$. Hence, the studied regime is located as “Thin reaction sheets” in the Borghi diagram. This implies that the smallest eddies increase heat and mass transfer in the flame preheat zone resulting in a thicker flame. The variations of Da and Ka with the hydrogen addition and swirl intensity increase were calculated and found not influential, due to the nature of the model herein that doesn't take into account hydrogen preferential diffusion. This indicates that at high turbulence levels, turbulence plays an important role governing the combustion phenomenon than hydrogen addition or swirl intensity.

On the other hand, the same figure shows the location of flames studied in some recent literature, such as flames of Nemitallah *et al.* (2019); Imteyaz *et al.* (2018); Ali *et al.* (2020) located as “quasi-laminar or wrinkled flamelets”. Such flames are characterized by $Da \gg 1$, $Ka < 1$, and $u'/S_L \approx 1$, which indicates that they are governed by the chemical kinetics.

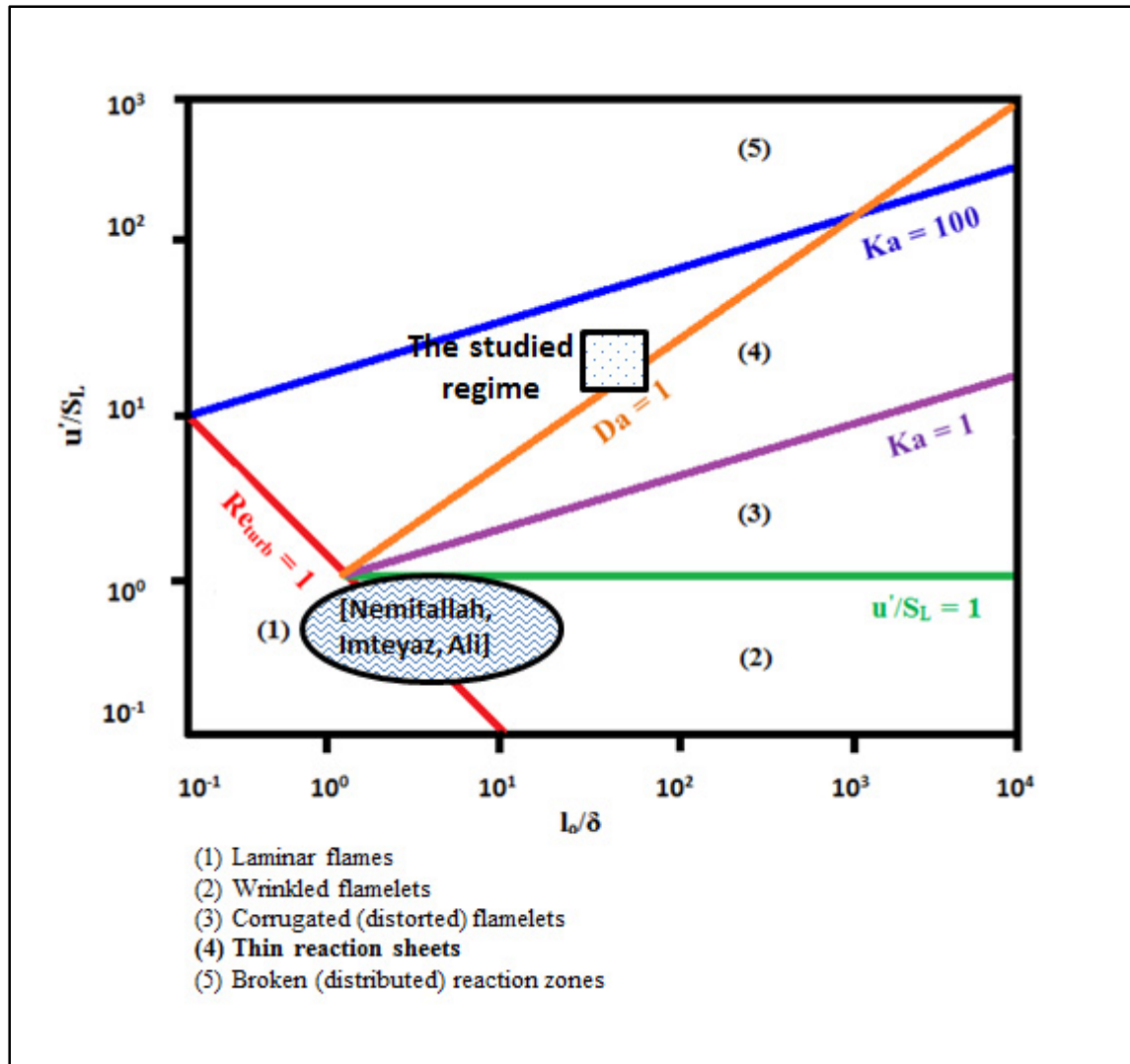


Figure 5.25 Borghi diagram (u'/S_L versus l_o/δ)

In the final analysis, it can be concluded that at high turbulence levels ($20 \leq u'/S_L \leq 45$), turbulence plays an important role controlling the combustion phenomenon than hydrogen addition or swirl intensity.

5.4 Chapter conclusions

The goal of this chapter was to identify the effect of swirl intensity on the flame structure and emissions for particular hydrogen concentrations under lean and stoichiometric burning conditions. First, the combustor geometry has been modified in order to account for swirl intensity change, in terms of the swirl angle. Then, the effect of swirl intensity on cold flow and CH₄-air combustion at ($\phi = 0.7$) was identified and compared with numerical data from the literature. Last, HEC has been characterized under high swirl levels (S up to 1.3) and lean and stoichiometric burning conditions.

It was concluded that increasing the swirl vanes angle increases the size of IRZ and shifts its location in the upstream direction, increasing the axial, radial, and resultant velocity inside the shear layers, increases the turbulent intensity, reduces the flame area and associated heat release, results in shorter and more compacted flames.

Regarding emissions, swirl intensity was found slightly increasing NO_x and reducing CO, due to the slight increase of temperature. However, the increase of NO_x was considered not important, as the NO_x levels were few ppm at the burner's outlet.

Last, it was concluded that changing swirl intensity does not significantly affect the turbulent combustion regime, which was located as "Thin reaction sheets" in the Borghi diagram.

CONCLUSION

A numerical study of H₂-enriched CH₄-air combustion under high turbulence and swirl levels was conducted. A numerical model of an industrial lab-scale combustor was proposed (in Chapter 2) and used to identify the effects of H₂ addition to CH₄ (in Chapter 4) and swirl intensity (in Chapter 5) on the combustion parameters and emissions, after a previous validation with experimental data from the literature (in Chapter 3). The combustor numerical model was in a satisfactory agreement with the experimental results from the literature (with a maximum error of 5%) and the results predicted by CFD highlighted the privilege of the RANS-FGM approach used for modelling the turbulent premixed combustion process.

A wide range of hydrogen (up to 90%) was used for enriching CH₄-air combustion under high turbulence ($u'/S_L \approx 45$) and swirl (S up to 1.3) levels and lean and stoichiometric burning conditions. Hydrogen was found to increase AFT, total energy, and combustion diffusivity, raise the reaction zone temperature, reduce the size of IRZ and shift its location in the far stream flow, and result in longer flames, due to the interaction of high H₂ reactivity with the high turbulence level studied.

Conversely, the swirl intensity was found to reduce the flame surface area and associated heat release, increase the size of IRZ and shift its location in the upstream direction, and result in shorter flames, due to the increased turbulent intensity. Coupling hydrogen addition with swirl intensity, it was concluded that both variables have a counter effect on the flame shape, length, and aerodynamics. Hence, it was recommended to increase the swirl intensity when using fuel blends with high H₂ concentrations.

Regarding emissions, hydrogen addition and swirl intensity were found responsible for slightly increasing NO_x emissions; however, such an increase was considered insignificant, as long as NO_x levels were generally in the order of a few ppm at the burner's outlet.

Moreover, hydrogen and swirl were found to reduce CO as they allow its conversion into CO₂, which was also reduced with an increased hydrogen addition.

For the combustion regime, a change in hydrogen concentration or swirl intensity was found not to be influential on the turbulent premixed combustion regime, which remains controlled by turbulence.

Lastly, the goal of this dissertation was to analyze HEC and emphasize that it is a promising approach towards a clean combustion.

FUTURE WORK

The first recommendation for the future work related to this dissertation is generating a Chemical Reactor Network (CRN) based on the proposed CFD model in order to precisely determine the slowest emissions (NO and CO). A network of Perfect Stirred Reactors (PSR) is expected to be used, due to the existence of IRZ and considering that Da is close to unity. For this concern, the preliminary trials are already being run using the STAR-CCM+ version 2020.2 “Reactor Network” module. An algorithmic clustering of the CFD field with $\Delta T = 55$ K and $\Delta f = 0.002$ is used to generate the network. Figure 5.26 shows two samples of the generated networks for the 50° (top) and 60° (bottom) swirl configurations with HVR of 25% and 50%, respectively, at $\phi = 0.7$.

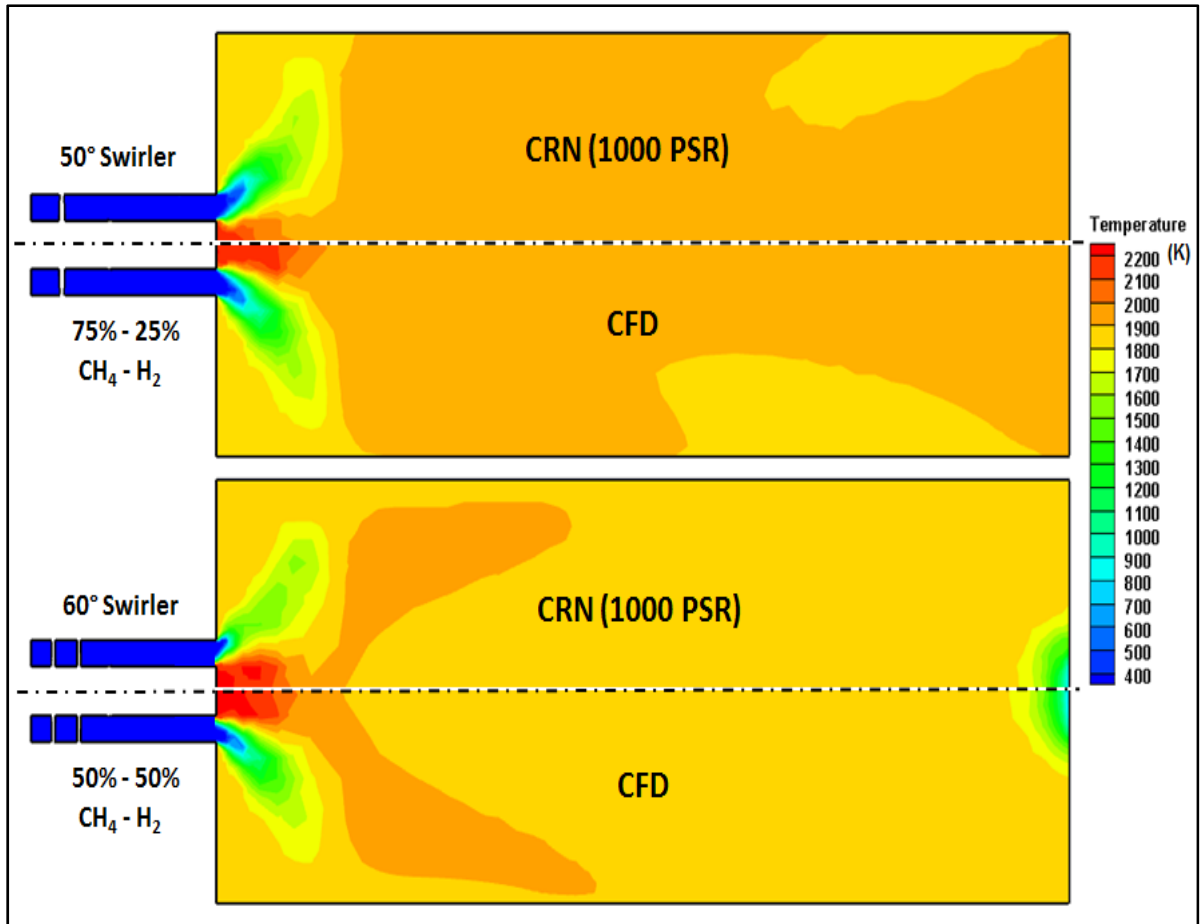


Figure 5.26 Samples of the generated networks for swirl-HVR couples of 50°-25% (top) and 60°-50% (bottom) at $\phi = 0.7$

The second recommendation for future work is studying the combustion of other alternative fuels, such as $\text{H}_2\text{-CO}$ or $\text{H}_2\text{-CO}_2$ syngas, and identifying its contribution for decreasing emissions.

The third recommendation for future work is studying the effect of considering the hydrogen preferential diffusion on the various combustion characteristics.

APPENDIX I

MORE VALIDATION RESULTS

I.1 3D flame visualization in terms of AFT and OH radical

Figure-A I-1 shows two 3D flame visualizations in terms of the AFT (top) and OH radical mass fraction (bottom), with the 3D stream traces coloured by the axial velocity. Regarding the swirling flow pattern, it can be seen that the global flow pattern can be characterized by the presence of IRZ along the burner's symmetric line, CRZ at the corners, and reversed flow inside the ROI. Such an IRZ is responsible for stabilizing the flame, where hot products are mixed with the incoming fuel-air mixture, and thus is considered one of the most important flow features of swirl stabilized flames (Huang et al., 2003; Huang & Yang, 2005).

In addition to the swirling flow pattern, the following observations can be made with respect to the flame features: 1) The flame is hung on the edges of the bluff body. 2) The flame occupies the entire width of the combustion. 3) The flame looks very fragmented and not like a continuous flame. The very fragmented appearance of the flame is attributed to the rich regions that have been previously identified in the non-reactive flow model. The same flame shape observations were reported by Taupin (2003).

I.2 3D flame visualization in terms of S_t

Figure-A I-2 shows the 3D flame visualization in terms of the turbulent flame speed (S_t). It can be seen that the flame develops in the combustion chamber in the form of a tulip, similarly to Taupin (2003). As well, the flame occupies only the ROI and looks fragmented, as mentioned above.

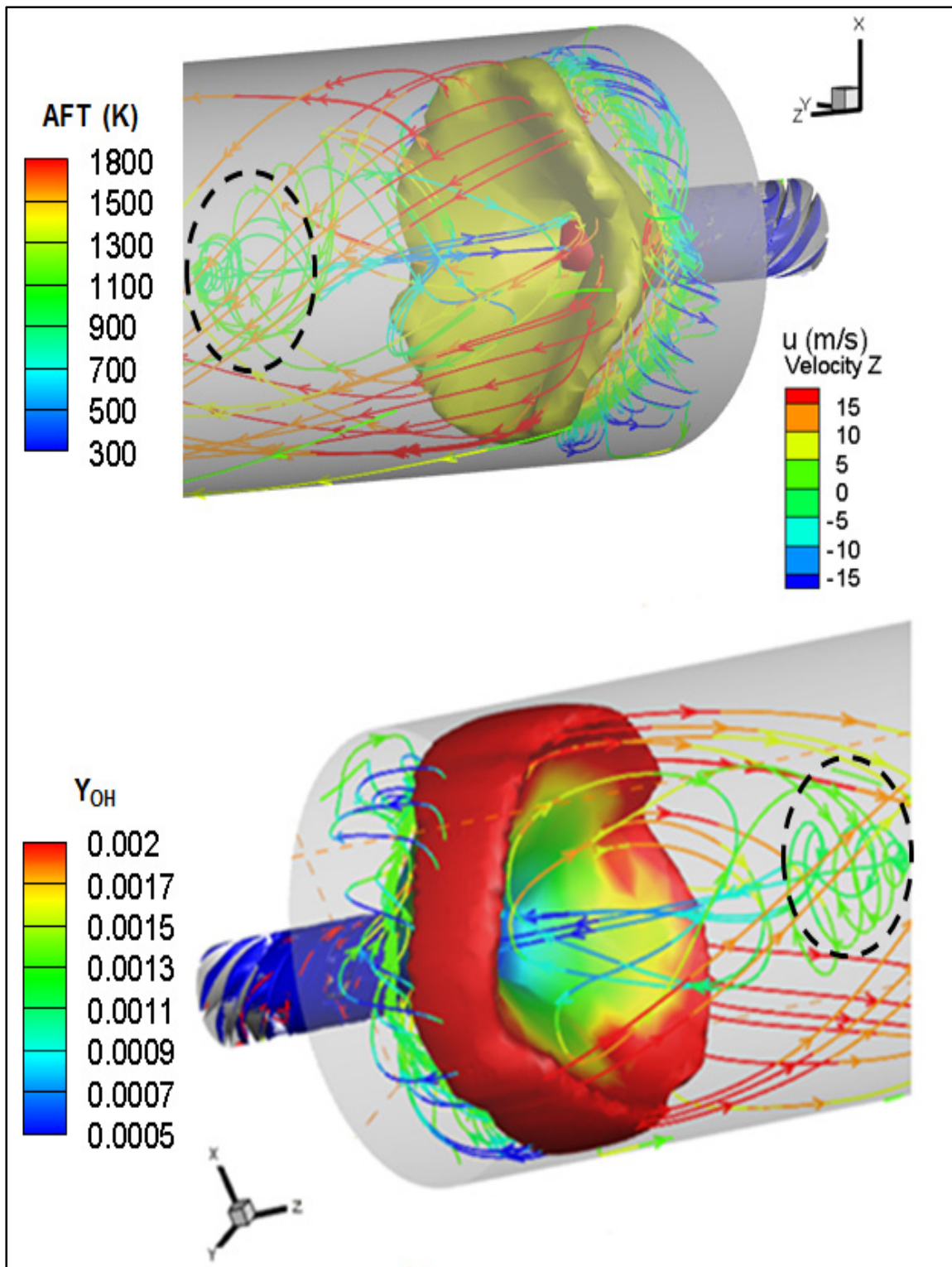


Figure-A I-1 3D flame visualization in terms of the AFT (top) and OH radical (bottom) iso-surfaces with the stream traces coloured by the axial velocity, methane-air combustion case at $\phi = 0.65$

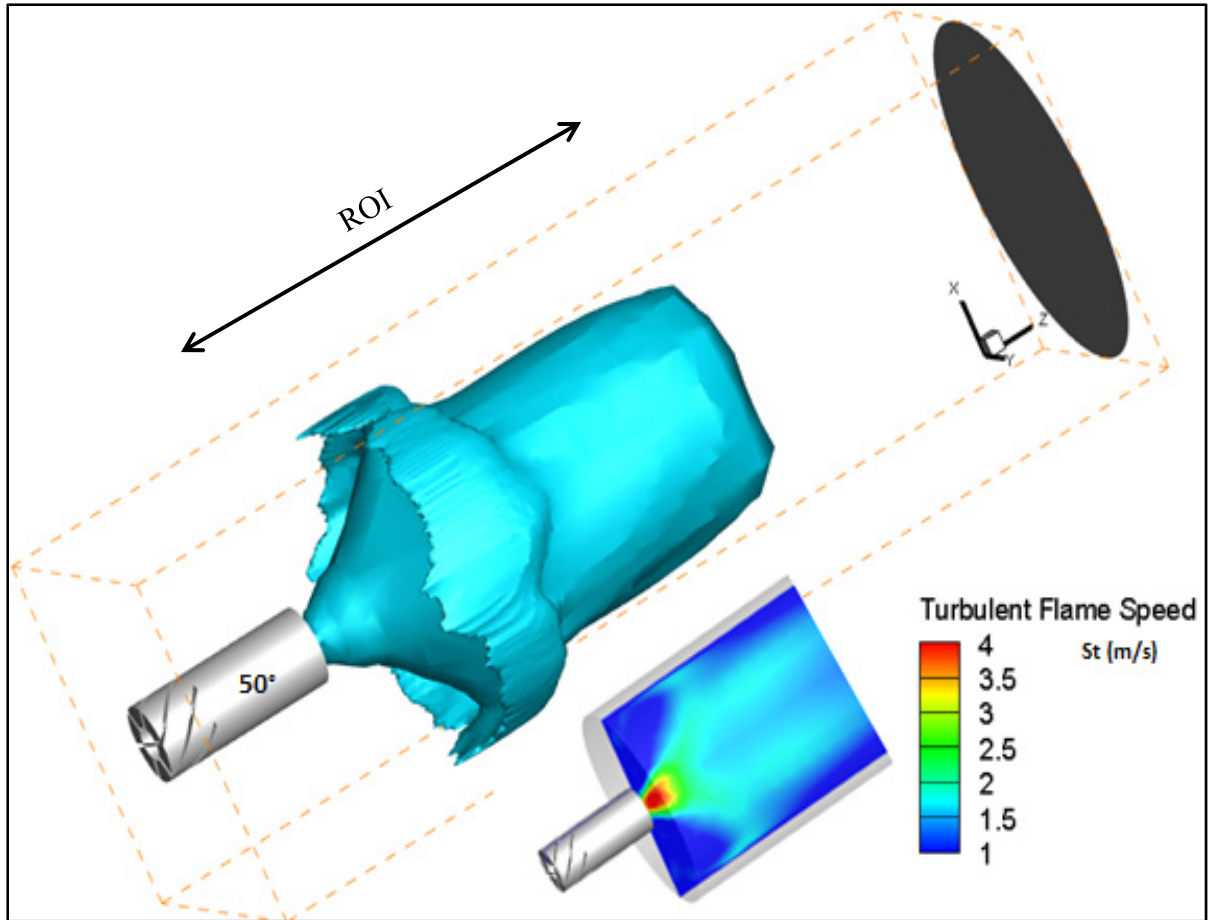


Figure-A I-2 3D tulip flame shape identified in terms of the turbulent flame speed (St), methane-air combustion case at $\phi = 0.65$

I.3 Back flow identification at the burner's outlet ($\phi = 0.65$)

Figure-A I-3 shows the captured back flow region at the 50° burner's outlet (basic swirl configuration) for the methane-air combustion at $\phi = 0.65$, identified through the distribution of the axial velocity (top), equivalence ratio (middle), and temperature (bottom) inside the entire combustion chamber length. This back flow can be identified by: a reversed flow with almost a zero-axial velocity (top), a lean methane-air mixture with $\phi \approx 0.5$ (middle), and a low temperature ≈ 1200 K (bottom). The same back flow was reported by Taupin (2003), who confirmed that the combustor could suck air from the outside as IRZ might end at the burner's outlet.

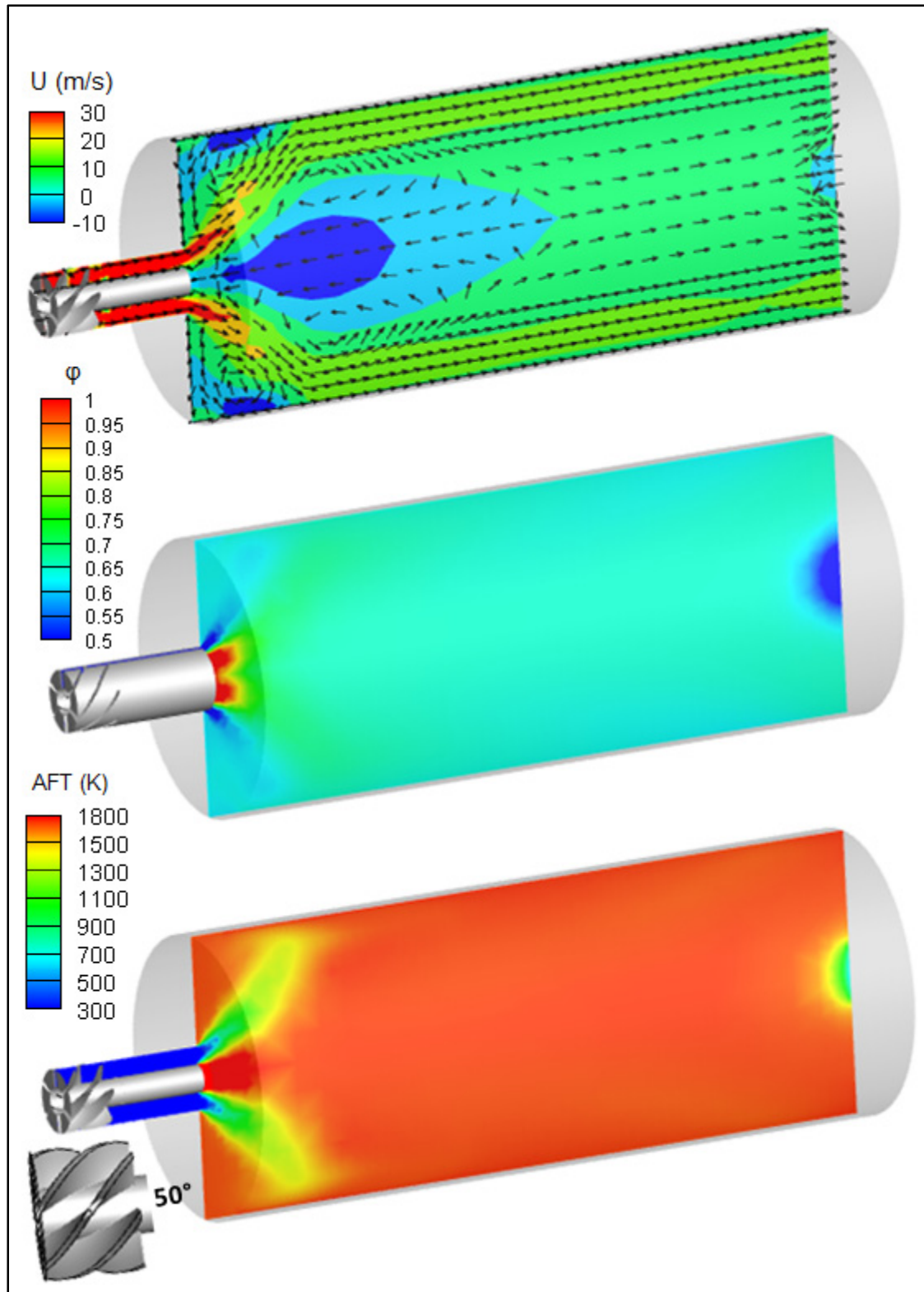


Figure-A I-3 CFD model fidelity identified by capturing a back flow at the 50° burner's outlet in terms of: U (top), ϕ (middle), and AFT (bottom)

I.4 CFD model extension for different equivalence ratios

Figure-A I-4 shows the CFD reactive flow model predictions of AFT, OH mass fraction, equivalence ratio, and main combustion products (CO_2 and H_2O) from top to bottom, respectively, at the three equivalence ratios, 0.7, 0.85, and 1, from left to right, respectively.

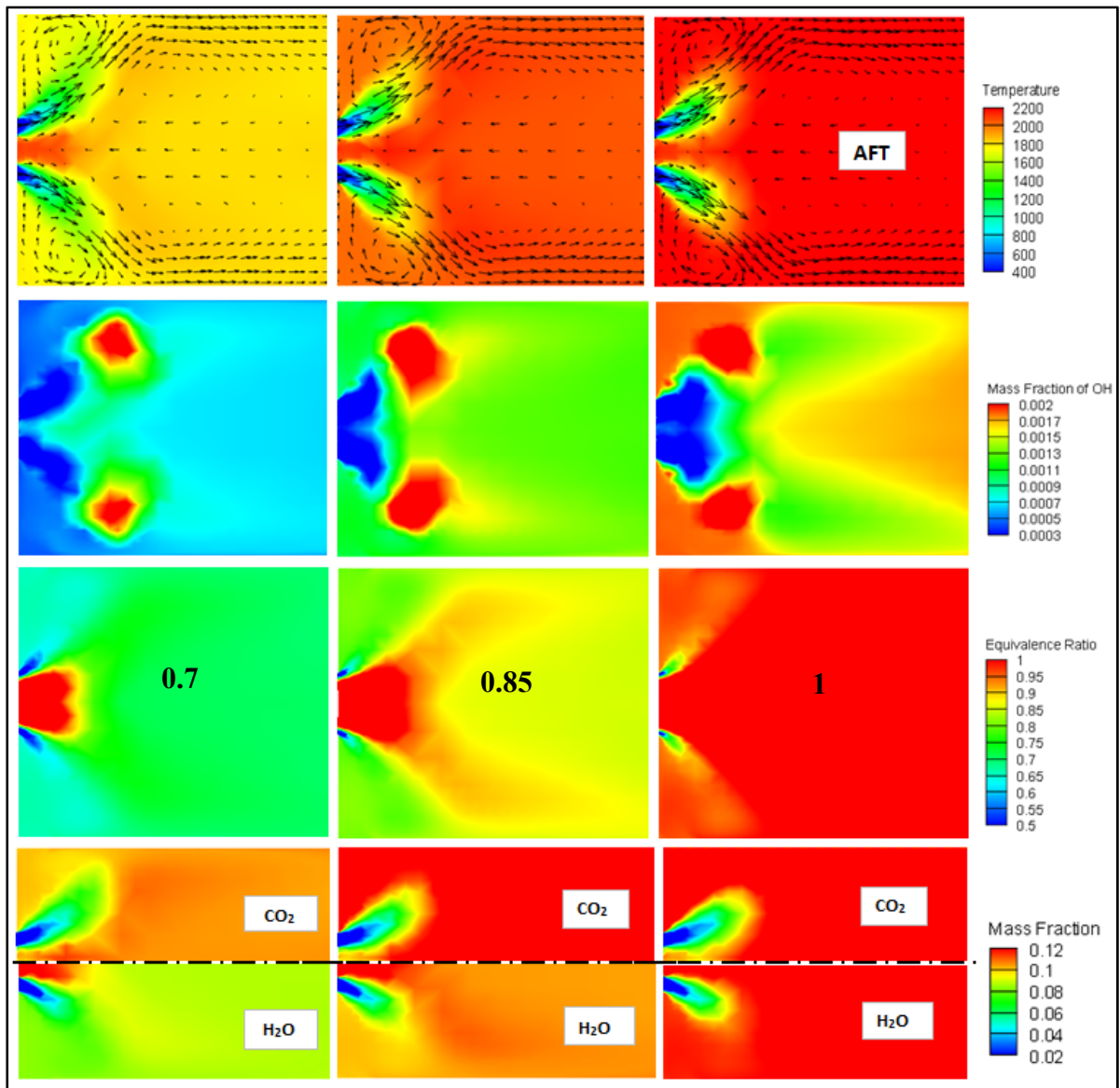


Figure-A I-4 CFD model predictions of AFT, OH mass fraction, equivalence ratio, and main products, respectively, from top to bottom, at three equivalence ratios, 0.7, 0.85, and 1, respectively, from left to right

It can be seen that the temperature increases with an equivalence ratio increase. The maximum temperature attained under stoichiometric burning conditions is ≈ 2227 K, which fills the entire ROI, except for the shear layers or jet. The OH mass fraction increases with an equivalence ratio increase. The main combustion products (CO_2 and H_2O) increase with an equivalence ratio increase.

I.5 CFD model extension for different preheat conditions

Figure-A I-5 shows the AFT distribution inside the ROI for an inlet preheat of 400 K (top), 500 (middle), and 600 K (bottom) of the methane-air combustion at $\phi = 0.7$. It is found that: 1) Increasing the inlet preheat from 400 K to 500 and 600 K increases the AFT from 1910 K to 1980 and 2050 K, respectively. This increase is linked to the increased chemical rates as well as the thermal and mass diffusivities, which increases the maximum attainable temperature. The same effect was reported by Natarajan & Lieuwen, (2007). 2) Changing the inlet preheat condition/temperature highly affects the flame shape, similarly to Taupin (2003). Hence, the flame shape is identified for the three studied preheat conditions/temperatures (400, 500, and 600 K) in terms of the OH radical as well as the turbulent flame speed below.

Figure-A I-6 shows the OH radical mass fraction distribution inside the ROI of the three studied inlet preheats: 400 K (top), 500 (middle), and 600 K (bottom) for the methane-air combustion at $\phi = 0.7$. It can be seen that: 1) Increasing the inlet preheat increases the levels of OH radicals inside the entire ROI, similarly to Taupin (2003), who identified high effects due to preheat by measuring the spontaneous CH emissions. This increase is attributable to the increased temperature levels inside the ROI associated with the increased kinetic rates. 2) The highest studied preheat (600 K) shows a compacted flame shape, compared to the one at $T_{\text{in}} = 400$ and 500 K. To clarify this compactness, the flame shape is identified in terms of the turbulent flame speed next.

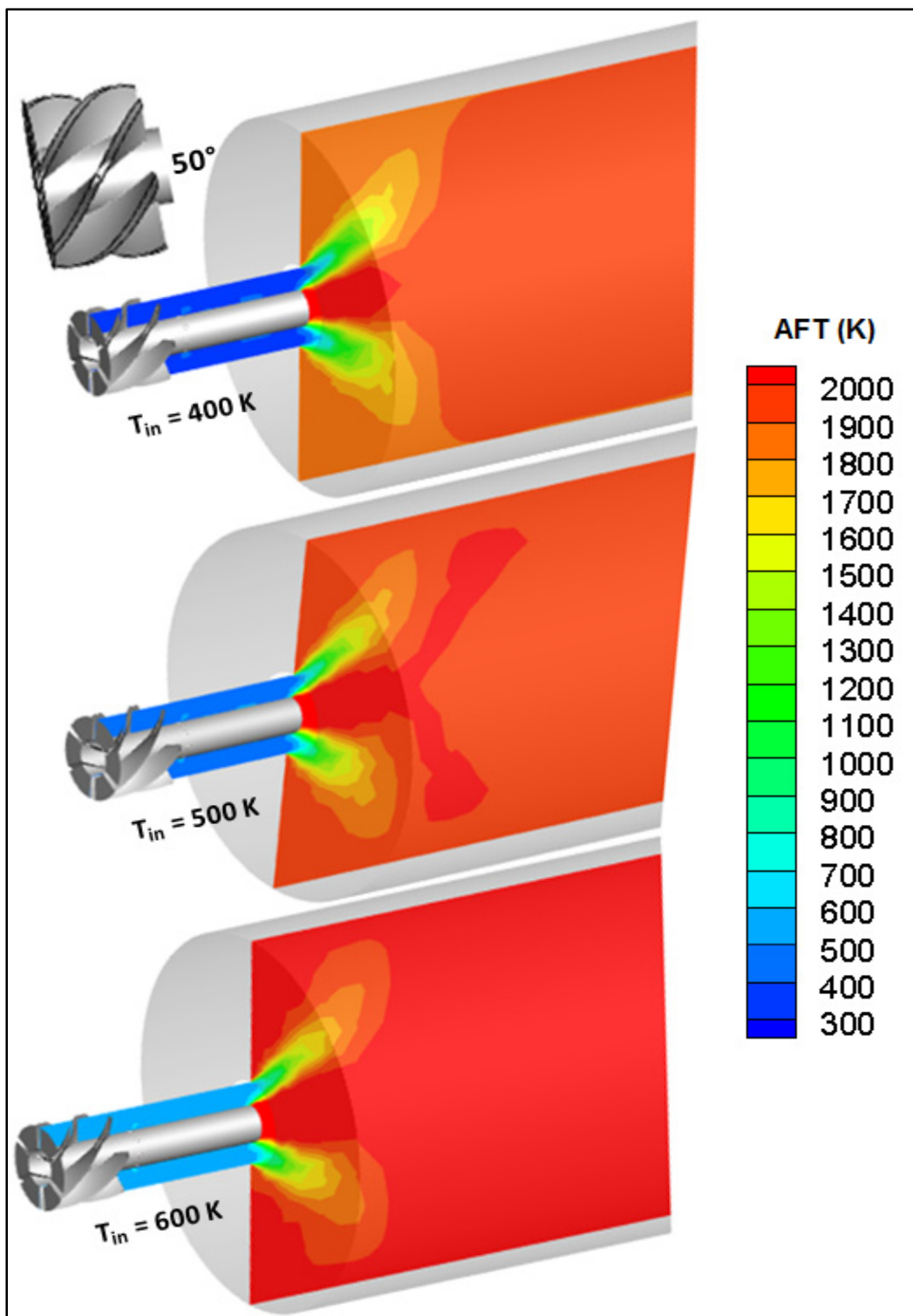


Figure-A I-5 CFD model predictions of AFT for different preheat condition, 400 K (top), 500 K (middle), and 600 K (bottom), methane-air combustion case at $\phi = 0.7$

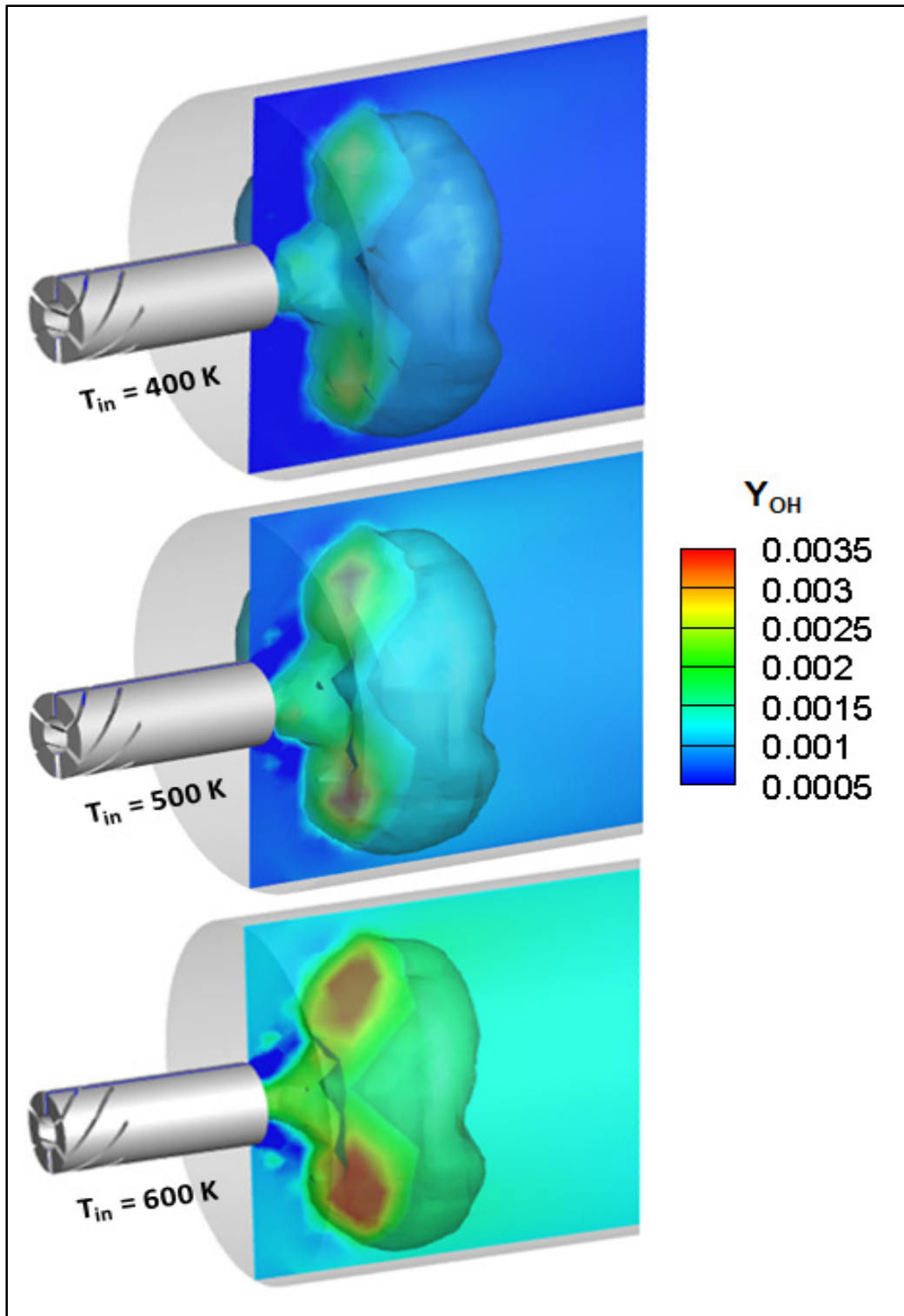


Figure-A I-6 CFD model predictions of OH radical for different preheat condition, 400 K (top), 500 K (middle), and 600 K (bottom), methane-air combustion case at $\phi = 0.7$

Figure-A I-7 shows the 3D flame visualization in terms of the turbulent flame speed (S_t) inside the ROI of the three studied inlet preheats: 400 K (top), 500 (middle), and 600 K (bottom) for the methane-air combustion at $\phi = 0.7$. It can be seen that: 1) Increasing the inlet preheat increases the turbulent flame speed, due to the increased chemical rates as well as the thermal and mass diffusivities, similarly to Natarajan & Lieuwen (2007). 2) Increasing the inlet preheat decreases both the flame length and radius, similarly to Taupin (2003).

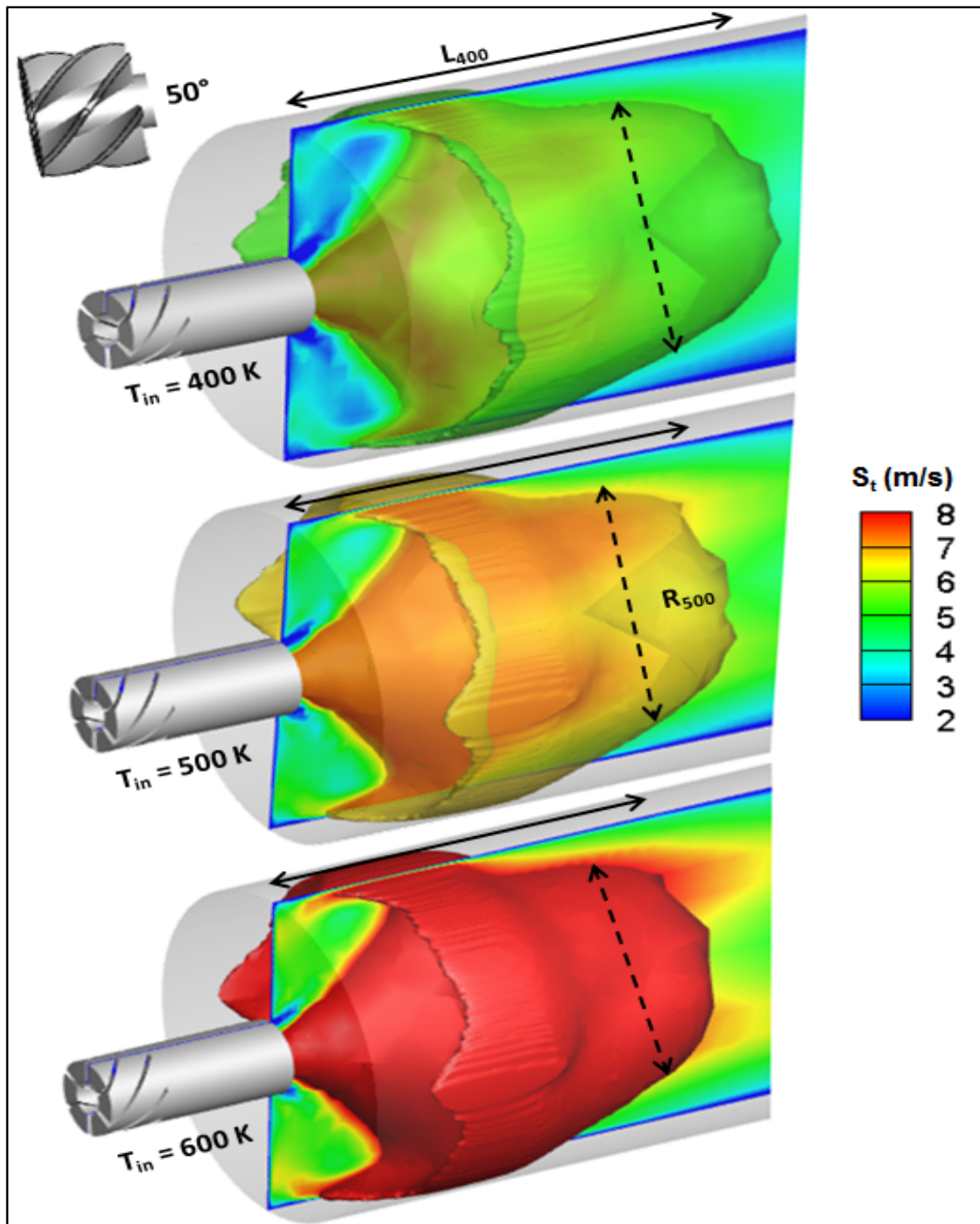


Figure-A I-7 CFD model predictions of flame shape (in terms of S_t) for different preheat condition, 400 K (top), 500 K (middle), and 600 K (bottom), methane-air combustion case at $\phi = 0.7$

APPENDIX II

UNSTABLE RESULTS

Figure-A II-1 shows the irregular temperature distribution inside the entire combustion chamber under the stoichiometric burning condition ($\phi = 1$) for swirl-HVR couples of 50°-75% (top), 50°-90% (middle), and 55°-90% (bottom). It can be seen that the three studied cases couldn't sustain a stable flame inside the ROI, where a cold flow is identified, instead of the flame. This singularity is related to the incapability of such configurations to form a reversed flow region inside the ROI, due to the non-existence of IRZ inside the combustion chamber. Instead, a unidirectional flow is formed inside the combustion chamber, as seen in Figure-A II-2.

From Figure-A II-1, it can also be observed that the region of irregularity (singularity) decreases with a swirl vanes angle increase from 50° (middle) to 55° (bottom). This indicates that increasing the swirl intensity counteracts the high hydrogen concentration (90%) effect, i.e. the swirl intensity increase helps restabilize the flame. This restabilization effect can be identified in Figure-A II-2, where it can be seen that the region with the stagnant flow (axial velocity in light blue) appears only in the 55° swirl configuration (bottom), however, the effect of hydrogen is more powerful in preventing such a restabilization trial. The net result is that the 55°-90% swirl-HVR couple could not sustain a stable flame.

Figure-A II-3 shows the 3D stream traces of the 50°-75% (top) and 50°-90% (bottom) swirl-HVR couples, where neither IRZ, CRZ, nor reversed flow regions formed at $\phi = 1$. Instead, a rotating flow is identified at the combustion chamber entry and a unidirectional flow is identified along the entire combustion chamber length until the outlet.

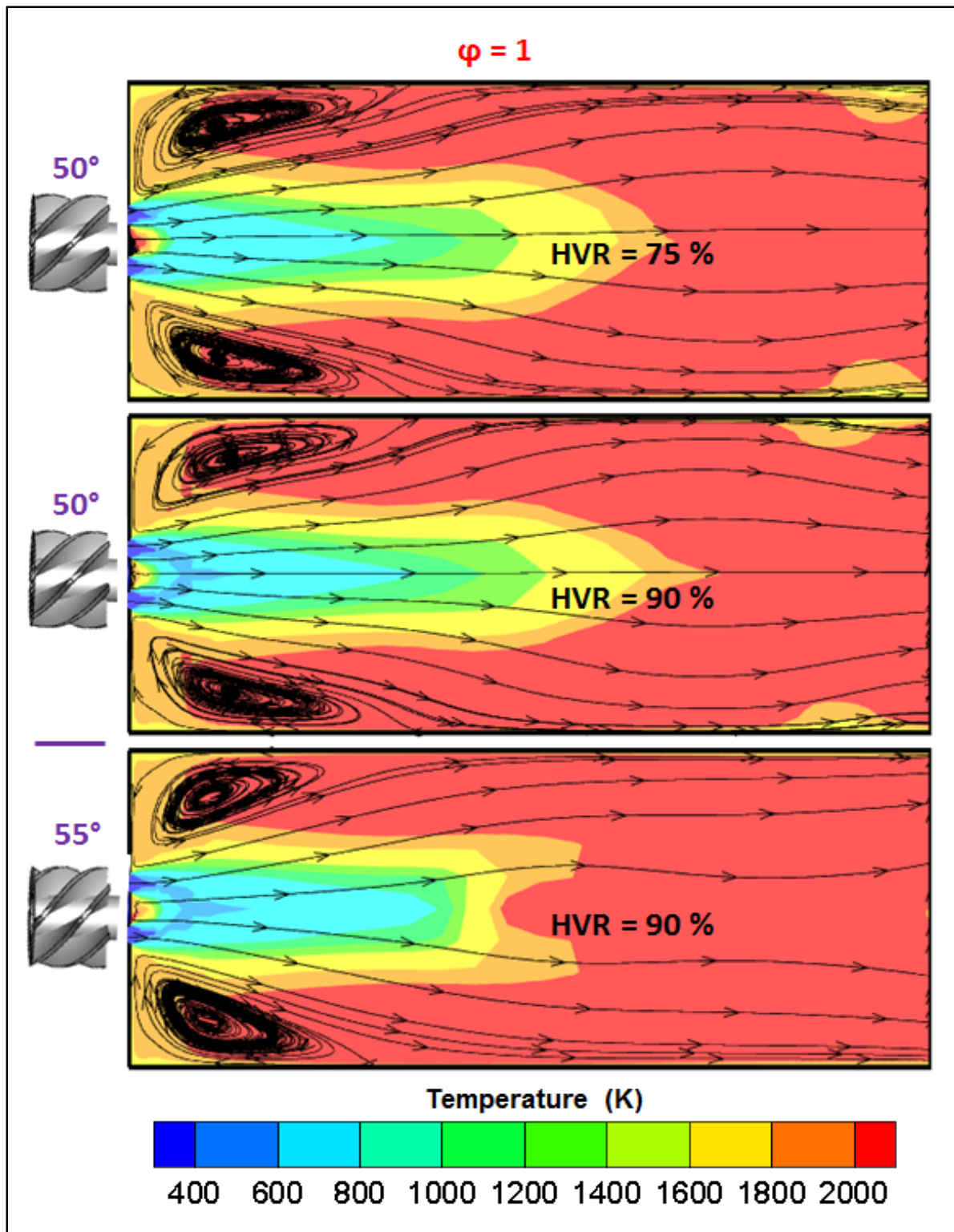


Figure-A II-1 Irregular temperature distribution inside the entire combustion chamber at $\phi = 1$ for swirl angle-HVR couples of 50°-75% (top), 50°-90% (middle), and 55°-90% (bottom)

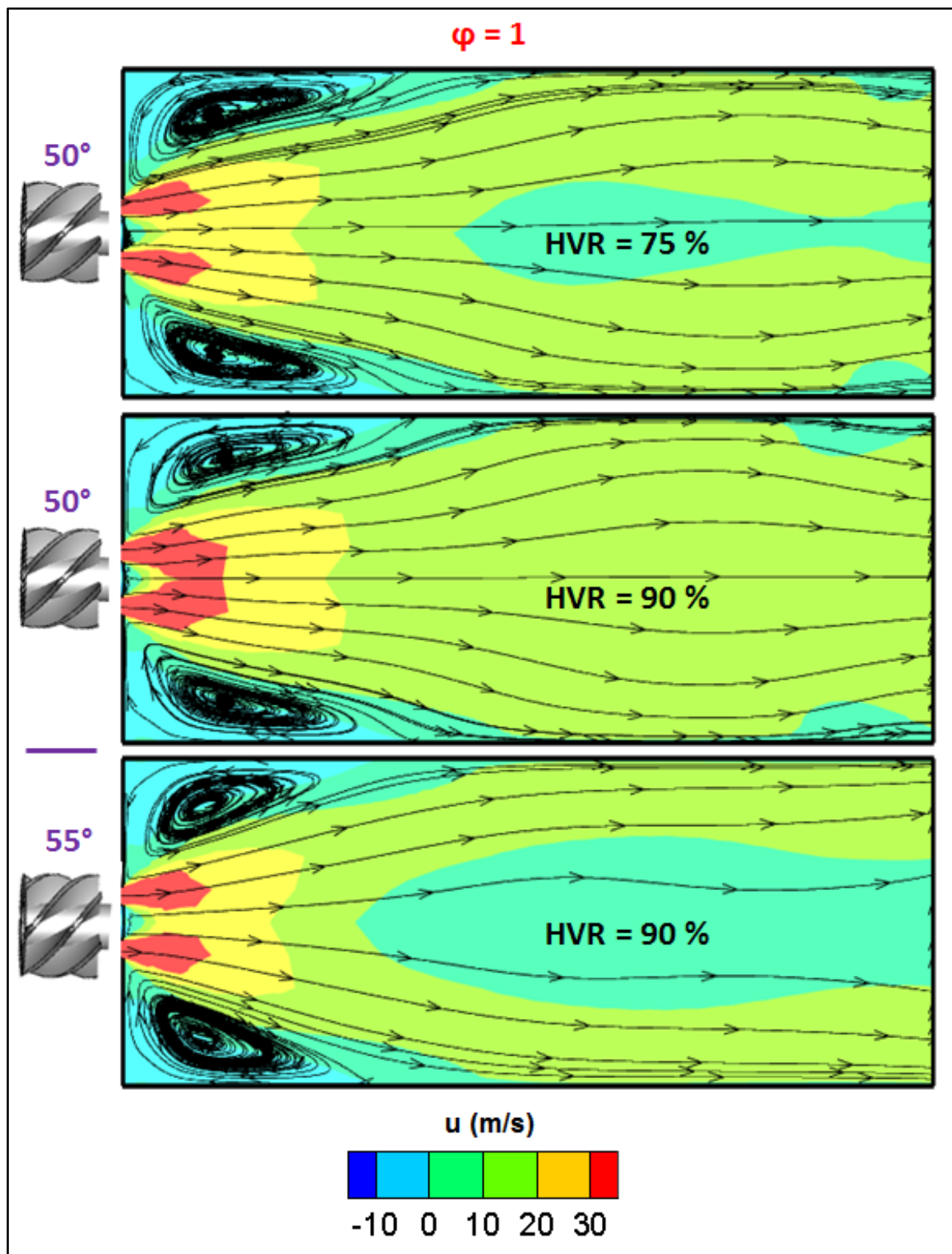


Figure-A II-2 Irregular streamlines distribution inside the entire combustion chamber at $\varphi = 1$ for swirl angle-HVR couples of 50°-75% (top), 50°-90% (middle), and 55°-90% (bottom)

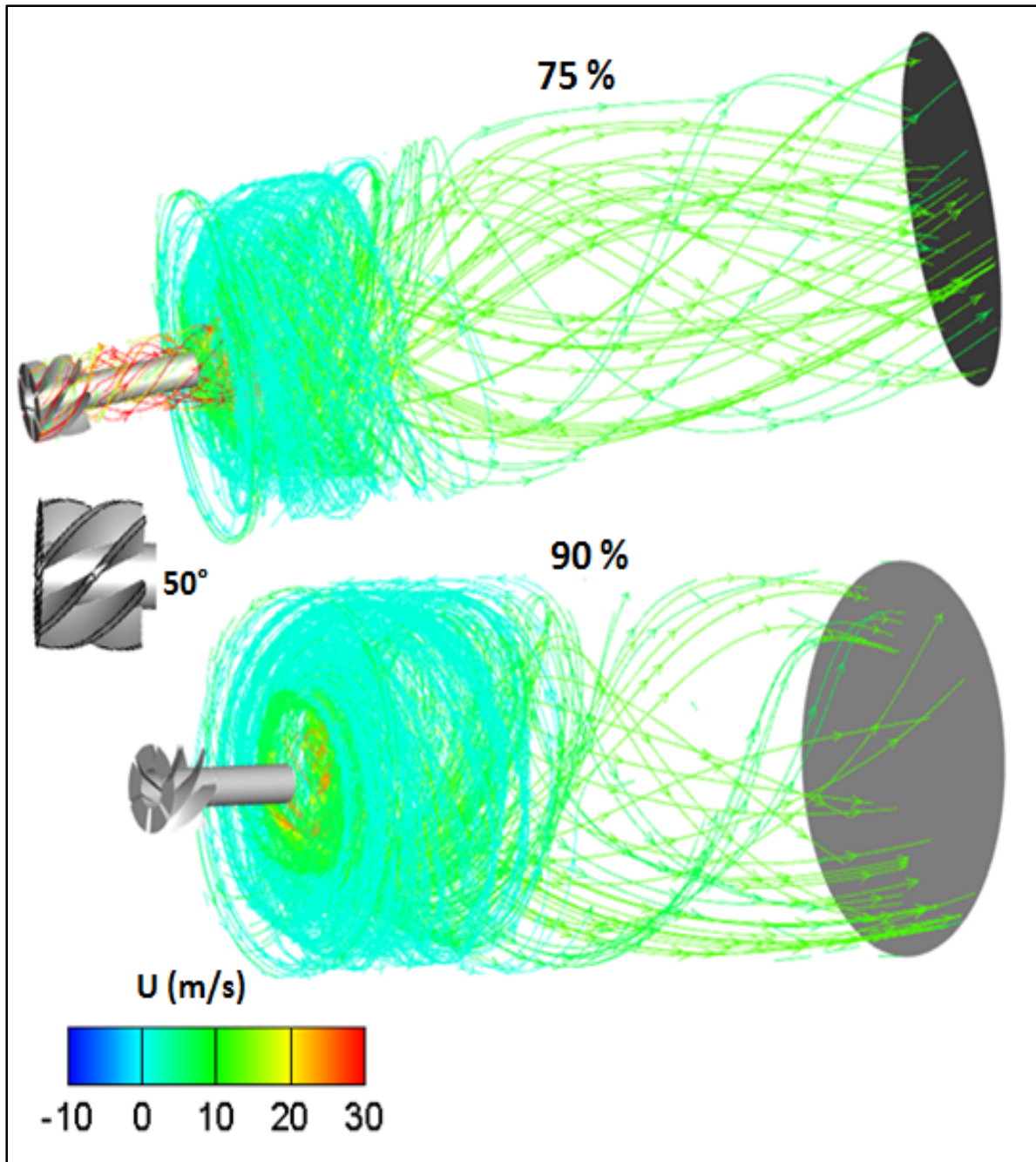


Figure-A II-3 3D stream traces distribution inside the 50° burner at $\phi = 1$ for HVR = 75% (top) and 90% (bottom)

BIBLIOGRAPHY

- Abe, K., Kondoh, T., & Nagano, Y. (1994). A new turbulence model for predicting fluid flow and heat transfer in separating and reattaching flows. *International Journal of Heat and Mass Transfer*, vol. 37, n° 1, p. 139–151.
- Ali, A., Nemitallah, M. A., Abdelhafez, A., Imteyaz, B., Kamal, M. M., & Habib, M. A. (2020). Numerical and experimental study of swirl premixed CH₄/H₂/O₂/CO₂ flames for controlled-emissions gas turbines. *International Journal of Hydrogen Energy*, vol. 45, n° 53, p. 29616–29629.
- Anderson, J. (2017). *Fundamentals of Aerodynamics*. Mc Graw Hill.
- Ayoub, M., Rottier, C., Carpentier, S., Villiermaux, C., Boukhalfaa, A., & Honoré, D. (2012). An experimental study of mild flameless combustion of methane/hydrogen mixtures. *International Journal of Hydrogen Energy*, vol. 37, n° 8, p. 6912–6921.
- Baulch, D., Drysdale, D., Horne, D., & Lloyd, A. (1973). Evaluated Kinetic Data for High Temperature Reactions. Butterworths London, vol. 2.
- Celik, I., Ghia, U., Roache, P., & Freitas, C. (2008). Procedure for estimation and reporting of uncertainty due to discretization in CFD applications. *Journal of Fluids Engineering*, vol. 130, n° 7.
- Choudhuri, A. R., & Gollahalli, S. R. (2000). Combustion characteristics of hydrogen–hydrocarbon hybrid fuels. *International Journal of Hydrogen Energy*, vol. 25, n° 5, p. 451–462.
- Day, M., Tachibana, S., Bell, J., Lijewski, M., Beckner, V., & Cheng, R. K. (2012). A combined computational and experimental characterization of lean premixed turbulent low swirl laboratory flames. *Combustion and Flame*, vol. 159, n° 1, p. 275–290.
- De, A., & Achary, S. (2012). Parametric study of upstream flame propagation in hydrogen-enriched premixed combustion: Effects of swirl, geometry and premixedness. *International Journal of Hydrogen Energy*, vol. 37, n° 19, p. 14649–14668.

- Environment and Climatic Change Canada. (2015). Retrieved from <http://prairieclimatecentre.ca/2018/03/where-do-canadas-greenhouse-gas-emissions-come-from>.
- Fichet, V., Kanniche, M., Plion, P., & Gicquel, O. (2010). A reactor network model for predicting NO_x emissions in gas turbines. *Fuel*, vol. 89, n° 9, p. 2202–2210.
- Goldin, G., Montanari, F., & Patil, S. (2014). A Comparison of RANS and LES of an Industrial Lean Premixed Burner. *Turbine Technical Conference and Exposition*. Düsseldorf, Germany: ASME.
- Gregory P. Smith, David M. Golden, Michael Frenklach, Nigel W. Moriarty, Boris Eiteneer, Mikhail Goldenberg, C. Thomas Bowman, Ronald K. Hanson, Soonho Song, William C. Gardiner, Jr., Vitali V. Lissianski, and Zhiwei Qin. (1999, 07 30). *GRI Mech. 3.0*. Retrieved 07 1999, from www.me.berkely.edu: http://www.me.berkely.edu/gri_mech
- Gülde, Ö. L. (1991). Turbulent premixed flame propagation models for different combustion regimes. *Symposium (International) on Combustion*, vol. 23, n° 1, p.743–750.
- Guo, S., Wang, J., Zhang, W., Zhang, M., & Huang, Z. (2020). Effect of hydrogen enrichment on swirl/bluff-body lean premixed flame stabilization. *International Journal of Hydrogen Energy*, vol. 45, n° 18, p.10906–10919.
- Gupta, A. K., Lewis, M. J., & Daurer, M. (2001). Swirl Effects on Combustion Characteristics of Premixed Flames. *Journal of Engineering for Gas Turbines and power*, vol. 123, n° 3, p. 619–626.
- Gupta, A. K., Lilley, D. G., & Syred, N. (1984). *Swirl flows*. Kent, England: Abacus Press.
- Hawkes, E. R., & Chen, J. H. (2004). Direct numerical simulation of hydrogen-enriched lean premixed methane–air flames. *Combustion and Flame*, vol. 138, n° 3, p. 242–258.
- Huang, Y., & Yang, V. (2005). Effect of swirl on combustion dynamics in a lean-premixed swirl-stabilized combustor. *Proceedings of the Combustion Institute 30* (p. 1775–1782). ELSEVIER.
- Huang, Y., Sung, H.-G., Hsieh, S.-Y., & Yang, V. (2003). Large-Eddy Simulation of Combustion Dynamics of Lean-Premixed Swirl-Stabilized Combustor. *Journal of Propulsion and Power*, vol. 19, n° 5, p. 782–794.

- İlbaş, M., Karyeyen, S., & Yilmaz, İ. (2016). Effect of swirl number on combustion characteristics of hydrogen-containing fuels in a combustor. *International Journal of Hydrogen Energy*, vol. 41, n° 17, p. 7185–7191.
- Imteyaz, B. A., Nemitallah, M. A., Abdelhafez, A. A., & Habib, M. A. (2018). Combustion behavior and stability map of hydrogen-enriched oxy-methane premixed flames in a model gas turbine combustor. *International Journal of Hydrogen Energy*, vol. 43, n° 34, p. 16652–16666.
- International Energy Agency. (2018). Retrieved from <https://www.iea.org/data-and-statistics/charts>.
- Karim, G., Wierzbza, I., & Al-Alousi, Y. (1996). Methane-hydrogen mixtures as fuels. *International Journal of Hydrogen Energy*, vol. 21, n° 7, p. 625–631.
- Khalil, A. E., Arghode, V. K., Gupta, A. K., & Lee, S. C. (2012). Low calorific value fuelled distributed combustion with swirl for gas turbine applications. *Applied Energy*, vol. 98, p. 69-78.
- Kim, H. S., Arghode, V. K., & Gupta, A. K. (2009 a). Flame characteristics of hydrogen-enriched methane–air premixed swirling flames. *International Journal of Hydrogen Energy*, vol. 34, n° 2, p. 1063–1073.
- Kim, H. S., Arghode, V. K., Linck, M. B., & Gupta, A. K. (2009 b). Hydrogen addition effects in a confined swirl-stabilized methane-air flame. *International Journal of Hydrogen Energy*, vol. 34, n° 2, p. 1054–1062.
- Kuenne, G., Ketelheun, A., & Janicka, J. (2011). LES modelling of premixed combustion using a thickened flame approach coupled with FGM tabulated chemistry. *Combustion and Flame*, vol. 158, n° 9, p. 1750–1767.
- Lefebvre, A. H. (1998). *Gas Turbine Combustion*. Philadelphia: Taylor & Francis.
- Maccallum, M. M. (1967). Swirling air jets issuing from vane swirlers.part1: free jets. *Journal of the institute of fuel*, 214–225.
- Meziane, S., & Bentebbiche, A. (2019). Numerical study of blended fuel natural gas-hydrogen combustion in rich/quench/lean combustor of a micro gas turbine. *International Journal of Hydrogen Energy*, vol. 44, n° 29, p. 15610–15621.

- Monaghan, R. F., Tahir, R., Cuoci, A., Bourque, G., Füre, M., Gordon, R. L., et al. (2012). Detailed Multi-dimensional Study of Pollutant Formation in a Methane Diffusion Flame. *Energy & Fuels*, vol. 26, n° 3, p. 1598–1611.
- Monaghan, R. F., Tahir, R., Cuoci, A., Bourque, G., Füre, M., Gordon, R. L., et al. (2014). Detailed Emissions Prediction for a Turbulent Swirling Nonpremixed Flame. *Energy & Fuels*, vol. 28, n° 2, p. 1470–1488.
- Natarajan, J., & T. Lieuwen, J. S. (2007). Laminar flame speeds of H₂/CO mixtures: Effect of CO₂ dilution, preheat temperature, and pressure. *Combustion and Flame*, vol. 151, n° 1-2, p. 104–119.
- Nemitallah, M. A., Imteyaz, B., Abdelhafez, A., & A.Habib, M. (2019). Experimental and computational study on stability characteristics of hydrogen-enriched oxy-methane premixed flames. *Applied Energy*, vol. 250, p. 433–443.
- Novoselov, I. V., & Malte, P. C. (2008). Development and Application of an Eight-Step Global Mechanism for CFD and CRN Simulations of Lean-Premixed Combustors. *Journal of Engineering for Gas Turbines and Power*, vol. 130, n° 2.
- Novoselov, I. V., Malte, P. C., Yuan, S., Srinivasan, R., & Lee, J. C. (2006). Chemical Reactor Network Application to Emissions Prediction for Industrial DLE Gas Turbine. *ASME Turbo Expo 2006: Power for Land, Sea, and Air*, vol. 42363, p. 221–235.
- Palanti, L., Pampaloni, D., Andreini, A., & Facchini, B. (2018). Numerical simulation of a swirl stabilized methane-air flame with an automatic meshing CFD solver. *Energy Proceeding*, vol. 148, p. 376–383.
- Persis, S. d., Cabot, G., Pillier, L., Gökalp, I., & Boukhalfa, A. M. (2013). Study of Lean Premixed Methane Combustion with CO₂ Dilution under Gas Turbine Conditions. *Energy Fuels*, vol. 127, n° 2, p. 1093–1103.
- Peters, N. (2001). *Turbulent Combustion*. IOP Publishing Ltd.
- S.Poireault PhD Thesis in French. (1997).
- Samaniego, J. M., Egolfopoulos, F. N., & Bowman, C. T. (1995). CO₂ Chemiluminescence in Premixed Flames. *Combustion Science and Technology*, vol. 109, n° 1-6, p. 183–203.

- Samiran, N. A., Chong, C. T., Ng, J.-H., Tran, M.-V., Ong, H. C., Valera-Medina, A., et al. (2019). Experimental and numerical studies on the premixed syngas swirl flames in a model combustor. *International Journal of Hydrogen Energy*, vol. 44, n° 44, p. 24126–24139.
- Schefer, R. W. (2003). Hydrogen enrichment for improved lean flame stability. *International Journal of Hydrogen Energy*, vol. 28, n° 10, p. 1131–1141.
- Schefer, R. W., Wicksall, D. M., & Agrawal, A. K. (2002). Combustion of hydrogen-enriched methane in a lean premixed swirl-stabilized burner. *Proceedings of the Combustion Institute*, vol. 29, n° 1, p. 843–851.
- Shy, S., Chen, Y., Yang, C., Liu, C., & Huang, C. (2008). Effects of H₂ or CO₂ addition, equivalence ratio, and turbulent straining on turbulent burning velocities for lean premixed methane combustion. *Combustion and Flame*, vol. 153, n° 4, p. 510–524.
- Soete, G. D. (1975). Overall reaction rates of NO and N₂ formation from fuel nitrogen. *Symposium (International) on Combustion*, vol. 15, n° 1, p. 1093–1102.
- STAR-CCM + Theory Manual. Retrieved from [plm.automation.siemens.com: https://www.plm.automation.siemens.com/global/en/products/simcenter/STAR-CCM.html](https://www.plm.automation.siemens.com/global/en/products/simcenter/STAR-CCM.html).
- Taupin, B., Cabot, G., Martins, G., Vauchelles, D., & Boukhalfa, A. (2007). Experimental study of stability, structure and CH* chemiluminescence in a pressurized lean premixed methane turbulent flame. *Combustion Science and Technology*, vol. 179, n° 1-2, p. 117–136.
- Taupin, Benoît PhD Thesis in French. (2003). *Etude de la combustion turbulente à faible richesse haute température et haute pression*. Rouen, France.
- Tu, Y., Xu, M., Zhou, D., Wang, Q., Yang, W., & Liu, H. (2019). CFD and kinetic modelling study of methane MILD combustion in O₂/N₂, O₂/CO₂ and O₂/H₂O atmospheres. *Applied Energy*, vol. 240, 1003–1013.
- Turns, S. R. (2000). *An Introduction to Combustion Concepts and Applications*. McGraw-Hill series in mechanical engineering.
- www.computecanada.ca/wiki/resources.

- Yilmaz, H., & Yilmaz, I. (2019). Combustion and emission characteristics of premixed CNG/H₂/CO/CO₂ blending synthetic gas flames in a combustor with variable geometric swirl number. *Energy*, vol. 172, p. 117–133.
- Zimont, V. L. (2000). Gas premixed combustion at high turbulence. Turbulent flame closure combustion model. *Experimental Thermal and Fluid Science*, vol. 21, n° 1-3, p. 179–186.